2015

Prompt gamma-ray imaging for on-line tracking of the bragg peak in proton radiation therapy

Melek Zarifi
University of Wollongong, mz659@uowmail.edu.au

Prompt Gamma-ray Imaging for On-line Tracking of the Bragg Peak in Proton Radiation Therapy

Melek Zarifi

A thesis submitted in partial fulfilment of the requirements for the award of the degree

Master of Philosophy

Medical Radiation Physics

from

University of Wollongong

Faculty of Engineering and Information Sciences

School of Physics

26 November 2015

Certification

I, Melek Zarifi, declare that this thesis, submitted in partial fulfilment of the requirements for the award of Master of Philosophy (Medical Radiation Physics), in the Faculty of Engineering and Information Sciences, School of Physics, University of Wollongong, is wholly my own work unless otherwise referenced or acknowledged. The document has not been submitted for qualifications at any other academic institution.

26 November 2015

Table of Contents

List of Tables

List of Figures

Abstract

Proton therapy (PT) requires reliable *in-vivo* beam range verification methods and techniques to ensure safe and accurate dose delivery to the targeted region while sparing critical organs-at-risk during the treatment delivery. Secondary prompt gamma (PG) rays emitted during PT have been proposed for on-line tracking and monitoring of the Bragg peak (BP) of the proton beam in real-time. The general principle of using PG imaging for *in-vivo* beam range verification has recently been proven. However, PG detection presents a great challenge since PG rays are generated from different nuclear reaction channels and have a broad energy range with strong interference backgrounds from the secondary neutrons and stray gamma rays. Currently there is a lack of detailed knowledge and quantitative methodology for clinically feasible PG imaging system development. The purpose of this study is to investigate PG detection strategies for optimal PG image formation in PT. The novelty of the work performed in my thesis is such that a systematic study of PG ray emission in water and PMMA phantoms from high energy proton beam irradiations has been carried out, which provides broad information of PG signal characteristics in spectral, spatial and timing aspects as compared to the main background signal from neutrons. To my knowledge, this kind of study has not yet been reported from any literature. Specific aims include: (i) quantifying the correlation between the longitudinal PG emission and the position of the BP in the patient; (ii) characterising PG detection dependencies on PG energy and timing properties; (iii) modelling PG detection with a proposed BGO detector.

The energy spectra, spatial spectra and time-of-flight (TOF) of the PG emission and detection from high energy proton irradiations have been extensively studied by means of dedicated Geant4 Monte Carlo simulations. In particular, a 200 MeV pencil proton beam has been modelled incident on different phantoms representing the patient and used in routine clinical Quality Assurance (water or PMMA, cubic or cylindrical shape). Alternative phantoms were selected to study the effect of their material and geometry on the PG ray emission and detector response. The yield of PG rays was compared to the yield of background neutrons produced as secondary radiation field by the PT treatment. The PG distribution has been quantitatively correlated with the BP position in the phantoms, considering possible different PG energy windows. Then, the response of a BGO based detector of size 45x45x25 mm^3 for PG detection has been modelled.

Our results show that the PG has a relatively high yield mainly depending on the oxygen and carbon composition of the phantom materials. The PG yield in the energy range of 4.2-6.3 MeV from the water and PMMA cylindrical phantoms are around 5-6% per incident proton. The longitudinal distribution of the PG emission is strongly correlated with the BP position of the proton beam. Yet the differences between the PG fall-off and BP fall-off are ∼4 mm in the 4.2-4.6 MeV and 4.2-6.3 MeV energy ranges in water, and in PMMA are ∼1 mm in the 4.2-4.6 MeV range and ∼2 mm in the 4.2-6.3 MeV range. These differences could affect the accuracy of the beam range verification using the PG signal. Our results also show that there exists an optimal energy window at approximately 4.44 MeV for PG detection. The PG signal in this energy window has a better correlation with the BP position and a higher PG-neutron ratio than other energy windows. There is also a prominent PG emission slightly backward peaked relative to the BP position, with higher PG-neutron yield ratio. The timing properties of PG emission also show a narrow TOF window around 3 ns which is well differentiated from the background neutrons. These results indicate that there exists an optimized strategy for PG signal detection. Utilising the optimized energy window, angular window, and TOF window determined by means of this Geant4 simulation study, PG image formation can be significantly improved for BP tracking.

Acknowledgments

I would like to express my gratitude to a number of people, many of whom are members of the University of Wollongong (UOW) Centre for Medical Radiation Physics (CMRP).

I thank my supervisor Dr. Yujin Qi (CMRP) for his guidance and contribution to this project, and the many discussions and analysis of results.

I thank Prof. Anatoly Rosenfeld (CMRP) for his constant support, contribution and dedication to the completion of this project.

My deepest gratitude goes to Dr. Susanna Guatelli (CMRP) for her constant support, guidance and contribution to this project, without whom the completion of this project would not have been achieved. Her dedication to helping me with Geant4 will always be greatly appreciated. She also provided the initial code that was built on for this project.

I thank Dr. Dean Cutajar (CMRP) for his assistance with Geant4 and the UOW HPC cluster, and for the many useful discussions and advice he provided throughout this project.

My sincere gratitude goes to David Bolst for his constant help with Geant4 throughout this project. His assistance is much appreciated.

We would like to thank Prof. Brian Hutton (University of College London, London UK) for his advice and discussions.

We would also like to thank the University of Wollongong Information Technology Services (ITS) for computing time on the UOW High Performance Computing Cluster.

I would like to thank my friends for their support and encouragement through the years. You have filled many of my days with incredible laughter, and have made this process easier. I am so grateful to call you friends. You will always be in my heart. My warmest gratitude and many thanks goes to my family, without whom I would not have had the strength to carry on each day. Your incredible love and support have helped me through this stressful time, and you are the reason I have come this far. Words cannot express my thank to you, and my appreciation for having you in my life. You are and always will be the light in my heart when all hope seems lost. I would also like to thank God for giving me strength, and for the life that I am blessed with, that is filled with joy and love, and wonderful people. Thank you.

Chapter 1

Introduction

1.1 General Aspects of Proton Therapy (PT)

Radiation therapy using beams of charged particles, such as protons and heavier ions such as carbon, is known as hadron therapy.[1] The potential benefit of protons as a method of radiation therapy was first proposed by Robert R. Wilson in 1946.[2] The synchrocyclotron at Lawrence Berkeley Laboratory (LBL), Berkeley USA, became available to investigate proton beams for radiotherapy and made the first patient treatment in 1954.[3] Then heavier ions for radiotherapy followed at the Bevalac facility at LBL in1975.[4] The first hospital-based PT facility opened in 1990 at the Loma Linda University Medical Center (LLUMC) in California.[5] The several decades of research and investigation by scientists have paved the way of vast progress to improve the accuracy and technique of dose delivery in radiotherapy. Currently, there are 58 operational clinical proton centres worldwide, and 52 under construction and in planning stages, with about 55,000 patients reported to have been treated with PT worldwide.[6,7]

Ideally, radiotherapy is delivered in order to destroy cancer cells, such that the dose is uniform and maximum at the target volume while is minimised as much as possible outside the target volume, with the goal to spare normal healthy tissue. Unlike the conventional photon beams, which have a high entrance dose that decreases gradually along the path giving an unwanted entrance and exit dose (see Figure 1), a proton beam can penetrate the tissue with limited lateral scattering, depositing most of its energy near the end of its track, and stops abruptly at the distal edge of the target volume. This maximum of energy deposition is termed the Bragg Peak, whose property allows the precise definition of the targeted region to be irradiated.[1] The difference between the depth dose of a photon beam and a spread-out-Bragg-peak (SOBP) dose achieved by protons can be seen in Figure 1, where the proton dose distribution conforms closely to the 'ideal' dose distribution. That is, a mono-energetic proton beam produces a Bragg curve with a single pristine Bragg peak, but adding together several Bragg peaks of varied energies produces a proton dose distribution with uniform maximum energy deposition in the entire target tumor, i.e. the proton SOBP depth dose curve. This highly conformed dose distribution from PT has the potential to result in a higher probability

for local control and disease-free survival, as well as lower probability for normal tissue damage[8], reducing the risk of side effects and further complications. However, treatments with charged particles are sensitive to the uncertainty in the determination of beam range. The distal dose fall-off, due to errors in patient setup or positioning, anatomical motion, and various other biological factors, lead to the employment of large safety margins in current PT treatments at the expense of the treatment quality.[9,10] Therefore, heavy charged particle radiation therapy requires reliable techniques for beam range verification to ensure that dose is delivered as planned in the treatments.

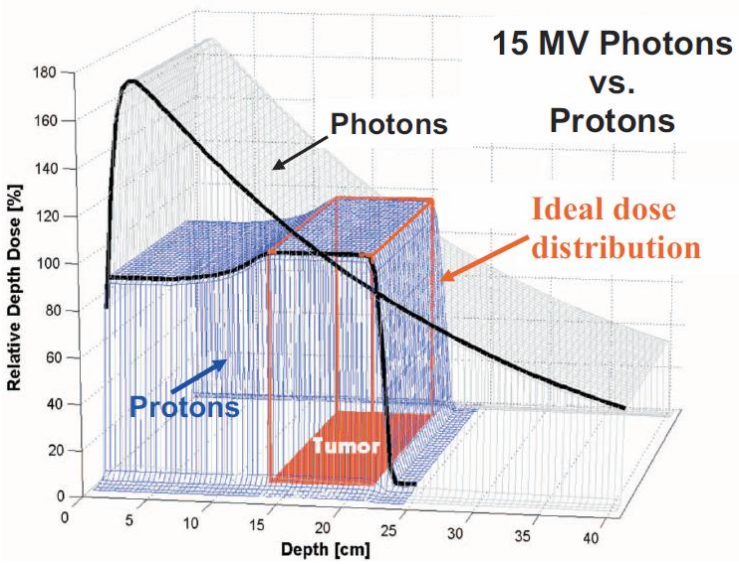

Figure 1: A dose versus depth comparison of a photon beam and a SOBP proton beam. From Ref. 8.

1.2 The Challenges of Beam Range Verification in Proton Therapy

Beam range verification is one of the major challenges in hadron therapy to ensure safe and accurate treatment delivery to the targeted tumor while sparing critical organs-at-risk close to the treatment region. Over the last several years, many different approaches for *in-vivo* beam range verification have been proposed and investigated. Yet there are still crucial critical issues which need to be solved for the development of clinically suitable and reliable *in-vivo* beam range verification techniques.

1.2.1 Overview of Beam Range Verification Methods

Table 1 and 2 compare the beam range verification approaches currently under development for PT Quality Assurance. These approaches can be classified alternatively into

direct and *indirect* measurement techniques. A direct method is such that the proton range is obtained directly from dose or fluence measurements, whereas an indirect method is such that the beam range determination is inferred from other signals. In terms of timing, the methods may be *on-line* or, alternatively, *off-line*. On-line timing has the beam range verification performed during or immediately before treatment delivery, whereas off-line methods have the beam range verified after the treatment is completed. Moreover, the measurements may be 1D, 2D (imaging) or 3D (volumetric).[11]

Table 1: Comparisons of *in-vivo* range verification methods. Adapted from Ref. 11.

Method	Timing	Dimension	Signal
In-vivo point measurements	On-line	1D	Direct
Range probe	On-line	1D	Direct
Proton radiography and tomography	On-line	2D/3D	Direct
PG imaging	On-line	2D/3D	Indirect
PET imaging	On-line/Off-line	3D	Indirect
MRI imaging	Off-line	3D	Indirect

Table 2: Status of *in-vivo* range verification methods."X" represents 'yes' for the corresponding range verification method. Adapted from Ref. 11.

Method	Commercially available	Existing in research environment	Requires further development	Expected accuracy < 1 mm
Implantable markers		X	X	X
Range Probe		X		X
Radiography		X		
PG imaging		X	X	X
PET imaging	X	X	X	
MRI imaging	X			X

Direct methods of *in-vivo* beam range verification include: *in-vivo* point measurements, the range probe, and proton radiography and tomography.[11] *In-vivo point dose measurements* have been widely used in photon and electron treatments.[12] Implantable dosimeters with

wireless readout are available and have been investigated for external beam radiation therapy, including prostate treatment.[13,14,15,16,17] Dosimetry verification systems (DVSs) (Sicel Technologies Inc., Morrisville, NC) are commercially available implantable dosimeters with wireless reading, and are metal oxide semiconductor field effect transistor (MOSFET)-based radiation detectors that are linear energy transfer (LET) dependent.[11,18] Hence, they do not measure a constant dose in the plateau of a conventional SOBP field, but this dependence may be used for range verification, requiring precise positioning of the dosimeters (since the DVS-dose curve becomes steep only near the distal end of the SOBP) and an absolute calibration of the MOSFET detectors.[11] Using implantable dosimeters allows for range verification during the delivery of the treatment, with no additional time for the patient being required, while giving the same dose distribution as planned. However, the forms of the individually delivered fields must be modulated to allow for the range measurement, to account for the non-tissue equivalence of the detector.[11] Limitations of this method include; verifying the range at a limited number of points, the dosimeters must be inserted into the target volume, and the implantation of markers may not be possible for many tumor types.[11,19] Further research in clinical scenarios is required to confirm submillimetre accuracy of this method found only in phantom tests.[11]

The range probe method has a high energy proton pencil beam passing completely through the patient, and its integral BP (residual range) measured on the exit side using a multi-layer detector. This method can provide useful information on the accuracy of range calculations *in-vivo* by comparing the measured integral BP with that calculated based on the patient's planning CT. For homogeneous regions, range resolutions of 1 mm may be possible with a detector thickness of 4 mm, while for heterogeneous regions, patient setup errors in the treatment position may be detected from changes of the BP shape.[20] An advantage of this method is that it is relatively simple, and requires only a commercially available multiple layer ionization chamber (MLIC) as a detector.[11] Also, high-resolution range verification appears to be feasible.[20] Disadvantages of this method include; the need for high energy proton beams, poor spatial resolution, and only the total range change through the entire patient can be measured, not the range at the tumor position.[11]

Proton radiography is the 2D extension of the range probe concept, where the position and energy loss of protons after traversing a material are measured. Here, a 2D fluence of protons is used, where the entrance and exit coordinate of each single proton is detected in coincidence with the range measurement to determine the residual range, and to achieve improved spatial resolution.[11,21] This method offers an *in-vivo* range measurement that may be

employed for treatment planning as well as range verification during the course of treatment.[11] The major disadvantage of proton radiography is the limitation in spatial resolution due to multiple Coulomb scattering (MCS).[21] Additional measurements of the proton incident and exit angle, and increasing the proton energy, are methods of improving the spatial resolution.[11,21] Inaccurate computed tomography (CT) Hounsfield Unit to relative stopping power conversions (HU-RSP) presents a major uncertainty in determining the proton range, yet proton radiography will allow for this conversion as it produces maps in units of water-equivalent path length (WEPL). A 3D map of the patient RSP can be produced from the reconstruction of individual proton radiographic projections, referred to as *proton CT*.[22] Hence, *proton tomography* allows direct measurement of relative electron density and stopping power for range verification, while proton CT can improve the accuracy of dose calculations for treatment planning, and be useful for pre-treatment verification of patient positioning relative to the proton beam.[23,24] The transmission images are true proton-beam's-eye-view projections since they can be taken exactly under the same geometrical conditions as for the treatment.[21] Furthermore, these images provide high tissue contrast, while the low dose can allow imaging for each fraction and could be used to detect anatomical changes during treatment. This method is currently not clinically used for range verification despite its potential, where further research and investigation is necessary for clinical implementation.[11]

Indirect methods for *in-vivo* beam range verification are mainly based on measurements of other signals such as secondary gamma rays, which are emitted as a result of nuclear interactions of the proton beam with target nuclei in tissue during the treatment. Two types of gamma rays can be used for this purpose. One is PG rays from the decay of excited target nuclei to their ground state - this is referred to as the prompt gamma imaging method. The other type is coincident gamma rays from the production of positron-emitting isotopes (such as ^{11}C, ^{15}O, etc) that produce two 511 keV annihilation gamma rays - this is referred to as the in-beam positron emission tomography (PET) imaging method. Magnetic resonance imaging (MRI) is another indirect method of beam range verification.

Prompt gamma imaging is the beam range verification technique investigated in this thesis. When protons pass through tissue, they undergo nuclear reactions which result in the emission of gammas, which can be used for treatment monitoring. Coincident gammas from the production of positron-emitting isotopes, and PG rays from excitations of target nuclei, can be used.[25] As the energy of the protons decreases, the interaction cross section increases and proton inelastic interactions with target nuclei occur along the penetration path up to a few millimetres before the BP where the reaction cross section begins to drop such that the proton

energy falls below the Coulomb barrier threshold.[10] That is, after a proton-nucleus interaction, the nucleus is excited to a higher energy state, and decays by emitting a photon (prompt gamma). Hence, PG rays can be used to determine the proton range since their emission is correlated with the proton penetration path.[25] However, the fall-off of PG emission is not equal to the dose fall-off, so a consistent PG and dose distal fall-off difference is required for proton range verification.[26] The main advantage of PG imaging is the ability to perform 'real-time' verification of proton dose delivery. This is because PG rays are emitted almost instantaneously, within a few nanoseconds, following the nuclear interaction, and hence can be detected almost immediately. This can be seen in Figure 2, where the time scale of PG emission compared to PET gamma emission is depicted. As stated, PG rays are emitted from excited nuclei upon proton-nucleus interaction, hence emitted within a few nanoseconds. In comparison, positron annihilation gammas imaged in PET give a delayed signal, and hence it does not provide real-time range verification. Along with real-time monitoring, high accuracy of beam range verification, and the close correlation between the PG emission and proton range, other advantages of PG imaging are the absence of washout effects, on-line treatment monitoring without additional dose, discrete spectral lines in PG emission containing information of tissue composition, and high production yields of gammas.[9,11,25,26,27] However, PG imaging for range verification is clinically unavailable due to the absence of an optimized PG detection methodology and technology, yet various studies have been and continue to be pursued, and will be discussed in the next chapter of this thesis.

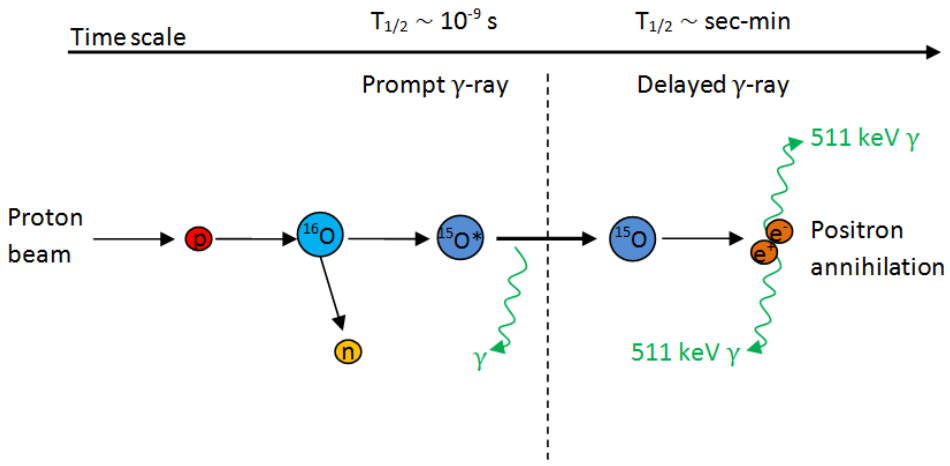

Figure 2: Schematic showing the time scale in emission of a prompt gamma ray (used in PG imaging) and coincident 511 keV gamma rays (used in PET imaging).

Positron emission tomography (PET) imaging uses coincident 511 keV gammas resulting from positron-electron annihilation. Positron-emitting isotopes, such as ^{11}C, ^{13}N and ^{15}O, are created from inelastic interactions of protons with atomic nuclei (nuclear fragmentation reactions) when traversing tissue. These isotopes are unstable and short-lived, and so they beta$^+$-decay (β^+-decay), whereby its mass is converted into energy, and emit two coincident gamma rays that can be imaged with a PET scanner.[26] For proton beams, β^+-activation only results from induced target fragmentation, in comparison to heavier ions where activation may arise from projectile fragmentation and target fragmentation.[28] Hence the activation is dependent on the elemental composition of the tissue, making the relationship between the induced activity distribution and dose distribution complicated, such that the same dose distribution delivered to different geometries of inhomogeneous tissue results in different activity distributions.[11,29] Also, the PET signal is from various radionuclides of different decay rates (half-lives), and the activity distribution changes with time, so PET imaging for range verification is sensitive to the time of data acquisition.[28] Moreover, charged particles deposit dose by imparting energy to atomic electrons through electromagnetic interactions, whereas positron emitter production involves nuclear reactions, therefore the PET activity distribution in PT is not correlated to the dose distribution.[28] That is, similarly to PG emission, the threshold energies for proton induced activations (β^+-isotope production) causes the activity distribution to fall before the proton dose fall-off.[30] Hence, the activity and dose distributions cannot be directly compared for direct range verification, and so PET measurements must be compared with predicted activity distributions.[28] Activity distributions can be predicted by using Monte Carlo calculations, or by a convolution of the dose distribution (distal fall-off region calculated by the treatment planning system) with a filter function.[11,31] PET imaging can be performed on-line (during irradiation) or off-line (a certain time after the treatment is completed).[30] On-line PET allows shorter imaging times (however gaining sufficient statistics is important), it minimises the effect of biological washout, and patient repositioning errors and anatomical morphological changes may be avoided or minimised since PET data are acquired with the patient at the treatment position.[11,28,30] On-line imaging has all β^+-isotopes contributing to the measured activity distribution, whereas off-line imaging has images primarily showing activity from radioisotopes whose half-life is similar to, or longer than the transportation and setup time (so is mainly restricted to ^{11}C).[11] Off-line PET is however advantageous because it does not require capital investment for the installation of a scanner in the treatment room, and has no impact on the patient treatment throughput.[28]

Magnetic resonance imaging (MRI) reveals changes in the constitution of human tissue caused by radiation, such as a characteristic pattern of fatty conversion in the vertebral bone marrow of the spine.[32] Thus, it presents the potential to observe radiation effects *in-vivo*. Visual inspection of MRI images alone is not sufficient to verify proton range since the location of greatest signal intensity (SI) gradient does not exactly correspond to the greatest dose gradient. Therefore, a relationship between dose and resultant MRI SI must be established to achieve proton range verification. A dose-SI curve for fatty marrow conversion has been established for a data set of 10 spine patients, and used to estimate range errors in the lumbar spine distal dose fall-off region.[32] Similarly, a conversion has been established with a data set of 5 patients with tumor in the liver.[33] Uncertainties remain due to the few patients in study. The advantages of MRI include its high spatial resolution, lack of additional ionizing radiation exposure, and availability of MRI scanners.[11] However, a firm dose-response relationship, and the minimum radiation dose required for fatty change, are still unknown.[32] Another challenge is the temporal evolution of the MR signal; in the hours to days post-irradiation, cellular depletion, marrow oedema, vascular congestion, and haemorrhage can occur and interfere with the MRI signal as a result of fatty replacement.[11]

1.2.2 Challenges of Prompt Gamma Imaging for Beam Range Verification

Recent studies have shown that the longitudinal distribution of the PG emission is correlated with the proton dose profile in the distal fall-off region.[25,34,35,36] This provides a rationale for the use of the PG signal for *in-vivo* verification of the proton dose delivery and range. However, from a physics point of view the PG emission does not have a strong correlation with the BP position since PG rays originate from different physics processes, as will be discussed. Significant research efforts are required to quantify the beam range uncertainty with the PG emission and detection.

PG imaging is an emerging *in-vivo* imaging technique that has the potential to overcome the limitations of *in-vivo* PET and promotes current *in-vivo* hadron beam range verification to track and monitor the BP position in real-time with the beam dose delivery. However, PG detection presents a great challenge since PG rays are generated from different nuclear reactions and have a broad energy range (between 2 and 15 MeV)[37] with strong interference background from neutrons and other stray radiation. Previous studies from many research groups are mainly focused on the feasibility of PG imaging[25,26,34,35], so further optimizing PG detection has become an important issue to improve PG imaging formation to reach the desired performance for clinical use. Unique advantages of PG imaging over other

methods for beam range verification include its ability to enable on-line treatment monitoring in real-time without additional dose, it provides high accuracy beam range verification of around 1 mm[25], and with close correlation between the proton range and the PG production position. Also, the discrete spectral lines in PG emission spectra contain information that may be used to determine elemental composition of irradiated tissue, which has been studied by some groups.[9,27]

1.3 Research Scope of the Thesis

This thesis study is confined in the specific scope to investigate the energy spectral, spatial and timing characteristics of PG emission signals deriving from a therapeutic proton irradiation as compared to its main interference background of neutrons by means of extensive Monte Carlo simulations. Optimal energy, angular and time-of-flight windows for PG imaging detection have been explored. Moreover, systematic modelling of the PG emission characteristics for imaging system design and development is performed. These will lead to developing optimal strategies of PG detection for real-time BP tracking in PT and support the development of clinically feasible PG imaging systems. The long-term goal of this project is to develop a novel *in-vivo* dose verification technique using the PG imaging method to enable on-line treatment monitoring for high-precision hadron radiation therapy.

Following this chapter, a literature review of PG imaging for range verification is presented in Chapter 2. Chapter 3 discusses the methodology adopted in this research. Chapter 4 then presents the results and their discussion.

Chapter 2

Literature Review

2.1 The Physics of Proton Therapy

2.1.1 Charged Particle Interaction with Tissue

Protons undergo two fundamental interactions with the atoms of the tissue they traverse and subsequently lose energy via *electromagnetic* and *nuclear* interactions. Electromagnetic interactions are Coulomb interactions with either the electrons or the nucleus of an atom, which results in significant energy loss of protons until fully stopped in the tissue. Nuclear interactions are proton-nucleus interactions which contribute significantly less to energy loss than the Coulomb interaction process. Yet nuclear interactions cause significant loss of beam fluence and the emission of various types of secondary particles such as gamma rays, neutrons and light fragments, which can be used for beam range verification. Figure 3 illustrates these interaction mechanisms.

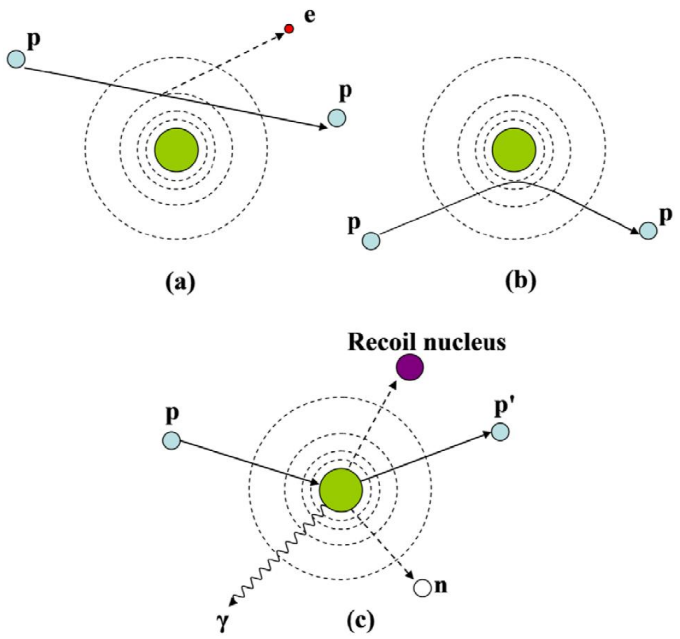

Figure 3: Illustration of proton interaction mechanisms: (a) inelastic Coulomb interaction leads to energy loss, (b) repulsive Coulomb elastic scattering with nucleus causes deflection of proton trajectory, (c) non-elastic nuclear interaction in which primary proton is removed and secondary particles are created. (p: proton, e: electron, n: neutron, **γ**: gamma ray). From Ref. 38.

That is, protons deposit energy in a medium through ionization and excitation, scattering, and nuclear interactions. The type of interaction between the proton and an atom in tissue depends on the proximity of the encounter. If the proton is at a considerable distance from an atom, its Coulomb force field affects the whole atom, distorting it and exciting it to a higher energy level, and occasionally ionizing it by ejecting a valence-shell electron.[39,40] If the proton closely passes an atom, it is likely to interact primarily with a single atomic electron, ejecting it from the atom with significant kinetic energy, called a delta (δ) ray (Figure 3(a)). These δ rays have enough energy to undergo additional Coulombic interactions, dissipating its kinetic energy along a separate track from the primary particle.[39] If the proton closely passes the atomic nucleus, it experiences a repulsive elastic Coulomb interaction which deflects the proton from its general straight-line trajectory (Figure 3(b)).[38] Furthermore, a charged particle can interact non-elastically with the atomic nucleus whereby the nucleus becomes excited and subsequently decays by emitting secondary particles such as protons, neutrons, gamma rays, and light fragments (Figure 3(c)).[38,41] The emission of gamma ray photons through de-excitation have energies that are essentially equal to the difference in energy between the initial and final nuclear states. Prompt gamma emission usually occurs without beta decay, depending on the reaction channel, but if so then the gamma rays will appear with a half-life characteristic of the parent beta decay but with energy reflecting the energy level structure of the daughter nucleus.[40] The spatial distribution of the absorbed dose is therefore altered by the presence of nuclear interactions, since some of the kinetic energy that would be deposited as local ionization and excitation is instead carried away by neutrons and gamma rays.[39] Table 3 summarises the proton interaction types.

Table 3: Summary of proton interaction types with target, ejectiles and influence on the projectile, with the corresponding dosimetric manifestation. Adapted from Ref. 38.

Type	Target	Principal ejectiles	Influence on projectile	Dosimetric manifestation
Inelastic Coulomb scattering	Atomic electrons	Primary proton, ionization electrons	Quasi-continuous energy loss	Energy loss determines range in patient
Elastic Coulomb scattering	Atomic nucleus	Primary proton, recoil nucleus	Change in trajectory	Determines lateral penumbral sharpness
Non-elastic nuclear reaction	Atomic nucleus	Secondary protons, neutrons, gamma rays	Removal of primary proton from beam	Primary fluence, generation of stray neutrons and prompt gammas

2.1.1.1 Energy Loss of Protons

The energy loss of protons in tissue can be quantified by the stopping power. The energy loss rate, or *linear stopping power* (S), for charged particles in a given absorber is the differential energy loss for that particle within the material divided by the corresponding differential path length[40]:

$$S = -\frac{dE}{dx} \tag{2.1}$$

In other words, this is the *rate* of energy loss, also termed *specific energy loss*[40], in units of energy/distance. The stopping power is defined for a beam, not an individual particle, so it describes the mean energy loss.[38] For particles with a given charge state, the linear stopping power increases as the particle velocity decreases, at energies relevant to proton therapy.[41]

As mentioned, electromagnetic interactions result in significant proton energy loss, and takes place through Coulomb interactions of protons with atomic electrons and atomic nuclei, so this energy loss can be expressed in two components:

$$S = S_{electrons} + S_{nuclei} \tag{2.2}$$

The *Bethe-Bloch* formula describes the specific energy loss/mean ionization energy loss (electronic stopping power), i.e. mainly $S_{electrons}$, taking into account quantum mechanical effects, and is written as[38,41,42,43,44]:

$$\frac{dE}{dx} = K\rho\frac{Z_p^2}{\beta^2}\frac{Z_t}{A_t}\left[\frac{1}{2}\ln\left(\frac{2m_e c^2\beta^2\gamma^2 T_{max}}{I_e^2}\right) - \beta^2 - \frac{\delta}{2} - \frac{C}{Z_t}\right] \tag{2.3}$$

$$K = 4\pi N_A r_e^2 m_e c^2$$

where Z_p is the charge number of the projectile, Z_t is the atomic number of the target material, ρ is density, β is the charged particle velocity relative to the speed of light (larger than the orbital electron velocity), N_A is Avogadro's number, r_e is electron radius, m_e is electron mass, A_t is the molar mass of the material, $\gamma = 1/\sqrt{1-1/\beta^2}$, I_e is the mean ionization potential of the material, δ is the density correction (for ultra-relativistic charged particles), T_{max} is the maximum kinetic energy that can be transferred to a free electron in a single collision, and C is a shell correction term (important when the particle velocity nears the velocity of the atomic electrons). Detailed discussion of the Bethe-Bloch formula can be found elsewhere.[38,41,42,43,44]

The variable β denotes the charged particle velocity in units of the velocity of light:

$$\beta \equiv \frac{v}{c} = \frac{pc}{E_{tot}} = \frac{\sqrt{E_{tot}^2 - m_0^2 c^4}}{E_{kin} + m_0 c^2} = \frac{\sqrt{E_{kin}^2 + 2E_{kin} m_0 c^2}}{E_{kin} + m_0 c^2} \tag{2.4}$$

where E_{kin} is the kinetic energy of the particle, E_{tot} is the total energy, m_0 is the rest mass, and p is momentum.[41] For example, for a proton with kinetic energy E_{kin} = 200 MeV, we can calculate that $\beta \approx 0.57$, given that the proton mass = 938 MeV/c^2. Hence, proton radiotherapy generally deals with moderately relativistic particles.[41]

Figure 4 shows the electronic stopping power as a function of kinetic energy of the protons, including the electronic and nuclear energy loss. As seen, the nuclear stopping power (from Coulomb interactions of the particles with atomic nuclei) occurs at low particle energy and contributes little to the total stopping power.[41] Different models are used to describe the stopping power curve depending on the kinetic energy of the protons, as seen in Figure 4. The Bethe-Bloch equation describes the energy loss when the charged particle velocity β is larger than the orbital electron velocity. At very low energies, when β becomes comparable or less than the orbital electron velocity, the energy loss becomes proportional to β, i.e. the Lindhard region.[45] The Bethe-Bloch and Lindhard regions can be joined by a polynomial, or the Anderson and Ziegler[46] low energy model can be used to describe the energy losses.[41]

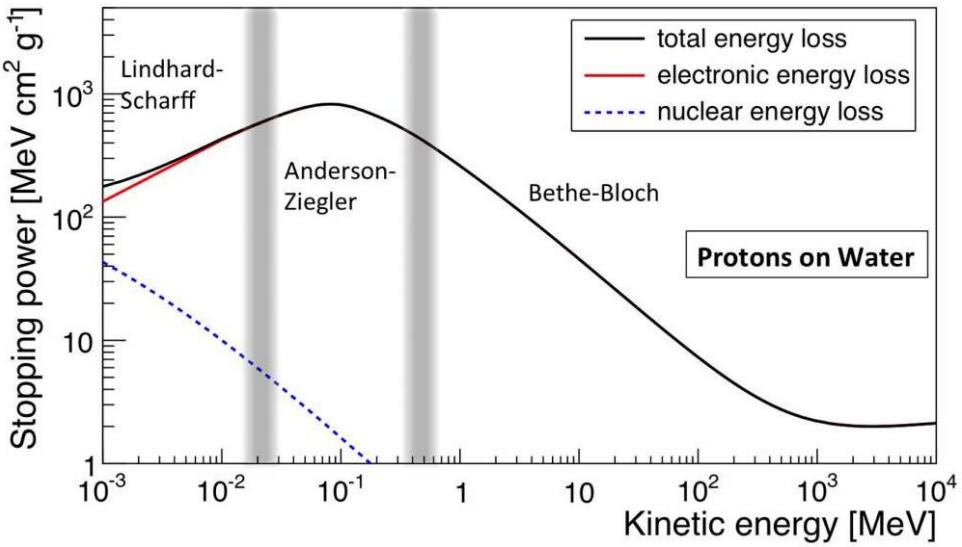

Figure 4: Stopping power of protons in water, with total, electronic, and nuclear stopping power shown. From Ref. 41.

The Bethe-Bloch formula describes the energy loss rate of charged particles along their track, which effects the shape of the Bragg curve. The first part of the Bragg curve (build-up region) corresponds to the stopping power whereby the energy loss is described by the Bethe-Bloch formula, where Coulomb interactions with outer-shell electrons of the material atoms are predominant. The formula shows that the energy loss is proportional to the inverse square of the proton velocity ($1/v^2$ classically and $1/\beta^2$ relativistically) and the square of the ion charge (z = 1 for protons), and there is no dependence on projectile mass. The linear stopping power is also proportional to the mass density, or the density of electrons in the absorber ($N_A \rho Z/A$), since the energy loss occurs by Coulomb interactions between protons and atomic electrons.[38] Other physical processes in the build-up region include the removal of some protons and the emission of secondary particles from nuclear reactions, and the accumulation of lateral deflections from multiple Coulomb scattering (MCS).[38] As the particle velocity decreases while traversing the medium, the interaction cross section increases, and the energy loss increases as described by the Bethe-Bloch formula, thereby causing the characteristic BP. The position and height of the peak are mostly governed by the stopping power and energy straggling, and to a lesser extent nuclear reactions and MCS (for very small fields).[38] In addition, as the particles slow down they get partly neutralized through electron pickup (from the target material), thereby reducing the particles' effective charge $\left(Z_p\right)_{\text{eff}}$ (which must replace Z_p in equation 2.3) and thus the Bragg curve displays a sharp fall-off as the particles lose all their energy and stop.[40,41]

The shape of the Bragg curve is also governed by the accumulation of many small variations in energy loss, which is a statistical or stochastic process.[38,40] Hence, there is a spread in energies after a beam of monoenergetic charged particles passes through a given thickness of absorber - the energy distribution width is a measure of *energy straggling*.[40] This phenomenon varies with distance along the particle track; initially the distribution width is narrow, but becomes wider and more skewed with penetration depth, and before the particle range the distribution narrows again due to the significant decrease in mean particle energy (see Figure 5). The same stochastic factors leading to energy straggling at a given penetration depth also result in a different total path length for each particle (i.e. the range of each individual particle deviates from the expected mean value), where *range straggling* is the fluctuation in path length for individual particles of the same initial energy.[40,41] That is, the lateral spread of the BP is due to energy straggling, while the longitudinal width (broadening) of the BP can be taken as a quantitative measure of range straggling. Although energy loss

from MCS is negligible, it too causes lateral broadening of the pencil beam and a reduction of the proton fluence on the central axis.[38,41]

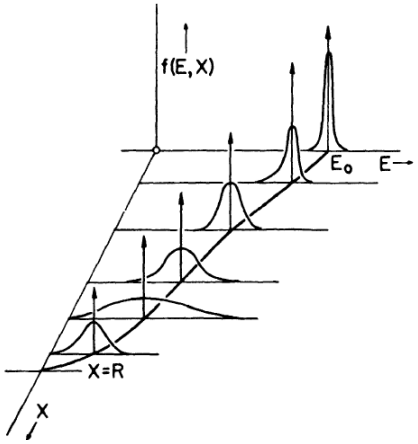

Figure 5: Plots of energy distribution of an initially monoenergetic beam of charged particles along penetration depth. E is particle energy, X is distance along the track. From Ref. 40.

2.1.1.2 Proton Beam Range

There are various definitions of range in the literature, the two main ones being the *mean range*, defined as the absorber thickness which reduces the particle count to half its value in the absence of the absorber (see Figure 6), and the *extrapolated range*, which is obtained by extrapolating the linear portion of the end of the transmission curve to zero. The range can also be defined as the distance beyond which no particles will penetrate.[40] Furthermore, it is convenient to think of the charged particle as losing its kinetic energy gradually, and so is often referred to as the continuous slowing-down approximation (CSDA).[39] The continuous ionization energy losses of charged particles are normally modelled in Monte Carlo codes analytically (down to ~2 MeV), based on a continuous-slow-down-approach (CSDA) that builds on the Bethe-Bloch equation, including relevant correction factors for Z_p.[41] So the range is essentially an average quantity defined for a beam, not for individual particles.[38]

Most protons have their path in matter as nearly a straight line, where on average the pathlength is almost equal to its projected pathlength and range.[38] Figure 6 demonstrates the relative fraction of the proton beam fluence remaining along depth in water. Nuclear reactions cause the removal of protons from the beam, where the sharp fall-off near the end of the range is due to ions being absorbed by the material when running out of energy. The distal fall-off presents a sigmoid shape due to stochastic fluctuations in the energy loss of individual protons, or range straggling[38], as discussed previously.

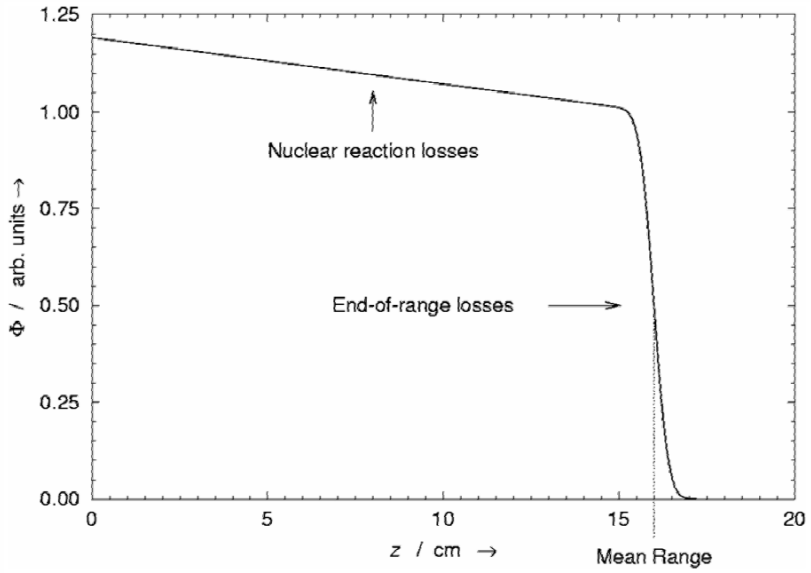

Figure 6: Relative fraction of fluence Φ in a proton broad beam remaining as a function of depth *z* in water. From Ref. 38.

The uncertainty in determining the range is an important concern in clinical PT, such as in calculating the settings of the treatment machine for patient treatment. The range uncertainty may depend on the knowledge of the proton beam energy distribution and on properties of all range absorbing materials in the beam's path such as elemental composition, mass density, and linear stopping power. CT scans used to convert image data from HU to linear stopping power present additional sources of uncertainty, such as CT scanner calibration imperfections, partial volume effects, motion artifacts, and streak artifacts.[38]

2.1.2 Nuclear Reactions of Proton Beam with Tissue

Non-invasive *in-vivo* beam range monitoring can be performed by detecting secondary radiation emitted from the target (patient) due to nuclear interactions of protons with tissue, such as β^+ emitters, PG rays, and charged fragments.[41] Protons need to have sufficient energy to overcome the Coulomb barrier of the nucleus to enter the nucleus, which depends on its atomic number. In the atomic nuclei of biologically relevant elements, the total inelastic cross section for proton-induced nuclear reactions has a threshold of the order of 8 MeV.[38] As discussed previously, nuclear interactions may be elastic or inelastic collisions. In elastic collisions, the kinetic energy is conserved, and the nucleus remains intact. They are due to strong rather than electromagnetic interactions, and although do not occur frequently they still cause broadening of the beam. Conversely, in inelastic collisions the total kinetic energy is not conserved, such that the nucleus is transformed and secondary particles (protons,

neutrons, alphas, etc) may be knocked out by the projectile. In PT, the emission of secondary particles is entirely due to the target nuclei.[41]

A proton striking an atomic nucleus initiates a series of nucleon-nucleon collisions, leading to the emission of protons, neutrons, light fragments, and to equilibration of the remnant nucleus. This involves three main stages; intra-nuclear cascade, pre-equilibrium, and de-excitation.[41] The *intra-nuclear cascade* (INC) (Generalised) model describes nuclear interactions of nucleons with energies above 50 MeV to hundreds of GeV, and forms the basis for nuclear interactions in the majority of Monte Carlo codes employed today. The incident particle interacts with quasi-free nucleons within the target nucleus (modelled as a Fermi gas of cold free nucleons) via a series of two-body interactions. A nuclear density distribution, a nuclear potential, and the Pauli exclusion principle, account for the nucleons inside the intra-nuclear medium. To justify this 'free' nucleon approach, the De Broglie wavelength λ_h of the incident particle must be much smaller than the average distance $\langle d \rangle$ between the nucleons in the material nucleus, and also much smaller than the mean free path λ_N within the nucleus:

$$\lambda_h = \frac{2\pi\hbar}{p} \ll \langle d \rangle = \left(\frac{3}{4\pi\rho_N}\right)^{1/3} \tag{2.5}$$

$$\lambda_h = \frac{2\pi\hbar}{p} \ll \lambda_N = \frac{1}{\sigma\rho_N} \tag{2.6}$$

where σ is the proton-nucleon cross section and ρ_N is the intra-nuclear density (normally 0.17 nucleons/fm^3 at the nuclei centre).[41] The time that a collision occurs must also be smaller than the time between the collisions, in order for them to take place independently. Secondaries are final state particles in the scattering process that are produced within the time-scale of strong interactions (10^{-22}-10^{-23} s). They have high energy and can scatter in the same nucleus, or escape it, etc. Among protons and neutrons, light nuclear fragments of high energy can also be emitted, through the *coalescence* mechanism, where emitted nucleons are grouped when they are near in phase space – the *intra-nuclear cascade* process.[41] In the *pre-equilibrium* stage, the particles in the cascade have reached the lower limit energy, but the nucleus is not yet in thermal equilibrium. The emission of protons, neutrons and light fragments leaves the residual nucleus in an equilibrium state, with the remaining nucleons sharing a certain excitation energy. These two stages discussed are often referred to as 'dynamic' stages, having an overall time scale of $\sim 10^{-22}$ s.[41]

Finally, the *de-excitation* stage, where the nucleus can dissipate its remaining energy in several ways (depending on the target nucleus mass and the energy remaining)[41]: nuclear

evaporation, where light fragments (such as alpha, He, etc) with a few MeV of kinetic energy can be emitted from the excited nucleus; fission, where the excited nucleus breaks into two fragments (high-Z nuclei only, Z ≳ 65); Fermi-breakup, where the excited nucleus disassembles into smaller fragments in one step (light nuclei, A ≲ 16, where the excitation energy may be greater than the binding energy of some fragmentation channels); and gamma emission, where a residual nucleus that remains after the previous stages is still somewhat excited, and so the final excitation energy is given off by emitting gamma rays. This stage is referred to as 'slow', usually 10^{-18}-10^{-16} s.[41] As is the scope of this thesis, PG rays are investigated for beam range verification, however positron annihilation photons will also be discussed for comparison.

The main effect of nuclear reactions during hadron therapy is the significant loss of beam fluence (as discussed in section 2.1.1.2). The number of particles remaining at a depth x depends on the inelastic nuclear cross section through the relationship:

$$P(x) = \frac{N(x)}{N(0)} = e^{-\frac{x}{\lambda_{int}}} \tag{2.7}$$

which is the probability of not having undergone a nuclear interaction after travelling a distance x in a material. $N(0)$ is the number of incident particles, $N(x)$ is the number of incident particles after a distance x, and the mean free path or interaction length is given by $\lambda_{int} = A_t/N_A\sigma\rho$, where σ is the total cross section.[41] This removal of primary protons causes a small decrease in the absorbed dose, which is largely compensated by the liberation of secondary protons and other ions.[38] Nuclear reactions also cause the modified dose distributions: the total energy deposition in the build-up region of the Bragg curve is considerably contributed by secondary particles; in heavy-ion irradiations, a dose tail is also delivered beyond the BP primarily due to forward scattered secondary particles from the nuclear reactions; and low energetic secondary particles (such as neutrons) are normally emitted at larger angles, contributing to the *low dose envelope* around the beam.[41] The production of various types of secondary particles is another consequence of nuclear reactions. High energy secondaries (that may exceed a hundred MeV) are mainly produced in the INC and pre-equilibrium stages, and are emitted mostly in the forward direction. Conversely, low energy secondaries produced in the de-excitation stage are emitted relatively isotropically in the centre-of-mass frame of the parent nucleus.[41] Three types of secondaries are employed for range monitoring in hadron therapy, β^+ emitters, PG rays, and charged fragments, however only the first two will be discussed here.

2.1.2.1 Positron Annihilation Photons

Positron-emitting isotopes such as ^{15}O, ^{11}C, and ^{13}N are created from inelastic interactions during proton irradiation.[47] When such a nucleus undergoes positron (e^+ or β^+) decay, the positrons typically travel only a few millimetres before losing their kinetic energy, and when their energy is very low, nearing the end of their range, they annihilate with electrons in the medium.[40] The original positron and electron then disappear, and replaced by two coincident 511 keV photons in opposite directions - termed *annihilation radiation*. This radiation is subsequently superimposed on gamma radiation that is emitted in the following de-excitation of the daughter product.[40] Table 4 lists nuclear reactions frequently occurring in PT that produce positron emitters.

Table 4: Nuclear reaction channels for positron emitter production. Adapted from Ref. 41.

β^+ emitter	Half-life (min)	Reaction channel	Threshold energy (MeV)
^{15}O	2.037	$^{16}O(p,pn)^{15}O$	16.79
^{11}C	20.385	$^{12}C(p,pn)^{11}C$	20.61
		$^{14}N(p,2p2n)^{11}C$	3.22
		$^{16}O(p,3p3n)^{11}C$	59.64
		$^{16}O(p,\alpha\ d)^{11}C$	27.50
^{13}N	9.965	$^{16}O(p,2p2n)^{13}N$	5.66
		$^{14}N(p,pn)^{13}N$	11.44

2.1.2.2 Prompt Gamma

Upon proton collisions with elemental nuclei in a medium, many nuclei are left in an excited state and de-excite by emitting neutrons or PG rays almost instantaneously ($<10^{-9}$ s)[48], hence providing the ability for PG imaging to offer a method of 'real-time' monitoring. That is, PG emission only occurs where the proton beam interacts in the material, thus the distribution of PG emission is correlated to the dose delivered.[48] As well, the close correlation between the proton range and the production of PG rays is such that nuclear reactions occur up to the last few millimetres of the track, where the proton energy falls below the Coulomb barrier threshold.[10] This close correlation can therefore enable verification of proton dose and beam range. Furthermore, PG rays have a wide energy spectrum, up to around 15 MeV[37], which are unique and characteristic to the element since the excited nuclear states are quantized. The discrete spectral lines therefore contain valuable information of tissue composition and elemental concentration for spectral analysis.[48] The major gamma emission lines that will be

considered throughout this thesis are: 511 keV annihilation photons, 2.22 MeV gammas from thermal neutron capture by hydrogen, 4.44 MeV PG rays from proton interactions with ^{12}C and ^{16}O, 5.21 MeV PG rays from ^{15}O, and 6.13 MeV PG rays from ^{16}O. Table 5 lists the nuclear reaction channels producing common gamma rays in PT.

Table 5: Nuclear reaction channels for gamma production. * represents a nucleus in an excited state, and χ represents spallation products (such as neutrons, deuterons, alpha particles, etc).[9] Adapted from Ref. 9 and 49.

Gamma energy (MeV)	Reaction channel	Mean life (sec)
2.22	$^{1}H(n,\gamma)^{2}H$	
4.44	$^{12}C(p,p')^{12}C^*$	$6.1x10^{-14}$
	$^{16}O(p,\chi)^{12}C^*$	$6.1x10^{-14}$
	$^{14}N(p,\chi)^{12}C^*$	$6.1x10^{-14}$
5.21	$^{16}O(p,\chi)^{15}O^*$	
6.13	$^{16}O(p,p')^{16}O^*$	$2.7x10^{-11}$
6.92	$^{16}O(p,p')^{16}O^*$	$6.8x10^{-15}$
7.12	$^{16}O(p,p')^{16}O^*$	$1.2x10^{-14}$

2.2 Current Research Status of Prompt Gamma for Beam Range Verification

The use of PG rays for range verification was first proposed by Min *et al* (2006), who reported the close correlation between PG distributions and the BP position within 1-2 mm accuracy for a 100 MeV proton beam in a water phantom. Since then, many authors have not only confirmed this result, but have performed simulations and experimental measurements to better understand the use of PG rays for beam range verification as well as detection methodology and detector technology improvements where custom-built prototype detector systems have also been developed. However, much research is still required to fully understand the use of PG rays for *in-vivo* range verification, and to overcome challenges in PG imaging detection technology.

2.2.1 Methodology Aspect

The feasibility of *in-vivo* PG range verification for monoenergetic proton pencil beams of clinical energies has been demonstrated.[25,34,35,50,51] The feasibility of range verification for passively scattered SOBP fields has also been demonstrated.[26,34] Hence, the strong correlation between PG ray emission and dose delivered during PT has been shown by many research

groups[25,34,35,36], and a close correlation between characteristic PG production and the proton SOBP dose distribution in homogeneous and heterogeneous media has also been found.[34] However, since the PG fall-off position is not 'equal' to the dose fall-off, a consistent PG-dose distal fall-off difference may be a key factor to enable direct correlation of the distributions.[26]

Extensive research has been performed into the characterisation of PG emission during proton irradiation of both homogeneous and heterogeneous media. The gamma spectrum has been studied by various authors, where the emission lines from specific nuclear de-excitations have been found to be: ^{16}O, single escape peaks 6.13 MeV and 5.62 MeV, double escape peak 5.11 MeV, and single escape peaks 2.74 MeV and 2.23 MeV; ^{15}O, single escape peaks 5.21 MeV and 4.70 MeV, and double escape peak 4.19 MeV; and ^{12}C, single escape peaks 4.44 MeV and 3.93 MeV, and double escape peak 3.42 MeV.[9] The 6.13 MeV PG emission was found to be directly proportional to the amount of oxygen in a volume of irradiated tissues, whereas the 4.44 MeV PG emission depends on both carbon concentration and oxygen concentration.[9] The relative intensity of gamma emission lines was found to be a function of both the elemental concentration and the physical density of the tissue. Regarding the discrete lines of ^{16}O, it has been shown that at low incident proton energies, gamma emission was highest from the first three excited levels (at 6.13, 6.92 and 7.12 MeV) to the ground state.[52] Although more low energy gammas are produced during irradiation, it is the high energy gamma rays that have been found to better discriminate the distal dose fall-off.[25,35] This is because high energy gamma rays experience less scattering when traversing and exiting the target, and their production has improved localisation with respect to the dose fall-off.[35] Moreover, due to the characteristic PG emission spectra dependent on the material composition of the media traversed by the protons, the PG signal can possibly be used to determine the elemental composition of the irradiated tissues.[9,27,34]

Critical issues of the use of PG emission in PT range verification have been identified. First, standard collimated detection systems are unable to efficiently measure high energy gamma rays (up to 8 MeV), and second, detectors have limited ability to accurately determine the location of emitted gamma rays within the irradiated volume.[27,34] Thus, the need to develop experimental systems designed to measure the characteristic gamma rays, as well as potential detector designs for range verification have also been noted.[27,52] Polf *et al* (2013) report the need to "develop efficient and accurate PG detection or imaging systems capable of working in a proton treatment vault, obtain a full understanding of the spatial characteristics of PG emission around the patient, and understand the relationship between PG emission and the density and elemental concentration of the irradiated tissues."

New methods of range verification and techniques to overcome such challenges of PG detection in hadron therapy have been explored by many research groups, such as time-of-flight techniques.[53,54,55] An unconventional method of range assessment through prompt gamma timing (PGT) has been explored, which is based on an elementary physical effect where protons penetrating tissue have a transit interval of time from entering the patient until stopping in the target volume.[55] In the case of protons with a 5-20 cm range, a 1-2 ns transit time has been determined. The transit time increases with the particle range, causing measureable effects in the PGT spectra, and hence useable for range verification. In this study, the PGT spectra are distributions of the time difference between a reference time, such as the target entrance of the beam, and the PG ray arrival time at the detection system. Kinematical relations were used to describe the relationship between PG emission and resultant time profiles. Here, the emission energy window was determined to be between 4.3 and 4.5 MeV.[55] The proton transit time was shown to be directly correlated to and measureable with statistical moments such as the mean μ and standard deviation σ of PGT spectra, and showed the precise yield of proton transit time from the PGT approach and hence the measurement of the proton range. Figure 7 shows the correlation between PGT statistical moments μ_γ and σ_γ and the proton range found from this group's study. Range variations of 2 mm were expected to be clearly detectable by means of this novel proposed method.[55]

In another study, a time-of-flight (TOF) technique to reject the neutron background of PG imaging to improve the accuracy of range verification by means of a shifting TOF acceptance window which accounts for proton propagation through the patient has been proposed.[54] It was found that for a narrow angular collimation window, the PG profile displays a steep fall-off that is well correlated with the BP, whereas a wider window allows for gamma spatial profiles to be detected while still presenting a fall-off correlating with the BP position. Results also showed that TOF windows having a width of about 1.0 ns allow almost all PG rays to be detected while accepting very few neutrons.[54] In this study, Monte Carlo codes predicted that even at a proton energy of 200 MeV, more than 99.6% of neutrons are ejected in the region of initial entrance up to the range of the proton. Thus, a shifting TOF window of appropriate width can in principle eliminate almost all neutron background within the longitudinal ROI.[54] Figure 8 shows the distribution yield of PG rays and neutrons registered in the detector as a function of longitudinal distance with the shifting TOF window applied, from this group's study. The difference between calculations with Geant4 and MCNPX as seen in this figure indicate large discrepancies between the algorithms used by the two codes in simulating proton-induced nuclear reactions.[54] Geant4 was found to give the lowest gamma-to-neutron

ratio and therefore representing the worst possible starting scenario, hence this group focused mainly on the Geant4 simulations, but the conclusions derived for the Geant4 code were also assumed valid for the MCNPX simulations.[54] TOF techniques such as this, that differentiate the PG signal from the background, do not only improve the PG signal-to-noise ratio, but could also eliminate the need for bulky shielding around the detectors in clinical applications.[11]

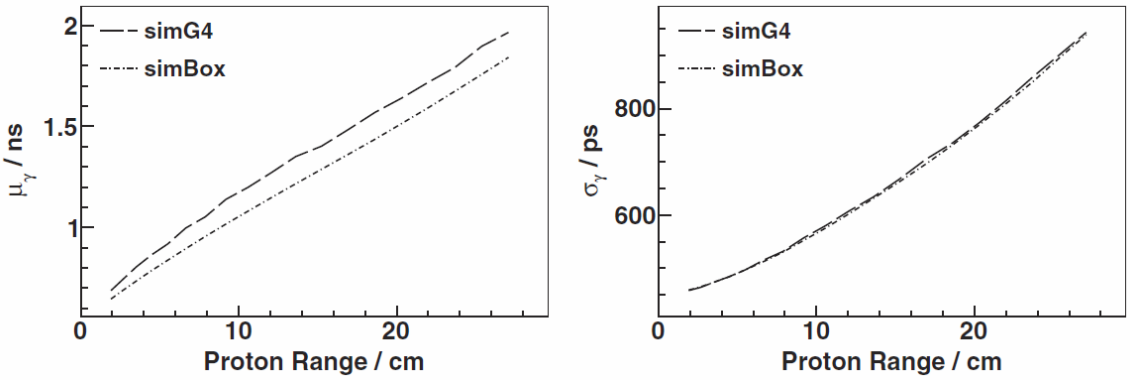

Figure 7: Range-dependent mean value $\boldsymbol{\mu_\gamma}$ (left) and standard deviation $\boldsymbol{\sigma_\gamma}$ (right) of modelled prompt gamma ray PGT spectra. Target material is PMMA. Proton energies are in the range of 50 MeV up to 230 MeV, corresponding to proton ranges of 2 cm up to 27 cm. The assumed system time resolution is 450 ps. From Ref. 55.

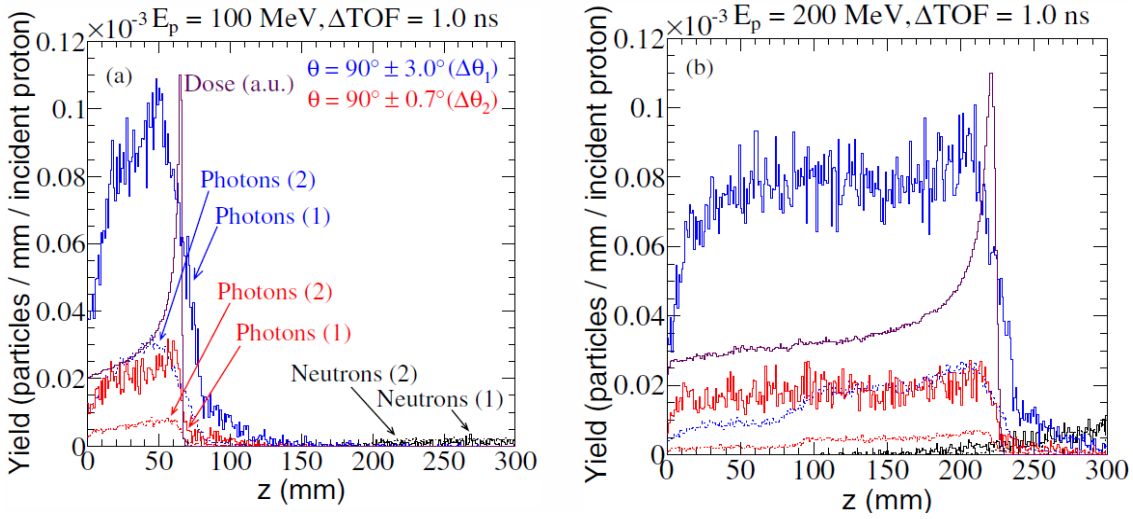

Figure 8: PG (blue and red) and neutron (black) yield registered in detector as a function of longitudinal distance *z*. Depth-dose profile in PMMA phantom (purple), in arbitrary units (a.u.), was calculated with Geant4. Mono-energetic beams of (a) 100 and (b) 200 MeV. Shifting time window of 1.0 ns is applied. PG profiles are shown for the small angular collimation windows $\Delta\boldsymbol{\theta_2}$ (red) and $\Delta\boldsymbol{\theta_1}$ (blue). Data obtained with Geant4, denoted as (1), and MCNPX, denoted as (2). Bin width is 1 mm. From Ref. 54.

2.2.2 Current Technology for Prompt Gamma Detection

Various detectors and camera types have been investigated for imaging PG rays, such as collimated PG cameras[10,25], pinhole cameras[56], slit cameras[57], gamma cameras[10], Compton cameras[58] and double-scattering Compton cameras[50,59]. For example, Min *et al* (2006) constructed a multilayered collimator system to locate the dose ends by measuring PG rays while moderating and capturing fast neutrons, and preventing unwanted gammas from reaching the scintillation detector. The PG distribution peaks were found to correlate well with the Bragg peaks, within 1-2 mm difference in position at 100 MeV.[25] Although collimated PG cameras are the most straightforward approach, the neutron background and stray gammas have presented a challenge in early setups, requiring thick layers of collimation.[11] However, Monte Carlo simulations have implied that array-type setups would allow PG measurements from therapeutic proton beams.[60] In comparison, the measured position and energy of scattered electrons and photons have been used to reconstruct the location and direction of incident gammas by means of Compton scattering kinematics.[61] The system could be employed for monitoring the precision of fractionated therapy in terms of accurately relocating the distal dose fall-off, and the fast timing coincidence of this method is promising compared to the use of a multi-grid collimator since background radiation during therapy is significant.[61]

In another study, a pinhole camera was designed to image useful gammas while shielding stray gammas and neutrons.[56] Both shape and position of the aperture were chosen in order to view the endpoint of the proton range, while the pinhole itself was shaped such that a suitable quantity of gamma rays transmitted through the hole for therapeutic proton beams. A shift in the peak of the overall gamma distribution of 0.2 mm was observed for an energy variation of 1 MeV. This study shows that pinhole cameras may be a simple and viable tool for verifying the accuracy of the dose deposition in a patient, when the therapy beam range is less than a few centimetres.[56]

A slit camera has also been developed and tested for real-time range control during PT.[57] The PG camera with slit collimator allows a one-dimensional projection of the beam path on a scintillation detector to be obtained. It was found that the photon profile sharply decreases at the BP, such that photons mostly produced by primary protons along the beam path are emitted isotropically and not heavily influenced by scattering prior to leaving the target, thus their fluence indicates the beam range. Also, photons of energy between 4 and 5 MeV were found to provide the most useful information for identifying the range.[57] A first prototype slit camera using the HiCam system was also prepared and tested; a compact Anger

gamma camera with modular structure based on arrays of five square silicon drift detectors (SDD) of 1 cm^2. A 1-2 mm standard deviation on the range estimation was achieved with the slit camera.[57] A position-sensitive gamma camera in combination with a knife-edge-shaped slit placed perpendicular to the beam direction has also been explored.[10] The knife-edge-shaped slit provides a larger field-of-view than parallel-edge slits, and a higher photon collection efficiency can be obtained compared with a pinhole camera. As well, only a one-sided access of the camera to the patient is required compared to PET systems, washout issues are avoided, and the slit width can be adjusted so that the system efficiency and resolution can be optimized. It was shown that under common therapy conditions for proton spot scanning, sufficient data may be collected during one spot-step (∼10 ms) to locate the distal dose edge with a 1σ accuracy of better than 1 mm.[10]

Compton cameras are emerging as a more suitable method of *in-vivo* PG range verification. They are multistage detectors which measure the energy deposited and position of each gamma ray interaction while scattering in the various stages of the camera.[37] Compared to collimated gamma cameras, Compton cameras yield an increased efficiency of potentially up to two orders of magnitude since performance-limiting absorbing collimators are replaced by an electronically operating collimator.[11] A Compton camera design for 3D *in-vivo* dose verification from in-beam single photon emission computed tomography (SPECT) during proton beam irradiation has beenevaluated.[58] The angular resolution and efficiency was studied, and it was found that a cadmium zinc telluride (CZT) system may be adequate, with the construction of a semiconductor scintillator hybrid system under way.[58] Double-scattering Compton cameras enable direct analytical reconstruction, and yield an improved spatial resolution.[11] A three-stage Compton camera has been investigated, with the purpose to develop the camera specifically designed to measure PG rays emitted from tissue, and determine its feasibility to measure and image PG rays emitted during proton beam irradiation.[50] Geant4 was employed to model three high-purity germanium detector stages arranged in parallel-plane geometry. To determine the lateral width and thickness of the detector stages that presented the best detection efficiency, an isotropic gamma source (0-15 MeV) was used. The overall efficiency of the camera was then determined with a proton beam irradiating a tissue phantom (replacing the gamma source). Overall efficiencies varied from $\sim 10^{-6}$ to 10^{-3} PG rays detected per incident proton, and it was concluded that a three-stage Compton camera could indeed be used for PG measurement and imaging during PT.[50] To minimise the radiation damage that results from neutrons, as well as the cost, and the need for cryogenic coolants in the case of high-purity germanium, room-temperature alternatives

such as CZT and Cerium Bromide ($CeBr_3$) would be more suitable. For example, CZT is a semiconductor detector which offers good energy resolution for high energy gamma rays, yet it does not offer high sensitivity for high energy gamma rays, nor it is good for timing measurements. On the other hand, $CeBr_3$ is a scintillator which offers good energy resolution, excellent sensitivity and timing for high energy gamma measurements. The feasibility of utilising the stochastic origin ensemble (SOE) algorithm for reconstructing images provided by a three-stage Compton camera measuring secondary gamma emission during PT has also been studied.[37] The effectiveness of this method for reconstructing proton pencil beam images and for modelling the distal fall-off of secondary gamma emission in PT was affirmed.[37]

The challenge to develop a PG imaging system capable of measuring the range with both accuracy and sufficient statistics for clinical use has been identified.[57] Furthermore, there is the need for a method of verifying the *in-vivo* beam range, to allow treatment margin reductions, and the ability to fully exploit the advantages of PT.[37] Again, detectors that are capable of efficiently imaging the high energy gamma rays and collimation techniques to effectively measure these PG rays require further research, as well as an improved understanding of the correlation between secondary gamma emission and the dose distribution in homogeneous and heterogeneous materials.[37]

2.3 Prompt Gamma Method: Issues Which Require Further Research

Despite the advantage in PG detection for PT range verification (see section 2.2), remaining challenges include the need for a real-time range verification technique during treatment delivery, a novel imaging detector for PG detection, background suppression for detector instrumentation, a novel imaging reconstruction algorithm, etc. In particular, there is the need for detectors to efficiently measure high energy gamma rays.[27,34,37,52] There is the challenge to develop a PG imaging system capable of measuring the range with accuracy and sufficient statistics for use in clinical routine.[57] There is also the need to fully understand the spatial characteristics of PG emission around the patient and the relationship between PG emission and the elemental concentration of the irradiated tissues[9], and the need to improve understanding of the correlation between secondary gamma emission and the dose distribution in homogeneous and heterogeneous media.[37]

Chapter 3

Methodology

The goal of this project is to characterise the spectral, spatial and timing characteristics of PG emission in a variety of phantoms, modelling the patient, to propose strategies which will aid the design and development of an optimal PG detection system for hadron therapy applications. A Geant4 Monte Carlo application was developed in the context of this thesis to calculate the PG emission produced by a 200 MeV proton pencil beam irradiating alternatively a water phantom and a standard PMMA phantom, which are used in clinical Quality Assurance.

Nuclear interactions along the proton track not only result in the emission of PG rays, there is also a significant contribution of neutrons emitted, produced by the incident protons in the phantom. Hence, neutrons contribute to the background signal and present a challenge for optimal PG image formation. Thus, the PG energy spectrum, yield and the correlation between the PG emission and the BP position have been extensively studied and compared to the background signal, produced by such secondary neutrons. Both cylindrical and cubic phantoms were adopted to study the effect of alternative phantom shapes on the PG signal. Cylindrical and cubic phantoms are widely used in the clinic for Quality Assurance purposes. The angular emission of PG rays was calculated with respect to the centre of the coordinate system of the Geant4 simulation. The timing properties of PG rays leaving the phantoms were studied at a certain distance from the phantom, corresponding to the realistic distance of the detector to the patient. Furthermore, modelling of the PG detection was studied in an ideal BGO detector by means of the simulation. Thanks to the methodology used in this research project, the simulation study will support the determination of an optimal energy window, angular position, and time window for PG detection in a BGO detector. The findings of this thesis will potentially aid in imaging system design and development, and determining an optimal methodology for PG detection for PT applications.

3.1 The Monte Carlo Simulation Application

The Monte Carlo simulation Toolkit GEANT4 version 10.00 was adopted in this study. Geant4 is a Monte Carlo code written in C++ and using the Object-Oriented Technology for

simulating the passage of particles through matter.[62] It is used from High Energy Physics to medical physics, nuclear and accelerator physics, as well as space science. Geant4 provides a complete set of tools for radiation physics related problems, including extensive physics capability coupled with powerful geometry functionality. It has other components such as tracking, detector response modelling, visualisation, event biasing techniques, analysis, etc.[63]

Figure 9 shows the simulation geometrical configuration. A 200 MeV proton pencil beam is the incident radiation for all simulations, unless otherwise stated. The beam originates at the phantom surface, i.e. it does not travel through air before entering the phantom.

Cylinder and cube geometry phantoms of water and PMMA were studied as alternative options, as these are typical phantoms for Quality Assurance in radiotherapy, modelling the patient. The PMMA (Polymethyl Methacrylate, $C_5O_2H_8$) was modelled with a density of 1.19 g/cm^3.[64] The cylinder phantom had a size of 50 cm along the direction of the proton pencil beam and a radius of 15 cm (see Figure 9). The cube phantom had a size of 30x30x30 cm^3. In both phantom geometries the proton pencil beam was incident normally to the phantom surface.

Electromagnetic (EM) (Livermore Low Energy Package) and hadronic physics processes are modelled in this study. HadronPhysicsQGSP_BIC_HP and HadronElasticPhysicsHP describe the inelastic and elastic nuclear scattering of protons, neutrons and pions. The HP data libraries model neutron interactions between thermal energies and 20 MeV. The IonBindaryCascadePhysics models the inelastic hadronic interactions of ions.[65] The production threshold of secondary particles was fixed to 1 mm. The Radioactive Decay and Decay Physics component are modelled as well. Validation of the Geant4 nuclear interaction cross-sections of high energy proton beams with low atomic number materials has been performed in other work.[66]

The energy deposition was calculated in the phantom along the direction of incidence of the protons to verify that the BP is at the expected position.

The energy, position and time of generation of gamma rays in the phantom was retrieved from the simulation. The time was calculated starting from the generation of the incident proton. The same physical quantities (energy, position, and time of generation in the phantom) were retrieved for secondary neutrons as well.

The 'detection sphere' and 'detection cylinder' were modelled as alternative solutions to study the energy spectrum and the angular emission of PG and neutron fields emerging

from the phantom, at a realistic distance of a possible detector from the phantom itself. More details are provided in section 3.2. The global system of coordinates refers to the whole Geant4 experimental setup.

Since the neutron background signal is always present during PT, the yield ratios of gamma rays to neutrons presented in our results are taken as the number of gamma rays per incident proton within the energy window of interest to the total number of neutrons per incident proton.

To achieve a statistical uncertainty adequate for the object of the study, between $1x10^7$ and $5x10^7$ events were executed when calculating the PG detection at a defined distance from the phantom. One event corresponds to one incident proton on the phantom. When simulating the response of a BGO detector, $1x10^9$ events were generated to ensure a 1σ statistical uncertainty of less than 10% (see section 4.3.1 for this estimation).

3.2 Characterisation of the Prompt Gamma Emission Field

To study the angular emission and timing properties of the PG emission, a dummy air-filled sphere was introduced containing the phantom with a radius of 50 cm. Figure 9 shows this setup for the cylindrical phantom. The centre of the sphere corresponds to the centre of the phantom. In the setup established in the simulation, φ represents the angle of the gamma/neutron with respect to the z-axis (the axis along the length of the phantom, or the beam direction axis), whereas θ represented the angle of the gamma/neutron with respect to the x-axis. This relationship was established with the knowledge of spherical coordinates:

$$z^* = \rho cos(\varphi) \tag{3.1}$$

$$x^* = \rho\ sin(\varphi)\ cos(\theta) \tag{3.2}$$

$$y^* = \rho\ sin(\varphi)\ sin(\theta) \tag{3.3}$$

Here, ρ represents the radius of the sphere (ρ = 50 cm), and * symbolises the position in Cartesian coordinate of the gamma/neutron when reaching the detection sphere. $\gamma(x^*, y^*, z^*)$ and $n(x^*, y^*, z^*)$ were retrieved from the *G4Track* information at the position where the gamma/neutron were crossing the boundary of the detection sphere.

The kinetic energy of the particle in MeV was retrieved, as well as φ and θ in degrees, by rearranging equations 3.1, 3.2, and 3.3:

$$\varphi = arcos(z^*/\rho) \tag{3.4}$$

$$\theta = arcos(x^*/\rho\ sin(\varphi)) \tag{3.5}$$

$$\theta = arcsin(y^*/\rho\ sin(\varphi)) \tag{3.6}$$

That is, θ can hence be determined with the use of x^* or y^*. In the histograms produced and displayed in this study, x^* was employed for convenience.

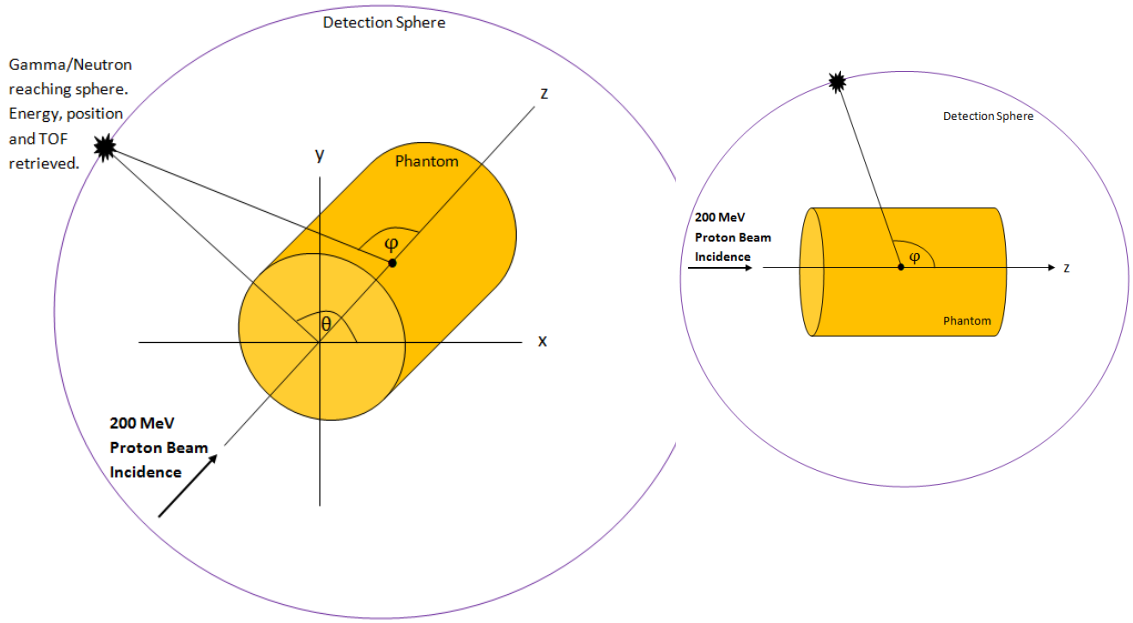

Figure 9: Simulation setup illustrating the coordinate system of the detection sphere with respect to the centre of the sphere (centre of phantom), with axes labelled. $\boldsymbol{\varphi}$ represents the angle from the z-axis, while $\boldsymbol{\theta}$ represents the angle from the x-axis. For the cubic phantom simulations, the cylindrical phantom is replaced with the cube phantom.

The sensitive detection sphere was then replaced with a detection cylinder coaxially surrounding the phantom, being the same length as the cylindrical phantom and with a radius of 50 cm, depicted in Figure 10. By doing this, the spatial distribution (the angular distribution in the case of the detection sphere) and timing information of the PG emission reaching the sensitive detection cylinder can be directly related to the Bragg curve since the results can be displayed on a position (z-axis) scale to compare with the phantom data of the same scale. Note that in the detection sphere setup, both cylinder and cube geometry phantoms are used, whereas only the cylindrical geometry phantoms are used in the detection cylinder setup.

The air-filled cylinder detector was modelled with an inner radius of 50 cm and outer radius of 51 cm.

The detection sphere/cylinder were introduced to determine an optimal angular preference for the PG detection, in comparison to neutrons, with the goal of improving the signal-to-noise ratio for optimal imaging formation and aid in detection system development.

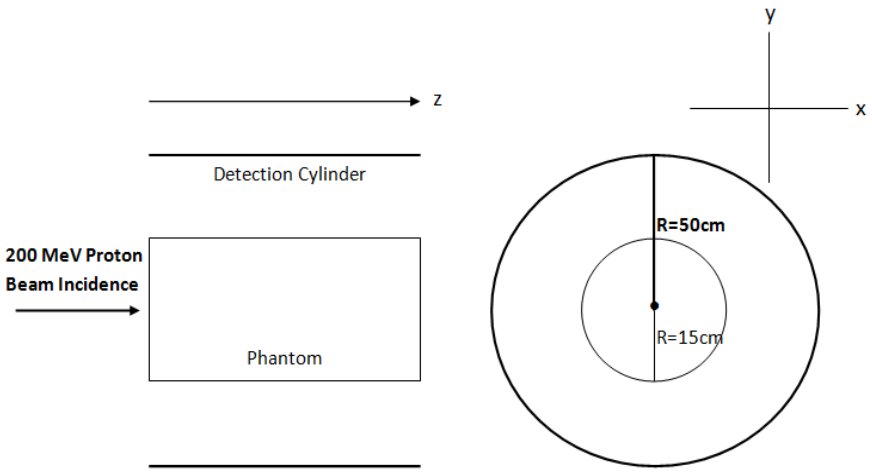

Figure 10: Setup of the sensitive detection cylinder coaxially surrounding the phantom, with 50 cm radius and same length as the phantom (50 cm).

The time from proton incidence to the detection of the gamma/neutron at the detection sphere/cylinder, denoted as TOF (time-of-flight) in Figure 9, was also retrieved from the simulations, in nanosecond units. This was achieved by using the *Global Time* information available in the *G4Track* class of the Geant4 toolkit. The timing properties of the PG rays and neutrons emitted from the phantom were studied and compared in order to determine an optimal time window or, eventually, a timing method to further improve the PG signal-to-noise ratio for optimal imaging formation.

3.3 Modelling Prompt Gamma Detection with an Ideal Detector

Once the optimal energy window and angular emission were determined by means of the detection sphere/cylinder, the response of an ideal BGO detector to PG signal was modelled in the simulation. The BGO detector was set in the optimal position to improve the signal-to-noise ratio as calculated in the first part of the project (see sections 3.1 and 3.2). The distance of the BGO detector from the centre of the phantom was 50 cm, corresponding to the

radius of the detection sphere/cylinder. The BGO scintillator ($Bi_4Ge_3O_{12}$, ρ=7.13 g/cm^3)[67] is a box of size 45x45 mm^2 facing the phantom and 25 mm length, as shown in Figure 11. The detector is located perpendicular to the phantom, i.e. at 90^o to the z-axis, where most gamma emission was found to be present, and positioned with face directed toward the phantom. In this study, only the cubic PMMA phantom is used. In order to yield a statistical error less than 10%, 5x10^7 primary protons were simulated 20 times, to obtain 10^9 events in total when the results were merged. The detector response is calculated as the total energy deposition per event.

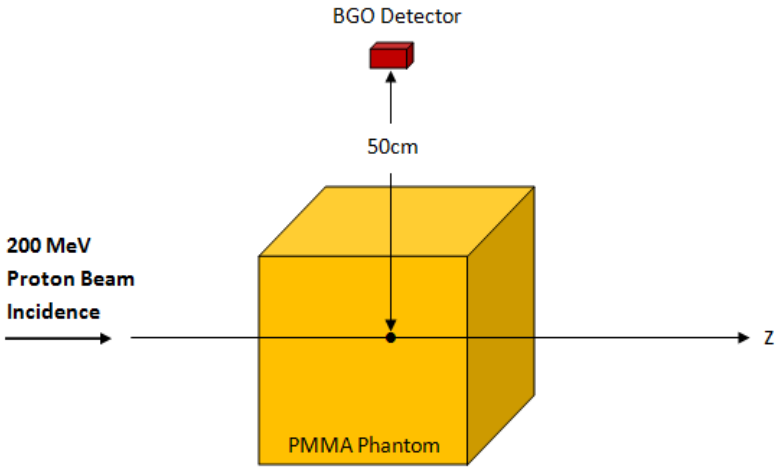

Figure 11: Simulation setup of the BGO detector.

Chapter 4

Results and Discussion

4.1 Characterisation of Prompt Gamma Emission in Proton Therapy

While investigating the emission of PG rays for on-line tracking of the BP in PT, the energy deposition of the 200 MeV proton beam in water and PMMA was calculated. Figure 12 shows this energy deposition (Bragg curve) in the cylindrical water phantom and PMMA phantom used in this study. The proton range (taken as the 50% fall-off of the BP) in water for a 200 MeV proton beam is found to be approximately 26 cm, which agrees with other publications within the simulation statistical uncertainties.[61,68,69] The range of the 200 MeV proton beam in PMMA is found to be around 22 cm, also agreeing with publications within 5%.[54] These range values are in good agreement with those from NIST within the simulation statistical uncertainties.

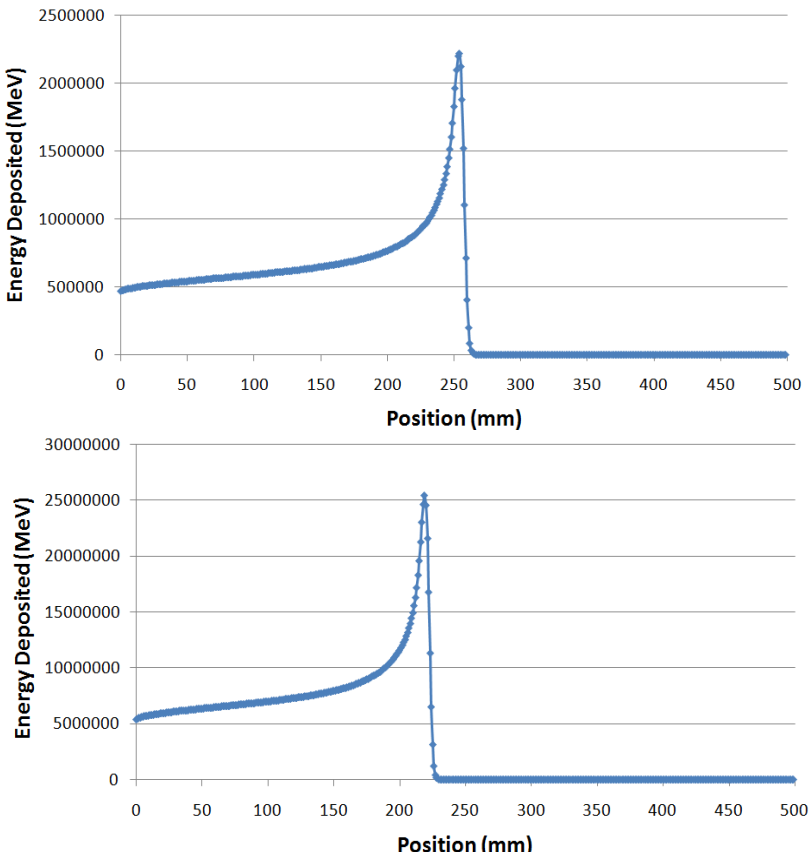

Figure 12: Bragg curve of a 200 MeV proton beam incident on the cylinder target phantom. Top: water phantom. Bottom: PMMA phantom. $1x10^7$ events were executed.

4.1.1 Energy Spectral Characteristics of Prompt Gamma in Proton Therapy

The PG emission does not correlate exactly to the dose, as the energy deposition is dominated by electromagnetic processes, while PG rays are emitted from nuclear reactions.[57] Figure 13 shows the energy distribution of the gamma rays with respect to the depth in the cylindrical phantom, where they originate. The BP is located at a depth of about 25 cm in the water phantom, corresponding to Position z = 0 mm in the figure. In the PMMA phantom, the BP is located at a depth of about 22 cm, which corresponds to Position z = -30 mm in the figure. The dashed yellow line in the figures represents the approximate BP position. We find that gamma rays are emitted along the entire phantom, with those of energies ~0.511, 2.22, 4.44, 5.21, and 6.13 MeV being most prominent. The 4.44, 5.21, and 6.13 MeV gammas are *prompt* gammas, such that they arise from the de-excitation of atomic nuclei of ^{12}C, ^{15}O, and ^{16}O, respectively. Hence, these gamma energies will be the focus of this study to determine an optimal energy window for improved PG image reconstruction. In comparison to PG rays, neutrons have a much wider energy spectrum, ranging from thermal energy up to the proton energy where there is a head-on collision. This is seen in Figure 14.

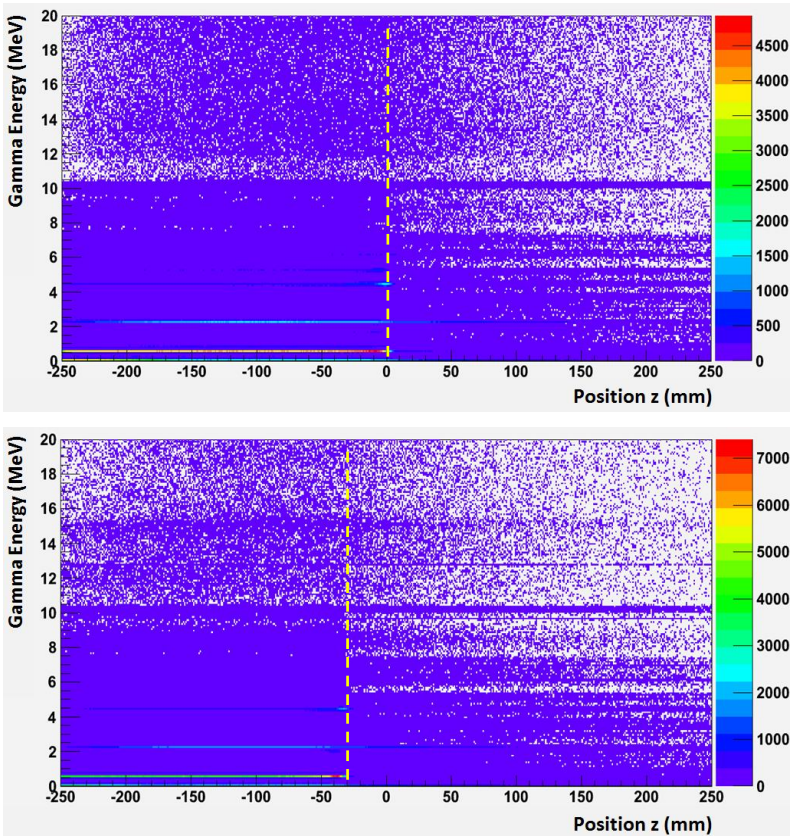

Figure 13: Gamma kinetic energy with respect to the position of origin in the cylinder phantom, along the z-axis. Top: water phantom. Bottom: PMMA phantom. The dashed yellow line represents the approximate position of the BP. The colour code represents the number of counts provided in the right-hand axis of each figure. $1x10^7$ events were executed. Data obtained with Geant4.

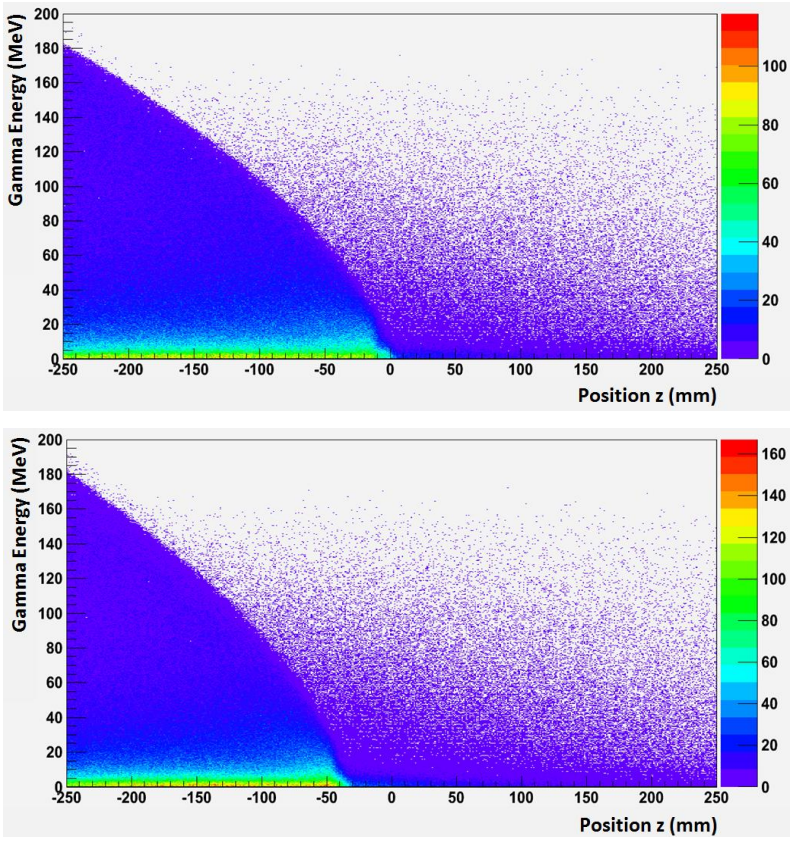

Figure 14: Neutron kinetic energy with respect to the position of origin in the cylinder phantom, along the z-axis. Top: water phantom. Bottom: PMMA phantom. The colour code represents the number of counts provided in the right-hand axis of each figure. $1x10^7$ events were executed. Data obtained with Geant4.

Figure 15 and Figure 16 show the gamma spectrum when gamma rays originate in the phantom in linear and logarithmic scale, respectively. Peaks are observed at 0.511, 2.22, 4.44, 5.21, and 6.13 MeV. The peak at 0.511 MeV is due to positron-electron annihilation gamma rays primarily from the decay of short-lived β^+-emitting isotope ^{15}O produced by nuclear fragmentation reactions between the primary protons and the target nuclei in the phantom.[10] The 2.22 MeV gamma rays are due to the absorption of secondary thermal neutrons by hydrogen; the $^1H(n,\gamma)^2H$ process. The 4.44 MeV gamma rays are from ^{12}C, due to proton interactions with both ^{16}O and ^{12}C, as presented in Table 5, Chapter 2. The 5.21 MeV emission line originates from ^{15}O. The first three excited states of ^{16}O are 6.13, 6.92 and 7.12 MeV, which can decay through the emission of gamma rays following the process $^{16}O(p,p')^{16}O^*$.[52] Of these three states, the 6.13 and 6.92 MeV emission lines are more evident in Figure 15 of our results. The energy spectrum of gamma ray emission during PT has been extensively studied[9,10,27,34,49,52,57], and the results obtained from this research agree well with these previous publications.

We find that in the water phantom the 4.44 MeV peak is greater in comparison to the 5.21 and 6.13 MeV peaks. This property is significant in the PMMA phantom, where the 5.21 and 6.13 MeV peaks are considerably low compared to the 4.44 MeV. This is because the PMMA material has composition including carbon, so more carbon nuclei are present to contribute to the emission of 4.44 MeV gamma rays. As expected, the gamma emission spectrum is characteristic to the material composition of the phantom from which they originate. This property has been a focus in previous work.[9,27]

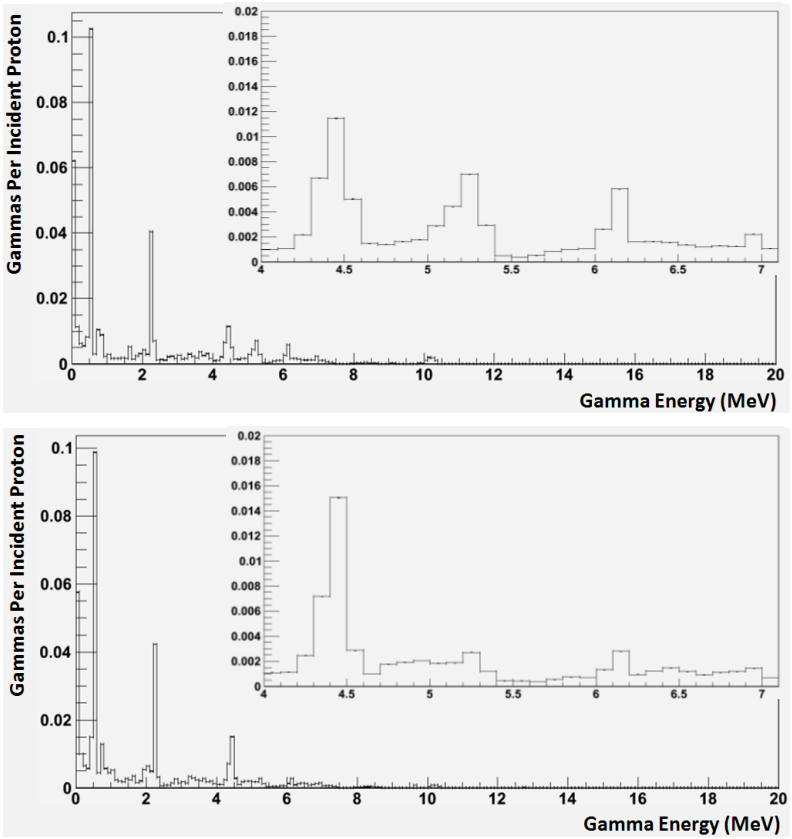

Figure 15: Energy spectrum of gamma when they originate in the cylinder phantom. Top: water phantom. Bottom: PMMA phantom. Data obtained with Geant4.

Figure 17 shows the energy spectrum of neutrons when they originate in the phantom. The spectrum shows a maximum at around 1-2 MeV before gradually decreasing at higher energies, having an average energy of around 6 MeV. This 1-2 MeV peak is due to proton inelastic collisions with hydrogen atoms, which are abundant in both water and PMMA materials.

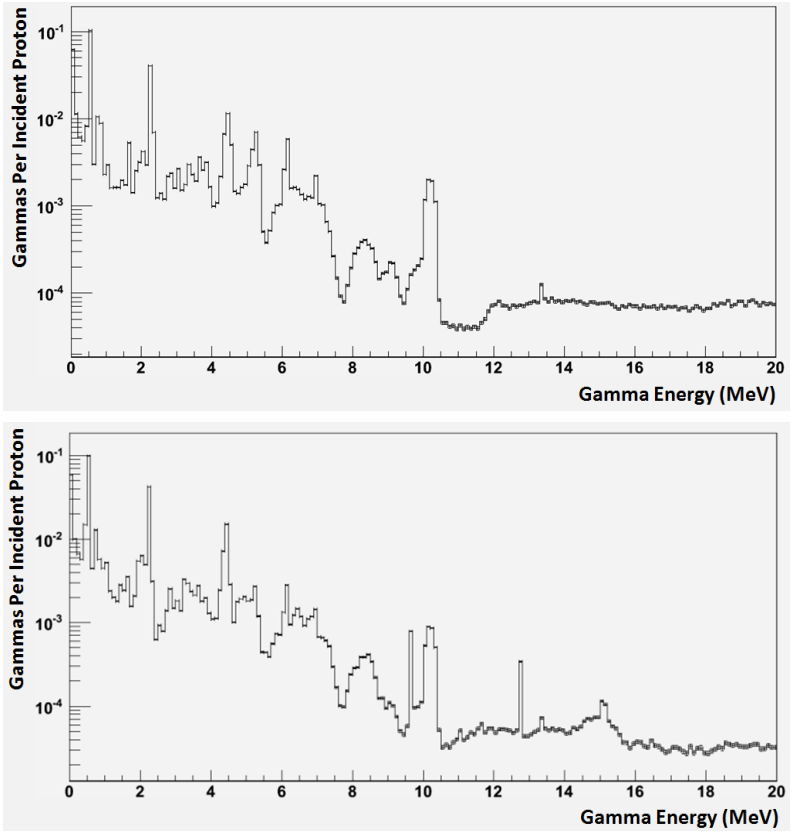

Figure 16: Energy spectrum of gamma when they originate in the cylinder phantom with logarithmic scale on the y-axis. Top: water phantom. Bottom: PMMA phantom. Data obtained with Geant4.

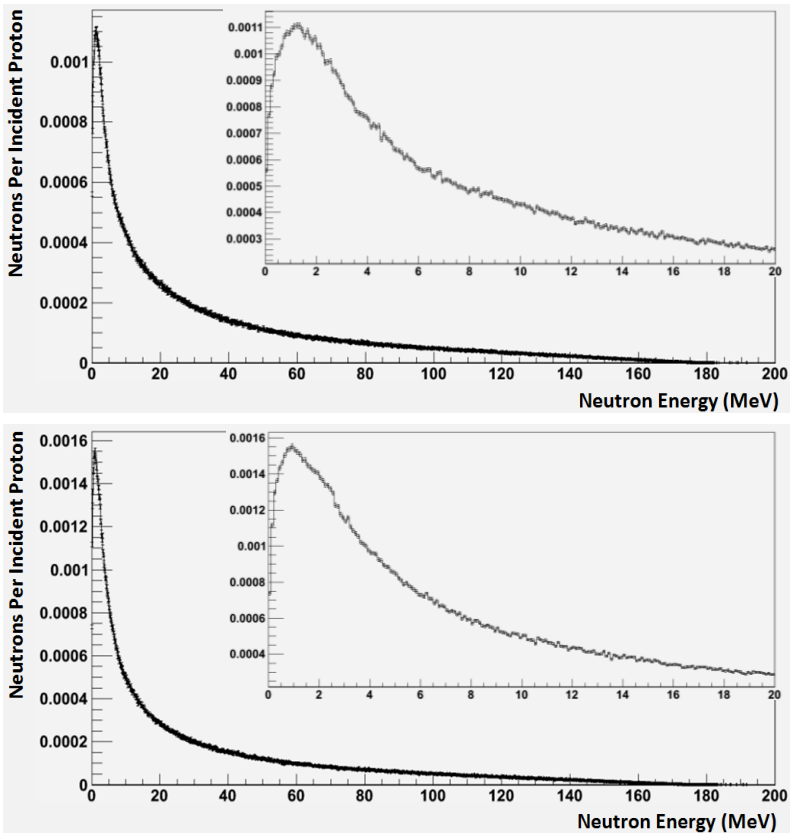

Figure 17: Energy spectrum of neutron when they originate in the cylinder phantom. Top: water phantom. Bottom: PMMA phantom. Data obtained with Geant4.

The results are presented for the cylinder phantom only, as the geometry of the phantom does not affect the energy spectra of PG and neutrons when they originate.

4.1.2 Correlation of Longitudinal Prompt Gamma Distribution with Bragg Peak Position

Figure 18 shows the point of origin of gamma rays and neutrons in the cylindrical water and PMMA phantoms. It can be observed that the majority of gamma and neutron emission originate in the path of the proton beam. Gamma ray production is more widespread than neutron production. This happens because neutrons are scattered at low energy and absorbed by the material while high energy neutrons are more forward peaked. It was found that the ratio of gamma and neutron production yield is approximately 2.

Figure 19 shows the emission of gamma rays and neutrons within the phantom as a function of position along the z-axis in order to study the correlation with the Bragg curve. The Bragg curve is normalised to the maximum value of the gamma emission (as is the case in all such correlation plots). This figure shows a greater number of gammas being emitted compared to neutrons in both the water and PMMA phantoms. More importantly, it shows the close correlation of the gamma emission and the Bragg curve; there is an increase in gamma emission just before the BP, and a sharp decrease in gamma emission at the BP, which reinforces the concept of using gammas as a beam range verification technique. The peak in gamma emission has been addressed as due to the cross section for proton reactions producing the gammas being maximum at a few tens of MeV.[10] In addition, the 'tail' following the BP can also be seen in the plots, which is primarily due to forward scattered secondaries such as gamma rays and neutrons. The close correlation of the gamma emission with the BP as validated in our results has also been shown by previous authors.[25,34,35,36]

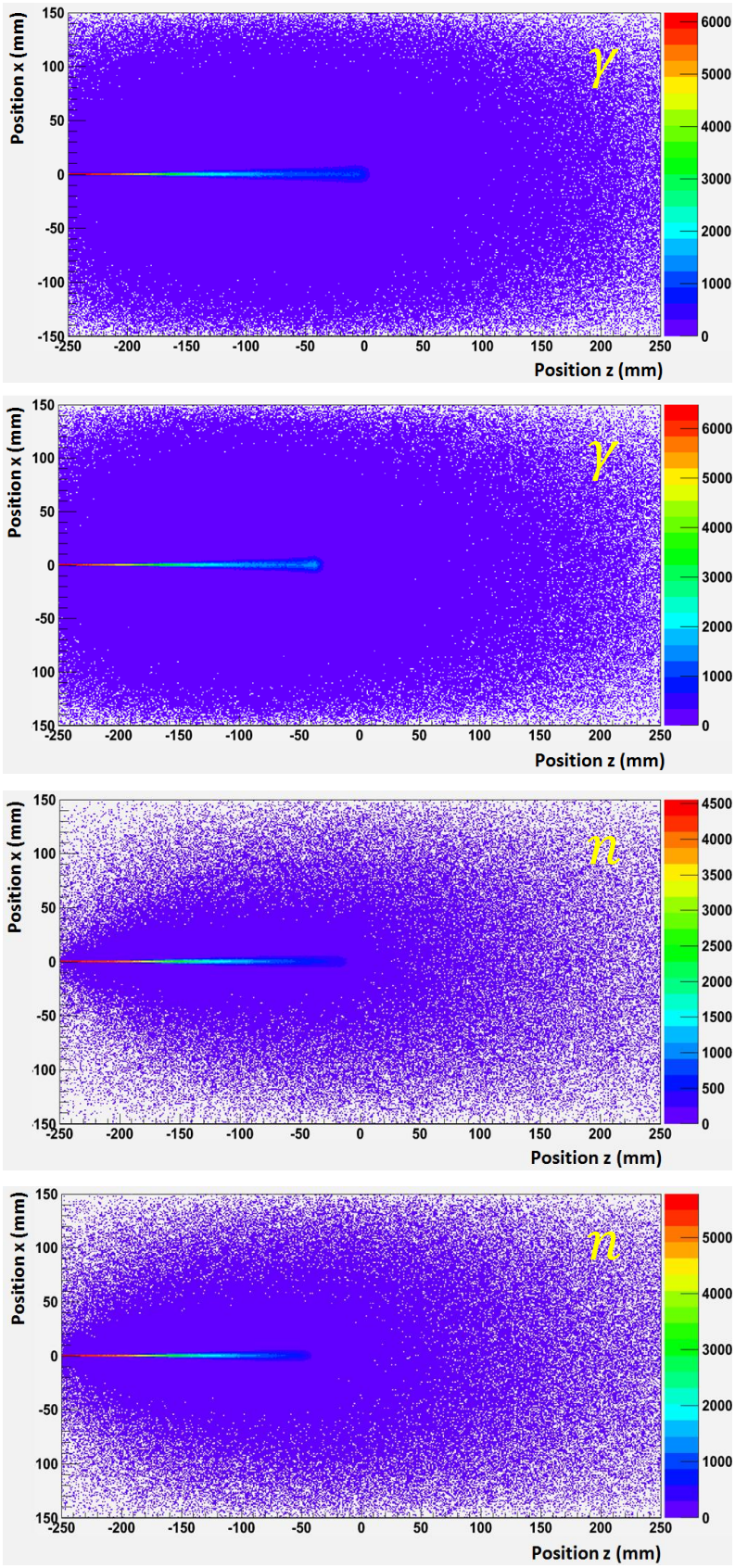

Figure 18: 2D spatial distribution of gammas (γ) and neutrons (n) that originate in the cylinder phantom. Top and third: water phantom. Second and bottom: PMMA phantom. The colour code represents the number of counts provided in the right-hand axis of each figure. $1x10^7$ events were executed. Data obtained with Geant4.

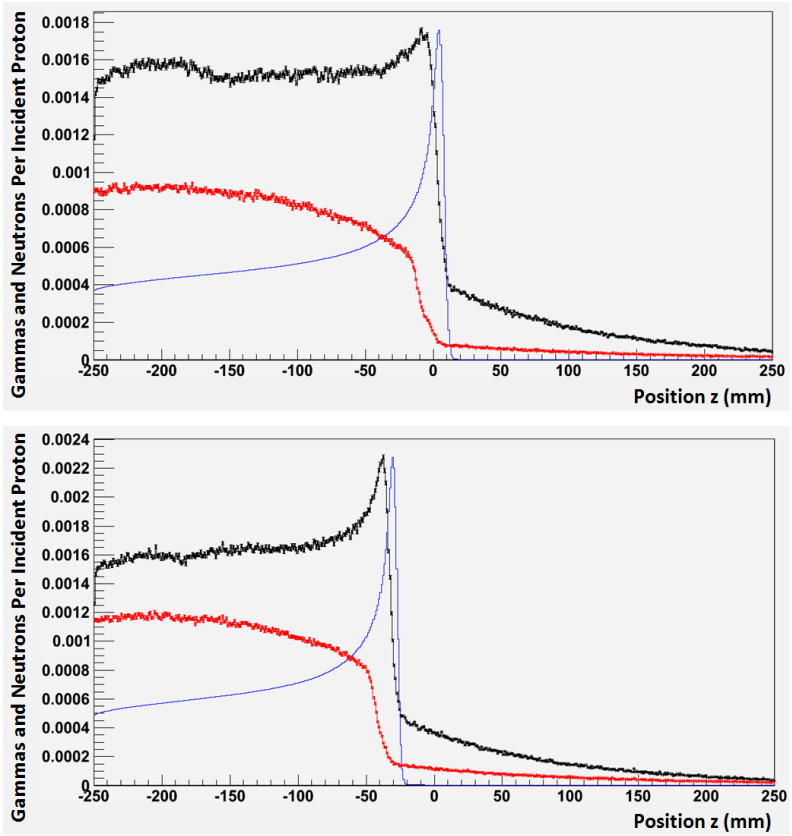

Figure 19: Gamma (black) and neutron (red) emission correlation with the Bragg curve (blue) in the cylinder phantom. The Bragg curve is normalised to the maximum value of gamma emission. Top: water phantom. Bottom: PMMA phantom. Data obtained with Geant4.

The gamma and neutron energy spectra within the BP were examined, so a *BP window* was set as 23-27 cm for the water phantom, and 20-24 cm for the PMMA phantom. We find that the energy spectra of gamma and neutron emission within the BP region have the same characteristic emission as seen in the entire phantom; 0.511, 2.22, 4.44, 5.21 and 6.13 MeV emission lines in the gamma emission spectrum, and the peaked distribution in the neutron emission spectrum at around 1-2 MeV. These are seen in Figure 20. Within the BP window, the PG emission lines in the gamma spectrum are seen to be more evident compared with the PG lines in the gamma spectrum of the entire phantom (see Figure 15), and comparable with the other gamma peaks. For example, the ratio of the 2.22 and 4.44 MeV emission lines within the entire phantom is ~3.6, while within the BP region the ratio is ~1.8. This reinforces that the emission of PG rays are greatest at the end of the proton range (the BP region).

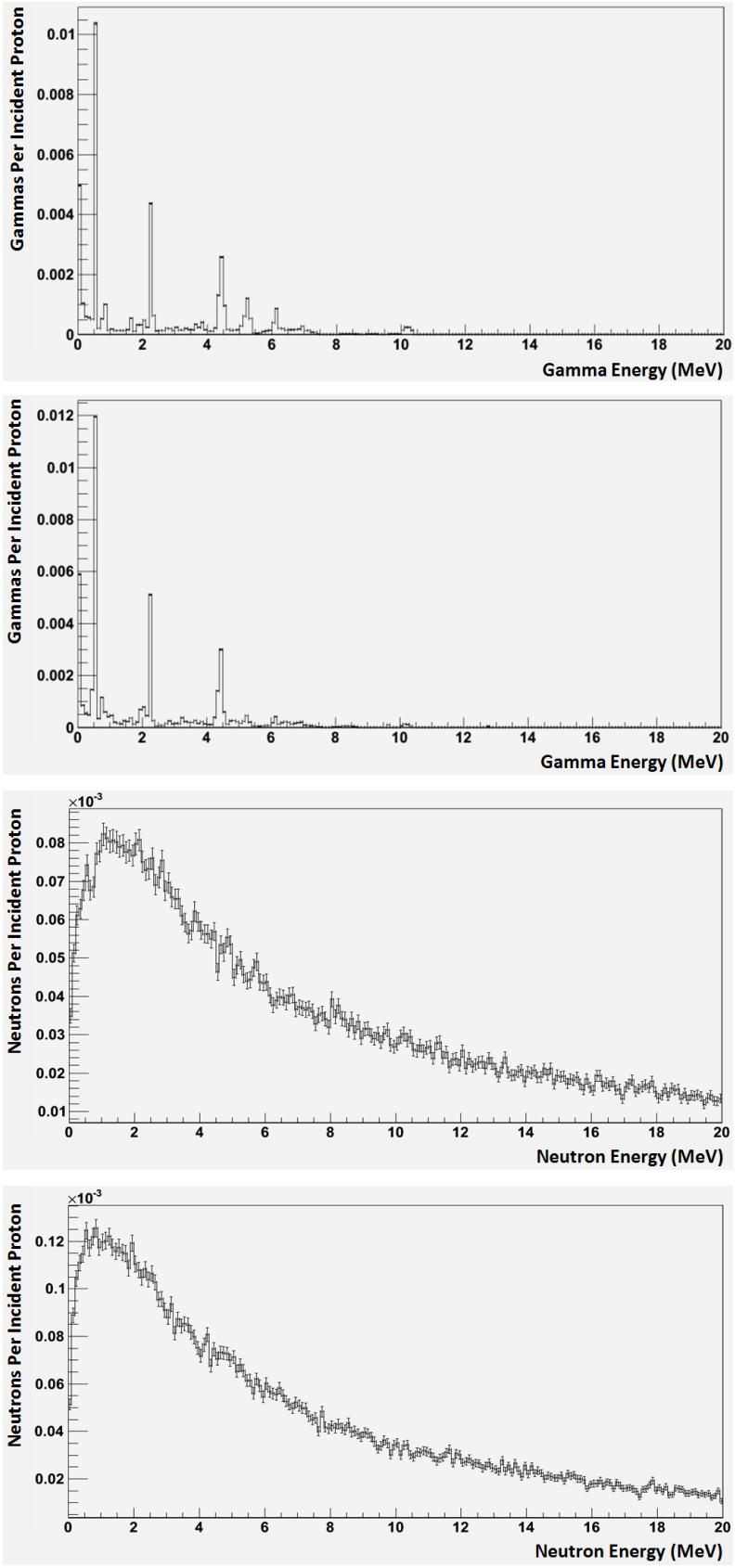

Figure 20: Gamma and neutron energy spectra under the BP window in the cylinder phantom. Top and third: water phantom (BP window: 23-27 cm). Second and bottom: PMMA phantom (BP window: 20-24 cm). Data obtained with Geant4.

To study the correlation between the PG signal and the BP, energy windows were applied to each PG energy with a 0.4 MeV width: 4.2-4.6, 5.0-5.4, and 5.9-6.3 MeV. A 4.2-6.3 MeV window is also studied as it contains all three PG energies, and so it increases the number of gamma statistics. Figure 21 and Figure 22 show the PG distribution with respect to the position along the phantom, where the correlation with the Bragg curve can be observed. In the water phantom, we identify that the 4.44 MeV PG window yields the closest correlation to the Bragg curve compared to the other energies; the sharp fall-off in PG emission closely correlates to the fall-off in dose. Hence, it can be seen that the correlation between the PG emission and dose distribution can allow range verification in PT by using the PG signal. The 3-5 MeV energy range of gammas has been shown to yield the greatest correlation with the beam range in another study as well.[57] A set minimum gamma energy of 4 MeV was also shown to yield the deepest fall-off when relative dose was plotted as a function of depth.[25] Other studies have also looked into the PG energies for distribution correlating to the BP.[69,70] Hence, high energy gamma rays (mainly from nuclear reactions) provide information regarding the position of the BP, while low energy gamma rays (mainly from scattering) contribute to the background, as mentioned in the literature.[10] Although the 6.13 MeV window also presents a close correlation with the BP fall-off, there appears a relatively large gamma signal in the build-up of the BP and after the peak (gamma tail). The 5.21 MeV PG signal fall-off occurs just before the BP, more so than the other energies. The 4.2-6.3 MeV window also exhibits good correlation with the BP, while providing a greater number of gamma statistics. Similarly, in the PMMA phantom, both the 4.2-4.6 and 4.2-6.3 MeV gamma windows yield good correlations with the BP, and with an increased gamma tail signal due to a greater number of scattered gammas and neutrons.

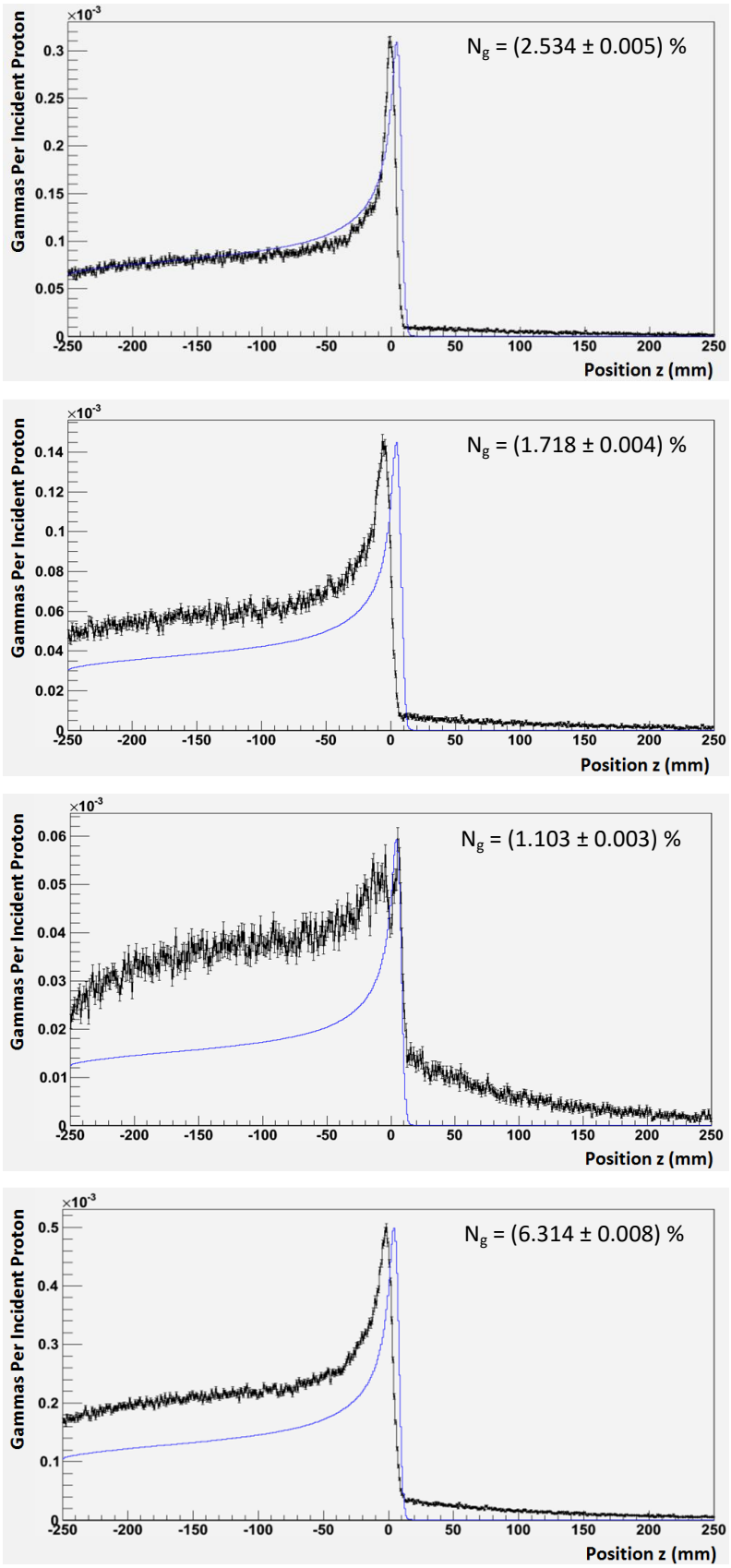

Figure 21: Gamma (black) emission correlation with the Bragg curve (blue) in the cylindrical water phantom. The Bragg curve is normalised to the maximum value of gamma emission. Top: 4.2-4.6 MeV window. Second: 5.0-5.4 MeV window. Third: 5.9-6.3 MeV window. Bottom: 4.2-6.3 MeV window. Data obtained with Geant4.

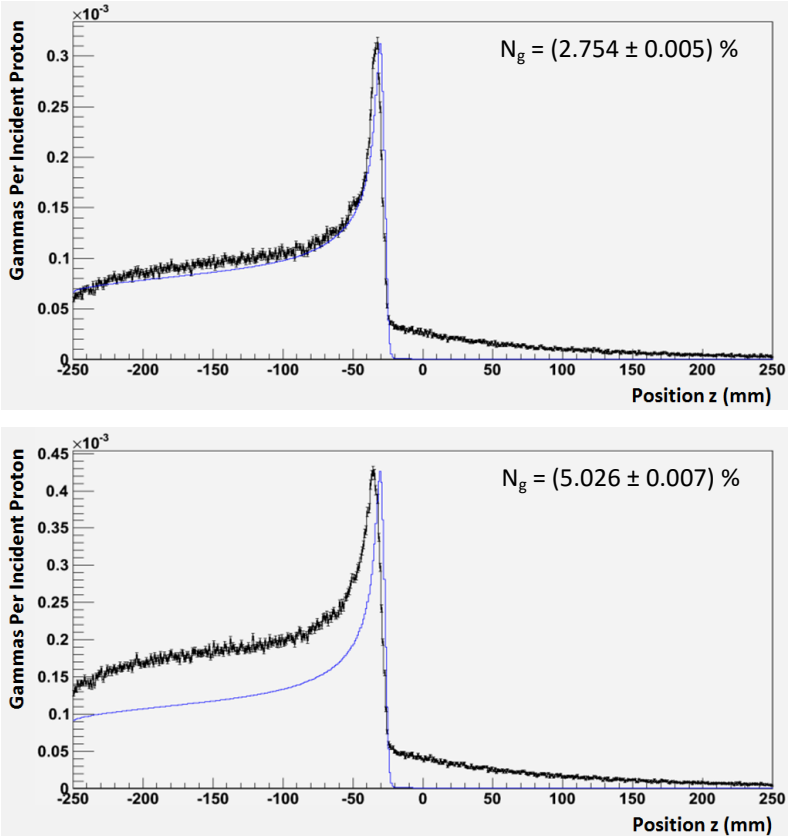

Figure 22: Gamma (black) emission correlation with the Bragg curve (blue) in the cylindrical PMMA phantom. The Bragg curve normalised to maximum value of gamma emission. Top: 4.2-4.6 MeV window. Bottom: 4.2-6.3 MeV window. Data obtained with Geant4.

It can be noticed from the correlation plots that the PG emission fall-off is not exactly correlated to the BP fall-off, as already mentioned. However, we find that this correlation becomes improved when the gamma energy windows are applied. Table 6 compares the peak and 50% distal fall-off positions of the PG emission and the BP. In the water phantom, we see that the 5.9-6.3 MeV PG rays exhibit the closest peak and fall-off correlation with the BP. However, this energy window presents a relatively low gamma yield. The 4.2-4.6 and 4.2-6.3 MeV energy windows present not only excellent PG fall-off correlation with the BP fall-off, they also offer higher gamma yields. The PG fall-off position within the PMMA phantom shows better BP fall-off correlation compared to the water results. Both 4.2-4.6 and 4.2-6.3 MeV energy windows provide excellent BP correlation, while the 4.2-6.3 MeV window offers the higher gamma yield, as expected. The 4.2-4.6 MeV window presents a ~4 mm fall-off difference in water and ~1 mm fall-off difference in PMMA. The fall-off difference in the 4.2-6.3 MeV window are ~4 mm in water and ~2 mm in PMMA. Due to the bin width of the histograms, the uncertainty of these position values is 1 mm. A recent study also showed that the 4.44 MeV and 6.13 MeV discrete gamma profiles exhibit a peak near the end of the proton

range, consistent with the cross sections of the nuclear transitions.[70] We therefore find that there is a difference in the PG emission fall-off position with varying energy, and the 4.44 MeV PG offers the greatest correlation with the beam range.

The signal-to-noise ratio (gamma-to-neutron ratio) has been retrieved for many of our results, to quantitatively compare the emission of gammas and neutrons. N_g represents the number of gammas per incident proton, while N_n represents the number of neutrons per incident proton. We find that about 3% of gammas per incident proton in the energy range of 4.2-4.6 MeV are produced in water and PMMA, respectively. While in the energy range of 4.2-6.3 MeV, about 6% and 5% of gammas per incident proton are produced in water and PMMA, respectively. So there are more gammas being registered in the larger energy window of 4.2-6.3 MeV, hence this window yields the higher gamma-neutron ratio, with $N_g/N_n \cong 0.30$ in water, and $N_g/N_n \cong 0.21$ in PMMA (see Table 7). Thus in a clinical sense, a trade-off must perhaps be made between choosing a window that offers the better PG and BP correlation or choosing a window that achieves a higher signal-to-noise ratio and provides a greater number of gammas to be detected (for improved image quality).

Table 7 summarises not only the gamma-neutron ratios within the energy windows found in this section, it also presents a summary of all gamma and neutron yields found from our study thus far. The findings in this table have been discussed along with the corresponding figures already presented.

Table 6: Comparison of PG peak position and BP position, and 50% fall-off positions.

	Energy window (MeV)	Peak position (mm) (±1 mm)			Fall-off position (mm) (±1 mm)		
		PG	BP	Difference	PG	BP	Difference
Water	No window	242		12	254		4
	4.2-4.6	249		5	254		4
	5.0-5.4	246	254	8	251	258	7
	5.9-6.3	254		0	258		0
	4.2-6.3	249		5	254		4
PMMA	No window	212		7	219		4
	4.2-4.6	217	219	2	222	223	1
	4.2-6.3	215		4	221		2

Table 7: Summary of gamma and neutron yields (in percentage) in the cylinder phantom. The ratio N_g/N_n within the energy windows is taken as the gamma yield within the energy window to the total neutron yield within the phantom. The simulation statistical uncertainties are given.

	Within	Number of gammas per incident proton, N_g (%)	Number of neutrons per incident proton, N_n (%)	Ratio, N_g/N_n
Water	Phantom	43.503 ± 0.021	21.029 ± 0.015	2.0687 ± 0.0018
	BP window (23-27 cm)	4.578 ± 0.007	0.894 ± 0.003	5.1208 ± 0.0189
	Energy window (MeV)			
	4.2-4.6	2.534 ± 0.005		0.1205 ± 0.0003
	5.0-5.4	1.718 ± 0.004		0.0817 ± 0.0002
	5.9-6.3	1.103 ± 0.003		0.0525 ± 0.0001
	4.2-6.3	6.314 ± 0.008		0.3003 ± 0.0004
PMMA	Phantom	41.443 ± 0.020	24.368 ± 0.016	1.7007 ± 0.0014
	BP window (20-24 cm)	4.822 ± 0.007	1.147 ± 0.003	4.2040 ± 0.0126
	Energy window (MeV)			
	4.2-4.6	2.754 ± 0.005		0.1130 ± 0.0002
	5.0-5.4	0.761 ± 0.003		0.0312 ± 0.0001
	5.9-6.3	0.580 ± 0.002		0.0238 ± 0.0001
	4.2-6.3	5.026 ± 0.007		0.2063 ± 0.0003

The cube geometry phantom results were again found to be consistent with the cylinder phantom results. Comparing the gamma-neutron ratios in the cylinder and cube phantoms, we find that the corresponding values are either very similar or exactly the same (see Table 8 for cube phantom gamma-neutron ratios). This suggests that regardless of the geometry, the ratio of gammas to neutrons emitted within the (same) material remains consistent. On the other hand, the emission of gamma and neutron leaving the phantom is influenced by the phantom geometry, so both cylinder and cube geometry phantom results will be presented and discussed in the following section.

Table 8: Cube phantom gamma-neutron ratios. The simulation statistical uncertainties are given.

	Energy window (MeV)	Number of gammas per incident proton, N_g (%)	Number of neutrons per incident proton, N_n (%)	Ratio, N_g/N_n
Water	No window	41.445 ± 0.020	20.423 ± 0.014	2.0293 ± 0.0017
	4.2-4.6	2.468 ± 0.005		0.1208 ± 0.0003
	5.0-5.4	1.677 ± 0.004		0.0821 ± 0.0002
	5.9-6.3	1.034 ± 0.003		0.0506 ± 0.0002
	4.2-6.3	6.112 ± 0.008		0.2993 ± 0.0004
PMMA	No window	39.966 ± 0.020	23.619 ± 0.015	1.6921 ± 0.0014
	4.2-4.6	2.656 ± 0.005		0.1125 ± 0.0002
	4.2-6.3	4.867 ± 0.007		0.2061 ± 0.0003

From our results, we find that not only is the 4.44 MeV PG emission line more prominent than the 5.21 and 6.13 MeV PG peaks in both materials, it also offers good correlation with the BP for beam range monitoring. Hence, we determine that the optimal energy for PG imaging is around 4.44 MeV. Yet the gamma rays within the 4.2-6.3 MeV window provide good BP correlation with the benefit of increased gamma statistics. However, as we have mentioned, a challenge that remains for PG imaging is the lack of a novel imaging detector for high energy PG detection. So although we have determined an optimal energy window for PG imaging, we further investigate detection characteristics of PG emission with the use of a sensitive detection sphere and cylinder to aid in future PG imaging system design and development. An optimal angular and time window will be determined for improved PG imaging formation, with background suppression for better image quality.

4.2 Characterisation of the Prompt Gamma Emission Field

4.2.1 Angular Dependence of Prompt Gamma Detection

4.2.1.1 Emission Characteristics of Prompt Gamma with the Detection Sphere

Following our simulations to determine the characteristic PG rays and neutrons produced in the water and PMMA phantoms, we then pursued to investigate those secondaries which escaped the phantom. This was essential information for the study, development and positioning of an imaging system for use in PT. In order to do this, we included a detection sphere surrounding the phantom with radius 50 cm, such that the angular distribution of the PG rays and neutrons traversing the surface of the sphere were investigated.

Both cylindrical and cubic phantoms were studied as the PG emission depends on the shape of the phantom itself as the PG radiation interacts with the material of the phantom and the probability of interaction and absorption depends on the traversed path in the medium.

Figure 23 shows the angular distribution of gammas and neutrons emitted from cylindrical water and PMMA phantoms. The plots show that the azimuthal emission (θ) is isotropic, whereas the axial emission (φ), along the direction of incidence of the proton beam, is non-isotropic, as expected.

Most gamma emission is directed at $\varphi \sim 110^{o}$ in both the cases of a water and PMMA phantom, while most neutron emission in water is directed at $\varphi \sim 60^{o}$, and in PMMA is $\varphi \sim 70^{o}$, with respect to the centre of the coordinate system. Hence, gamma emission is seen to be slightly backward peaked while the neutron emission is forward peaked, agreeing with previous work.[71] Here, the BP position in the cylinder water phantom occurs at around the centre of the phantom, which is the point of the simulation coordinate system centre. In the cylinder PMMA phantom, the BP position is about 3 cm before the coordinate system centre. Therefore, from our results we determine that gamma has an emission preference at $\sim 20^{o}$ backward peaked in water, and $\sim 17^{o}$ backward peaked in PMMA, relative to the BP. Figure 24 shows the angular distribution of gamma rays and neutrons.

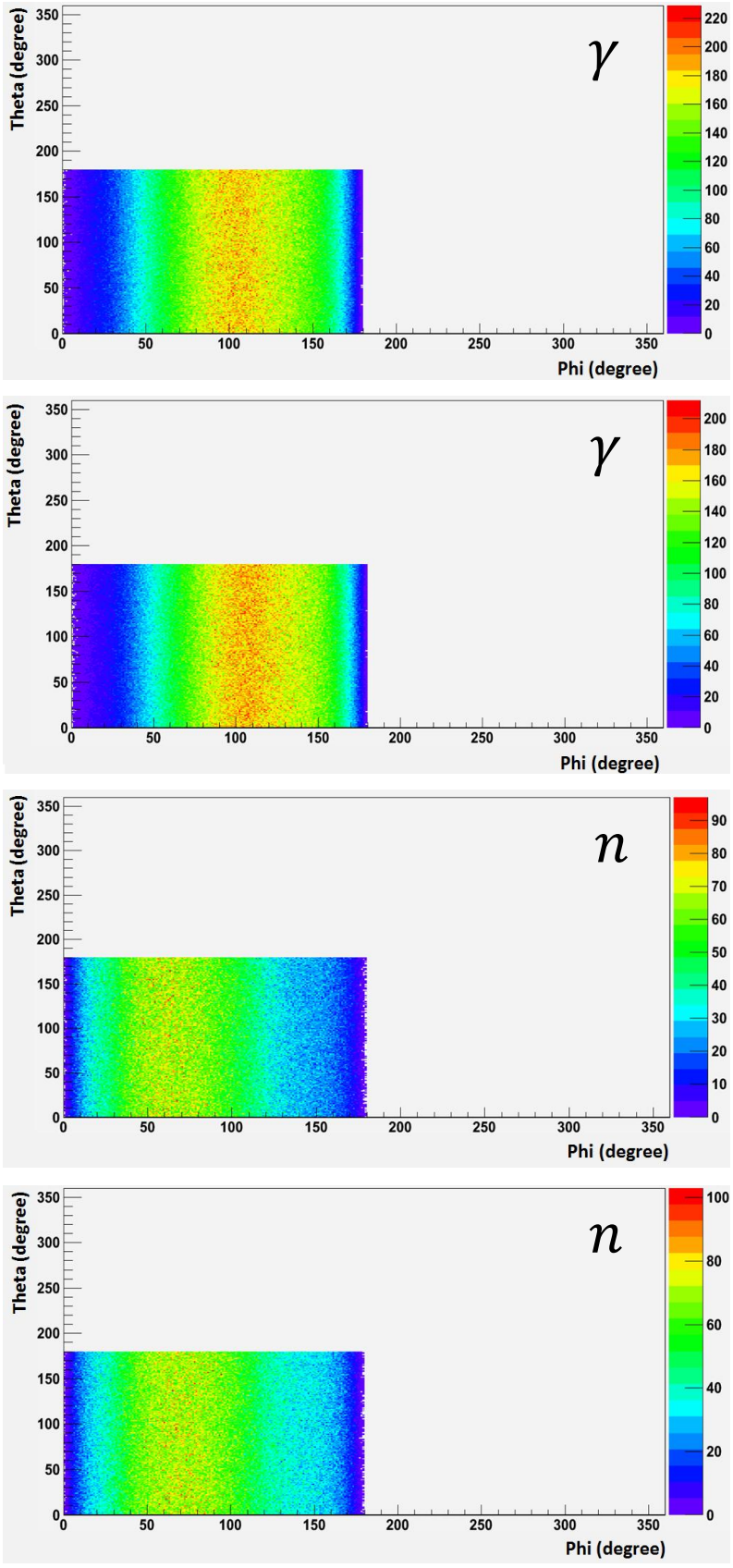

Figure 23: Angular distribution ($\boldsymbol{\theta}$ and $\boldsymbol{\varphi}$, see Figure 9, Chapter 3) of gamma rays ($\boldsymbol{\gamma}$) and neutrons ($\boldsymbol{n}$) when traversing the detection sphere. The radiation is emitted from a cylinder phantom of water (top and third) and PMMA (second and bottom). The colour code represents the number of counts provided in the right-hand axis of each figure. 1x10^7 events were executed. Data obtained with Geant4.

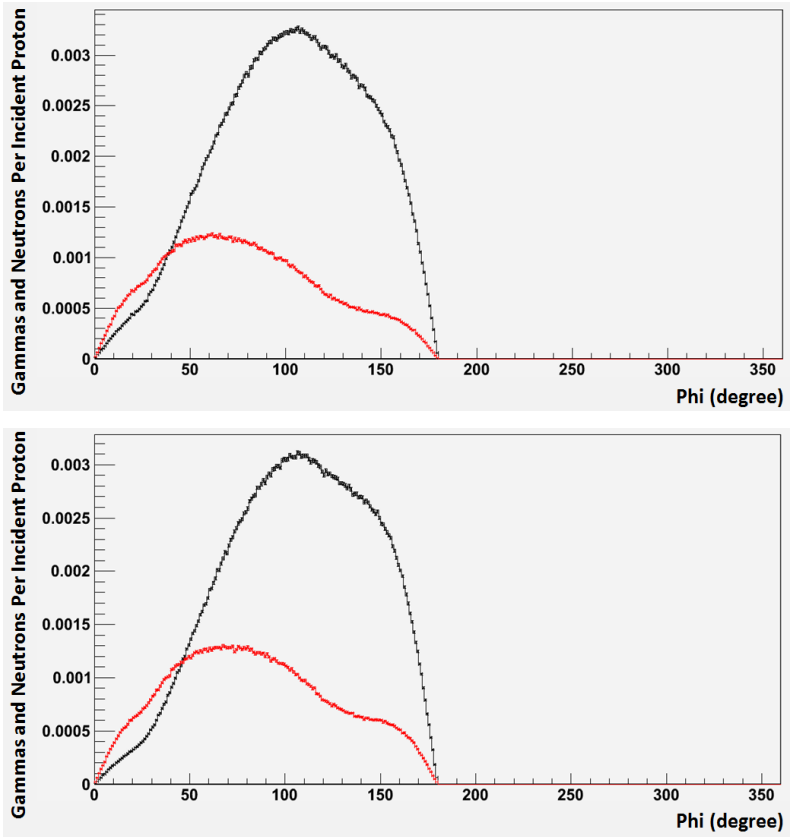

Figure 24: Angular distribution of gamma rays (black) and neutrons (red) traversing the detection sphere, once emitted from the cylinder phantom. Top: water phantom. Bottom: PMMA phantom. Data obtained with Geant4.

Although we have determined that the 4.44 MeV PG energy is the optimal choice for BP monitoring due to its relatively high yield and close correlation with the proton range, we continue to explore the various energy windows with respect to angular emission. Figure 25 and Figure 26 present the angular frequency plots comparing gamma emission within the energy windows to the total neutron emission from the cylinder water and PMMA phantoms, respectively. The gamma-neutron ratios are also presented. The gamma angular preference of $\varphi \sim 110^{o}$ with respect to the centre of the coordinate system still remains true here, within the applied PG energy windows. In both phantoms, the 4.2-6.3 MeV window yields the highest signal-to-noise ratio due to the greater gamma statistics, as expected. Comparing the two phantom materials, we find that water yields higher signal-to-noise ratios for the corresponding energy windows, since water produces a relatively higher number of gammas with lower number of neutrons.

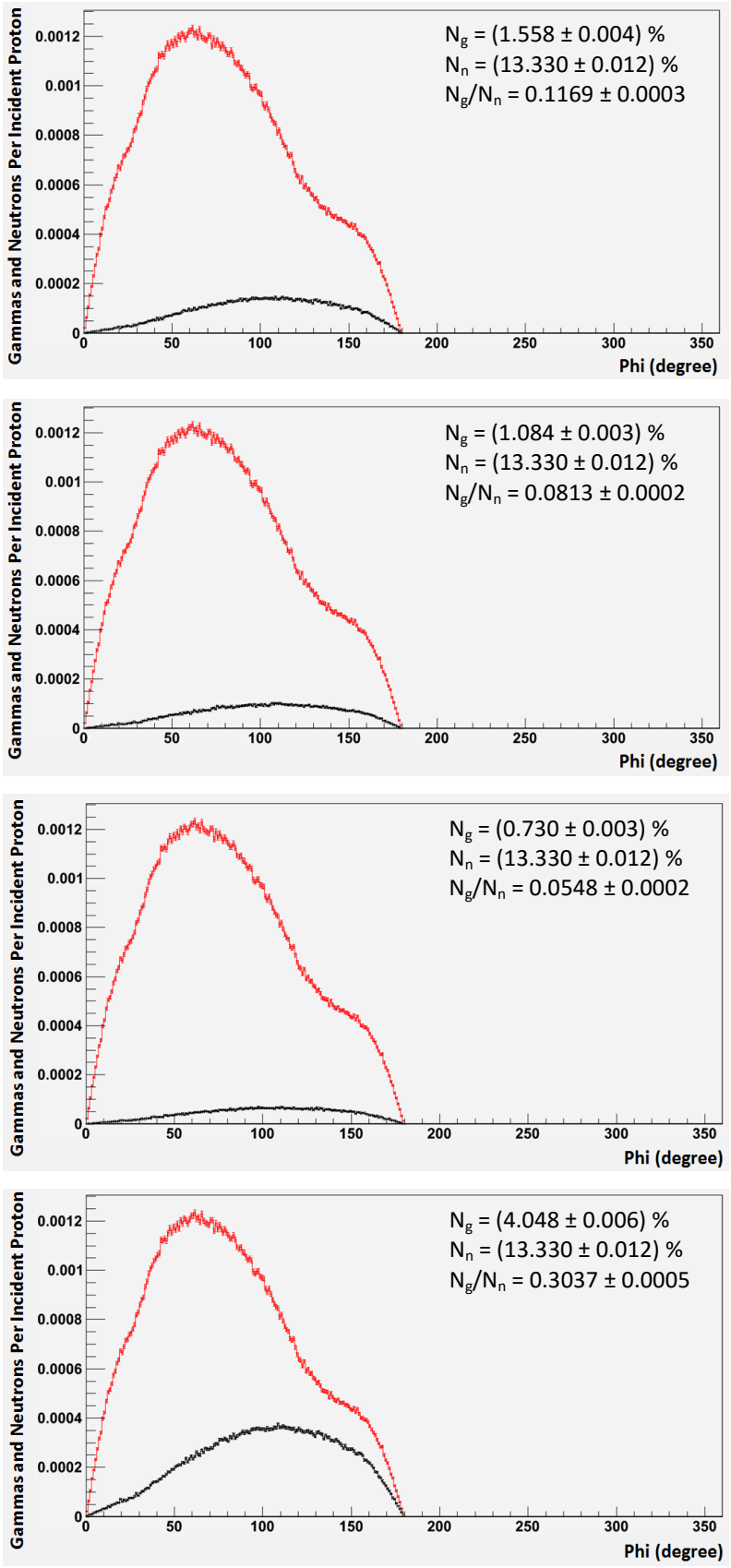

Figure 25: Angular distribution of gamma rays (black) and neutrons (red) traversing the detection sphere, once emitted from the cylinder water phantom. Top: 4.2-4.6 MeV window. Second: 5.0-5.4 MeV window. Third: 5.9-6.3 MeV window. Bottom: 4.2-6.3 MeV window. Data obtained with Geant4.

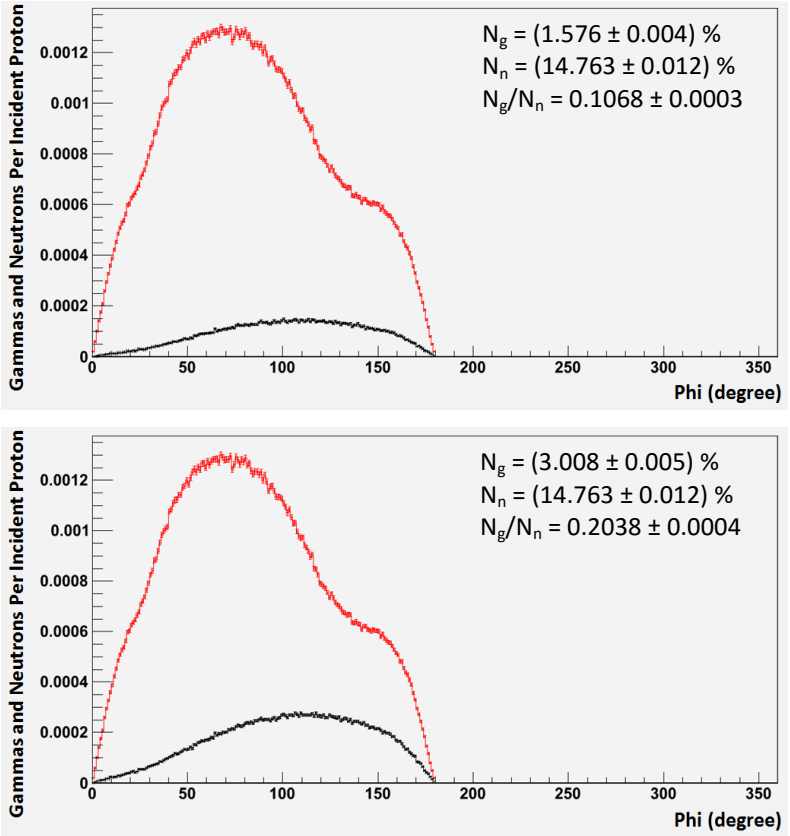

Figure 26: Angular distribution of gamma rays (black) and neutrons (red) traversing the detection sphere, once emitted from the cylinder PMMA phantom. Top: 4.2-4.6 MeV window. Bottom: 4.2-6.3 MeV window. Data obtained with Geant4.

Table 9: Angular preference of gamma and neutron emission traversing the detection sphere once emitted from the cylinder phantom.

	Energy window (MeV)	Angular preference, φ, with respect to centre of coordinate system (degree) (±5°)		Gamma angular preference, φ, with respect to the BP position (degree) (±5°)
		Gamma	Neutron	
Water	No window	107	60	20
	4.2-4.6	108		
	5.0-5.4	110		
	5.9-6.3	110		
	4.2-6.3	110		
PMMA	No window	107	70	17
	4.2-4.6	110		
	4.2-6.3	110		

Table 10: Summary of gamma and neutron yields (in percentage) traversing the detection sphere once emitted from the cylinder phantom. The simulation statistical uncertainties are given.

	Energy window (MeV)	Number of gammas per incident proton, N_g (%)	Number of neutrons per incident proton, N_n (%)	Ratio, N_g/N_n
Water	No window	35.096 ± 0.019	13.330 ± 0.012	2.6329 ± 0.0028
	4.2-4.6	1.558 ± 0.004		0.1169 ± 0.0003
	5.0-5.4	1.084 ± 0.003		0.0813 ± 0.0002
	5.9-6.3	0.730 ± 0.003		0.0548 ± 0.0002
	4.2-6.3	4.048 ± 0.006		0.3037 ± 0.0005
PMMA	No window	33.113 ± 0.018	14.763 ± 0.012	2.2430 ± 0.0022
	4.2-4.6	1.576 ± 0.004		0.1068 ± 0.0003
	4.2-6.3	3.008 ± 0.005		0.2038 ± 0.0004

Table 9 presents the angular preference of gamma rays and neutrons traversing the detection sphere from the cylinder phantoms. Table 10 summarises the yields and ratios of gamma rays and neutrons traversing the detection sphere from the cylinder phantoms. Comparing this table with the yield values of gamma rays and neutrons that originate within the phantom (see Table 7), we find that the number of gamma rays (and neutrons) per incident proton has decreased, as expected. In the energy range of 4.2-4.6 MeV, about 1.6% of gammas per incident proton reach the detection sphere from the phantoms, while about 2.5% originate within the water phantom, and about 2.8% in the PMMA phantom. In the 4.2-6.3 MeV range, about 4% and 3% of gammas per incident proton reach the detection sphere from the water and PMMA cylinder phantoms where 6% and 5% originate within the phantoms, respectively. The 4.2-6.3 MeV window again exhibits the greater gamma-neutron ratio.

Figure 27 shows the angular distribution of gamma rays and neutrons traversing the detection sphere from the cubic phantom. The axial emission (θ) of gammas and neutrons from the phantoms is non-isotropic, as expected. The gamma angular preference is seen to be $\varphi \sim 90^{o}$, while the neutron emission preference is $\varphi \sim 30^{o}$, in both water and PMMA, with respect to the centre of the coordinate system. However, we find that the azimuthal emission (θ) for gammas and neutrons is also non-isotropic, which is different to the cylinder phantom results. This is simply due to the geometry of the phantom; most gamma emission occurs at $\theta \sim 0$, 90, and 180 degrees, while least gamma emission occurs at $\theta \sim 45$ and 135 degrees, due to the absorption path of the gammas (and neutrons) before escaping the phantom.

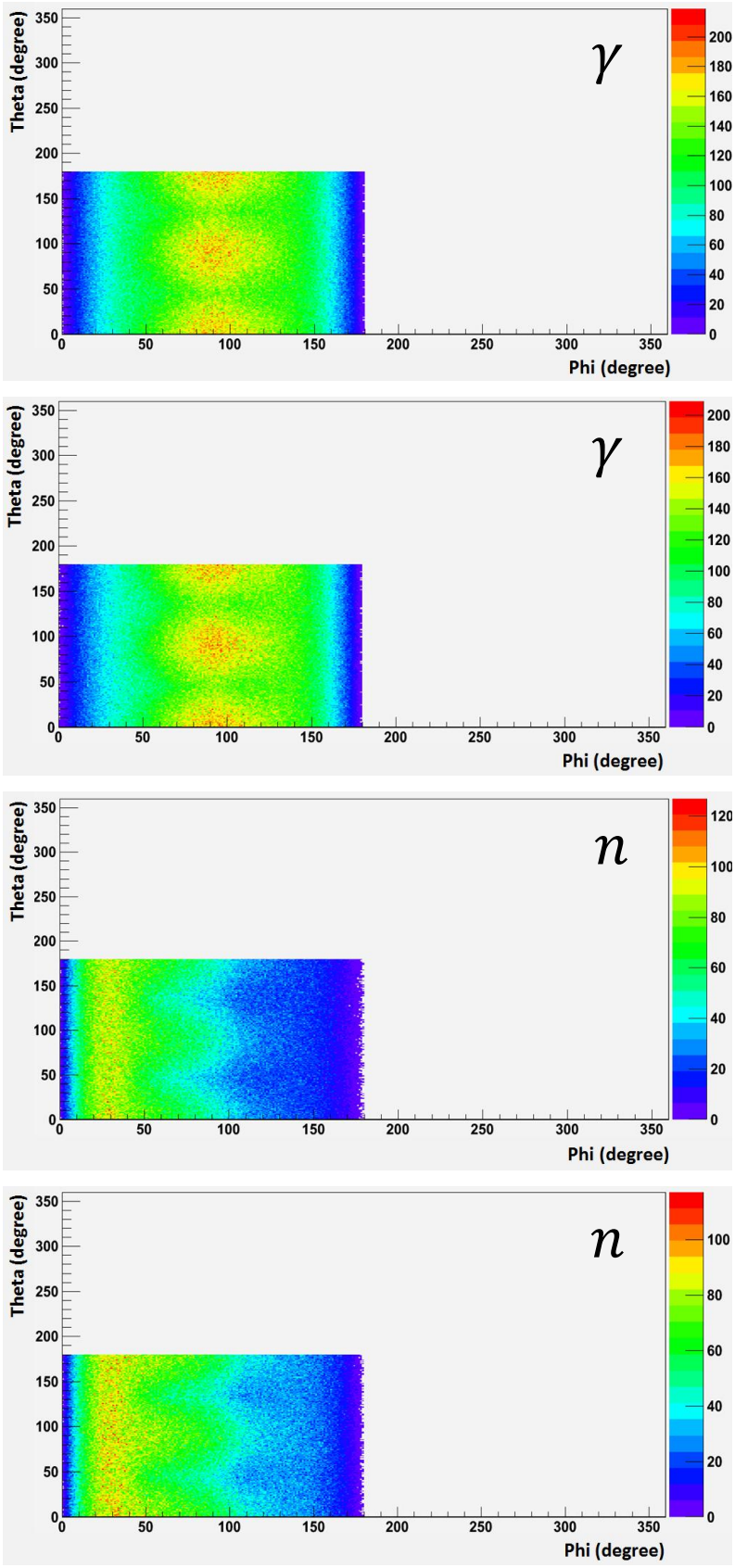

Figure 27: Angular distribution ($\boldsymbol{\theta}$ and $\boldsymbol{\varphi}$, see Figure 9, Chapter 3) of gamma rays ($\boldsymbol{\gamma}$) and neutrons ($\boldsymbol{n}$) when traversing the detection sphere. The radiation is emitted from a cube phantom of water (top and third) and PMMA (second and bottom). The colour code represents the number of counts provided in the right-hand axis of each figure. 1x10^7 events were executed. Data obtained with Geant4.

The angular preference of gamma rays and neutrons from the cube water and PMMA phantoms can be seen in the plots of Figure 28, where gamma has an emission preference at $\varphi \sim 90^{o}$ and neutrons have an emission preference at $\varphi \sim 30^{o}$ with respect to the centre of the coordinate system. Here, the BP position occurs several centimetres following the simulation coordinate system centre (~10 cm for the water phantom, ~7 cm for the PMMA phantom). Hence, gamma emission is again seen to be slightly backward peaked, while neutrons are forward peaked. Here, we determine that gamma has an emission preference at $\sim 11^{o}$ backward peaked in water, and $\sim 8^{o}$ backward peaked in PMMA, relative to the BP. We find that our results show a difference in BP emission angle between the cylinder and the cube phantoms; however no difference in gamma angular preference should be expected with respect to the BP. This difference is seen in our results simply because of the difference in peak position with respect to the coordinate system centre, regardless of the point in which the angular calculation is taken.

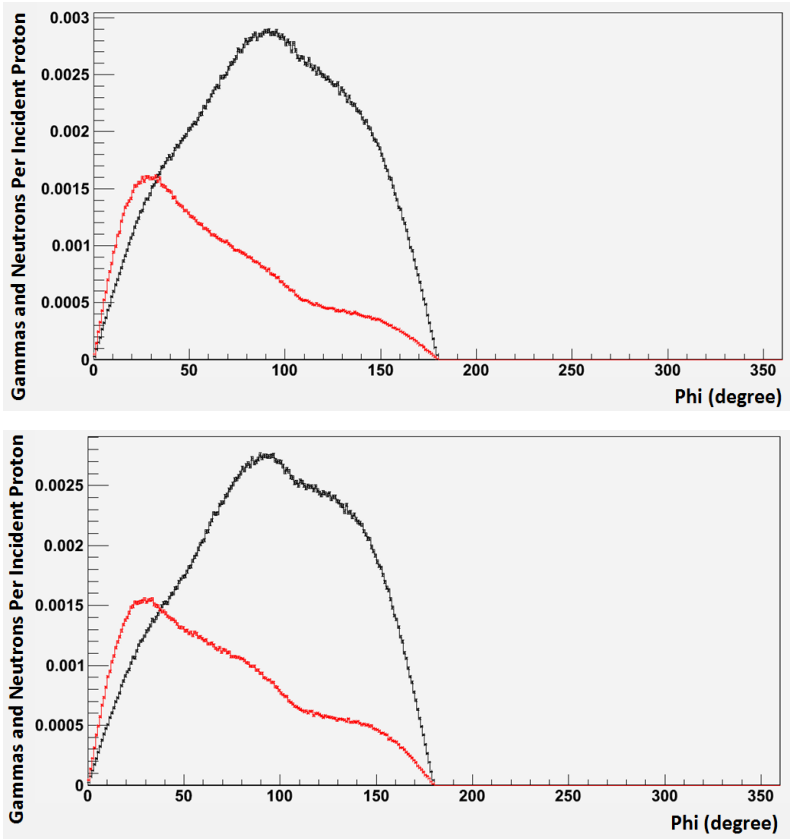

Figure 28: Angular distribution of gamma rays (black) and neutrons (red) traversing the detection sphere, once emitted from the cube phantom. Top: water phantom. Bottom: PMMA phantom. Data obtained with Geant4.

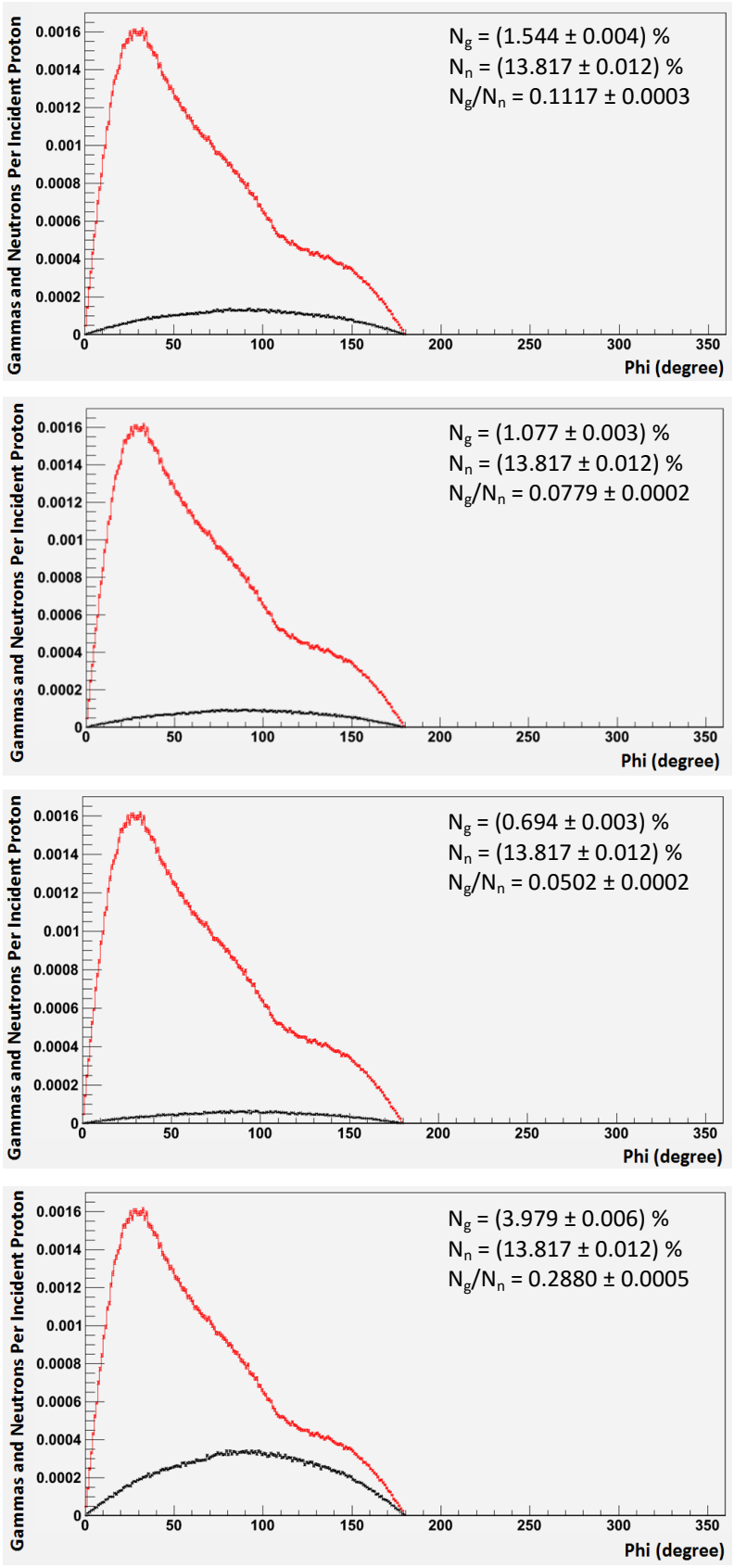

Figure 29: Angular distribution of gamma rays (black) and neutrons (red) traversing the detection sphere, once emitted from the cube water phantom. Top: 4.2-4.6 MeV window. Second: 5.0-5.4 MeV window. Third: 5.9-6.3 MeV window. Bottom: 4.2-6.3 MeV window. Data obtained with Geant4.

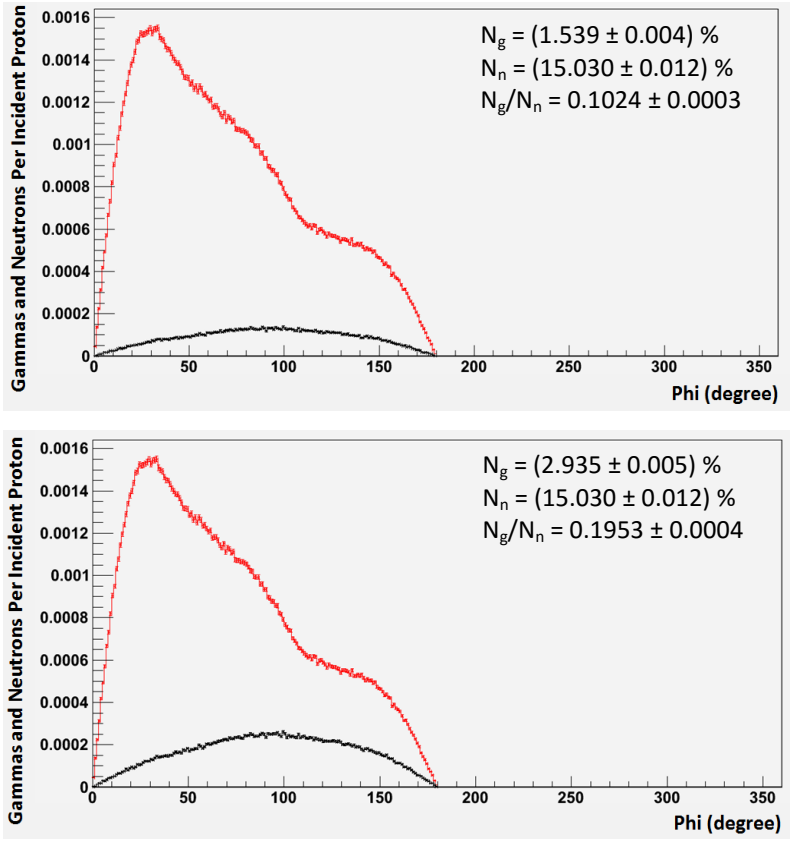

Figure 30: Angular distribution of gamma rays (black) and neutrons (red) traversing the detection sphere, once emitted from the cube PMMA phantom. Top: 4.2-4.6 MeV window. Bottom: 4.2-6.3 MeV window. Data obtained with Geant4.

Figure 29 and Figure 30 present the angular distribution of gamma emission within the energy windows of interest and the total neutron emission from the cubic water and PMMA phantoms, respectively. The gamma-neutron ratios are also presented. The gamma angular preference within the PG energy windows is $\varphi \sim 90^{o}$ with respect to the centre of the coordinate system. Similar to the cylinder phantom results, water yields the higher signal-to-noise ratios for the corresponding energy windows, and the 4.2-6.3 MeV window yields the highest gamma-neutron ratio. Table 11 presents the angular preference of gamma rays and neutrons traversing the detection sphere once emitted from the cubic phantom.

Table 11: Angular preference of gamma and neutron emission traversing the detection sphere once emitted from the cube phantom.

	Energy window (MeV)	Angular preference, φ, with respect to centre of coordinate system (degree) (±5°)		Gamma angular preference, φ, with respect to the BP position (degree) (±5°)
		Gamma	Neutron	
Water	No window	90	30	11
	4.2-4.6	90		
	5.0-5.4	90		
	5.9-6.3	90		
	4.2-6.3	90		
PMMA	No window	93	30	8
	4.2-4.6	93		
	4.2-6.3	95		

The difference in emission preference of gamma and neutron in the cylinder phantom results and cube phantom results is due to the change in BP position relative to the centre of the simulation coordinate system. The simulation registers the gamma (and neutron) with respect to the coordinate system centre, which is at the centre of each phantom. This will be discussed further in section 4.2.1.2. From our results, the gamma emission angular preference is validated to be slightly backward peaked, while the neutron emission is forward peaked.

A summary of cube phantom results of gamma and neutron emission yields reaching the detection sphere is presented in Table 12. As expected, the 4.2-6.3 MeV window yields the greater number of gammas being registered and thus offers the higher gamma-neutron ratio.

Table 12: Summary of gamma and neutron yields (in percentage) traversing the detection sphere once emitted from the cube phantom. The simulation statistical uncertainties are given.

	Energy window (MeV)	Number of gammas per incident proton, N_g (%)	Number of neutrons per incident proton, N_n (%)	Ratio, N_g/N_n
Water	No window	33.776 ± 0.018	13.817 ± 0.012	2.4445 ± 0.0025
	4.2-4.6	1.544 ± 0.004		0.1117 ± 0.0003
	5.0-5.4	1.077 ± 0.003		0.0779 ± 0.0002
	5.9-6.3	0.694 ± 0.003		0.0502 ± 0.0002
	4.2-6.3	3.979 ± 0.006		0.2880 ± 0.0005
PMMA	No window	32.125 ± 0.018	15.030 ± 0.012	2.1374 ± 0.0021
	4.2-4.6	1.539 ± 0.004		0.1024 ± 0.0003
	4.2-6.3	2.935 ± 0.005		0.1953 ± 0.0004

Using the cube PMMA phantom, the energy of the proton beam was varied (150-200 MeV, with 10 MeV intervals) in order to observe the shifting BP position (Figure 31) and the influence on the gamma angular preference (Figure 32). At each energy, $1x10^7$ incident protons were simulated. As expected, the range of the protons, and thus the BP position, decreases with decreasing initial proton energy, while the peaks become higher and thinner due to physical processes (energy and range straggling, see section 2.1.1.1). Table 13 presents the BP position, beam range (50% fall-off), and gamma angular preference (with an uncertainty of 5^o) with respect to the centre of the coordinate system, as a function of proton beam energy.

Table 13: Bragg curve features and angular preference with respect to the centre of the coordinate system, as a function of proton beam energy.

Proton beam energy (MeV)	BP position (mm) (±1 mm)	Beam range (mm) (±1 mm)	Gamma angular preference (degree) (±5^o)
150	133	135	112
160	149	151	108
170	165	168	104
180	182	186	100
190	200	204	95
200	219	223	90

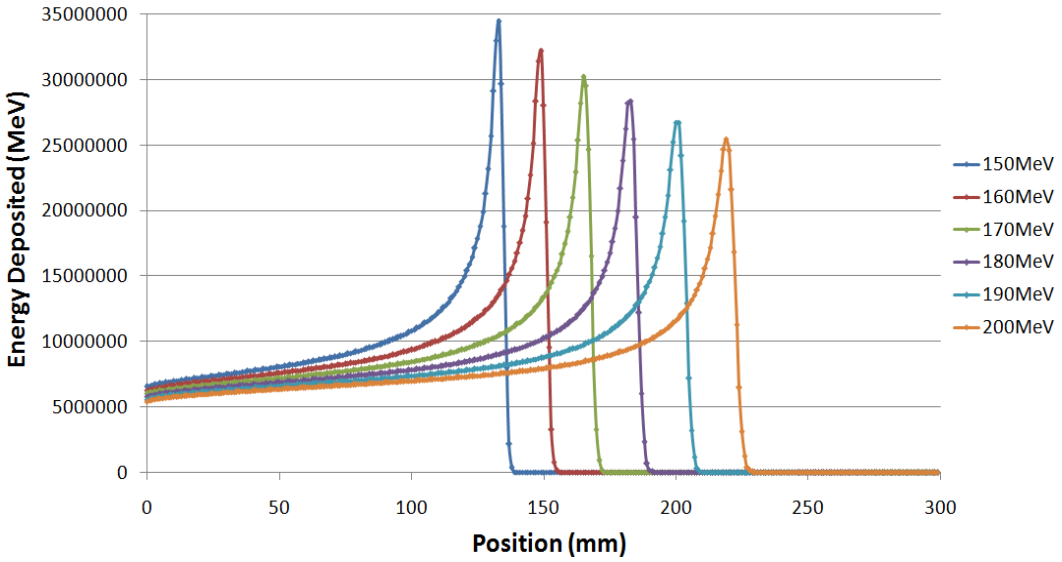

Figure 31: Bragg curves of varying proton beam energy. 1x10^7 events were executed.

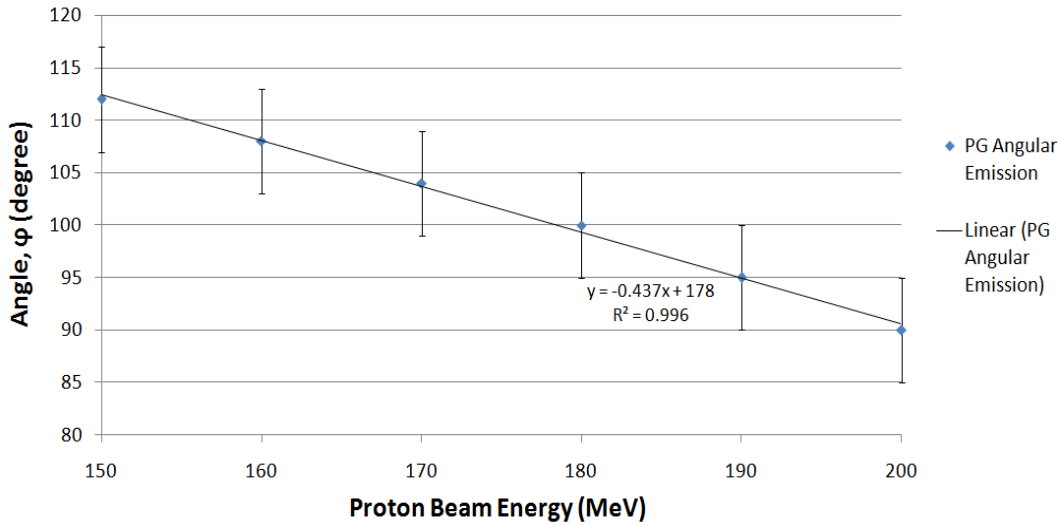

Figure 32: Gamma emission angular preference as a function of the proton beam energy.

The angular preference of gamma emission therefore also changes with proton beam energy, the dependency is shown in Figure 32 for beam energy from 150 to 200 MeV (10 MeV intervals). This plot illustrates that with increasing proton beam energy, the gamma angular emission preference decreases. It should be noted however that the BP position shifts relative to the coordinate system centre with varying beam energy, while the point at which the data is registered remains the same (i.e. at the centre of the coordinate system, which is at position 150 mm in Figure 31). What needs to be noted in Figure 32 is the linearity of the plot, such that the angle decreases in ~5^o intervals with increasing beam energy intervals. This suggests that the gamma emission angle relative to the BP remains somewhat constant in each case.

4.2.1.2 Effect of the Phantom Shape on the Prompt Gamma Emission

The effect of a cubic and, alternatively, cylindrical water phantom on the PG emission was studied. The location of the BP changes when considering the two shapes because of the different size of the phantom along the direction of incidence of the proton beam (see Figure 33). So the BP location in the cylinder phantom is at about the coordinate centre, whereas in the cube phantom the BP is shifted. Hence, the gamma emission preference is $\varphi \sim 110^{o}$ in the cylinder phantom and $\varphi \sim 90^{o}$in the cube phantom with respect to the coordinate centre.

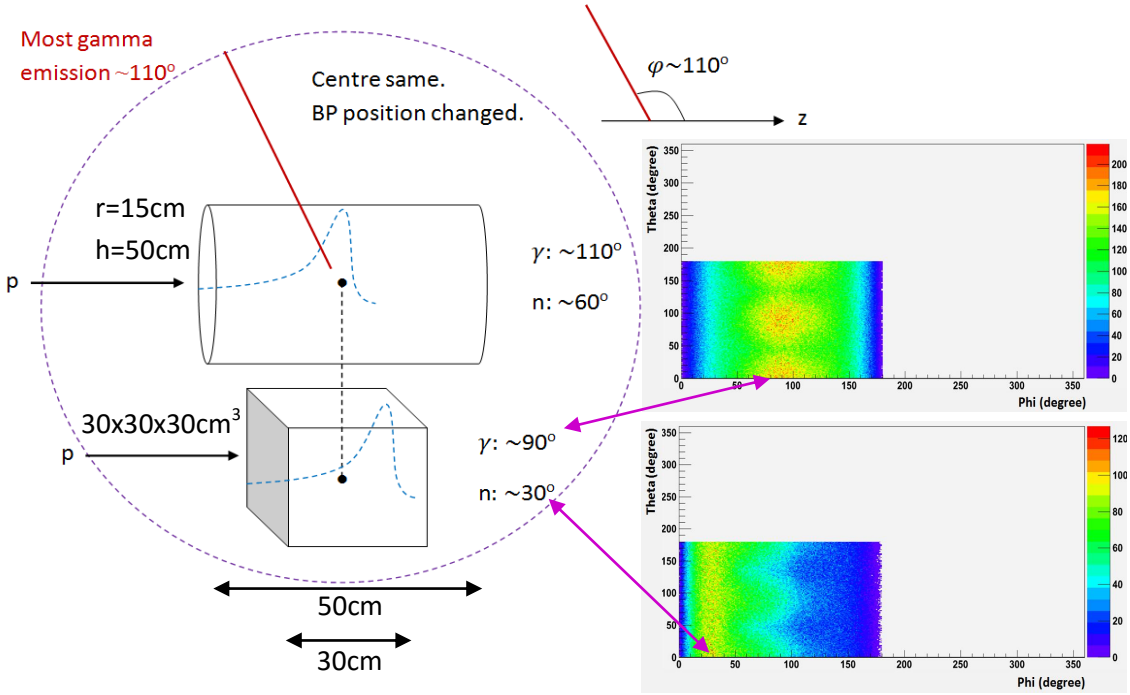

Figure 33: Illustration comparing the cylinder phantom with the cube phantom, in which the proton incidence position is shifted and the Bragg peak position is also shifted with respect to the global system of coordinates. 2D angular distribution plots on the right are the cube phantom results for gamma (top) and neutron (bottom) when traversing the detection sphere; data obtained with Geant4, $1x10^{7}$ events were executed.

The neutron emission was found to be $\varphi \sim 60^{o}$ in the cylinder phantom and $\varphi \sim 30^{o}$ in the cube phantom with respect to the coordinate system centre; this is simply due to the less absorption material before the neutrons escape the cube phantom, thus being more forward peaked. The 2D gamma and neutron emission plots for the cube phantom are also included in Figure 33 for observation.

To verify the simulation, the cylinder phantom was then compared to a rectangular phantom (30x30x50 cm^{3}) of the same length, depicted in Figure 34. The results show that the gamma emission angular preference is $\varphi \sim 110^{o}$ and the neutron emission preference is $\varphi \sim$

60^{o} with respect to the coordinate system centre, in both phantoms. Hence, regardless of the phantom geometry - as long as the BP position is the same - the emission preference will be consistent, as expected. The neutron emission is also the same since the same absorption thickness is present before the neutrons leave the phantom.

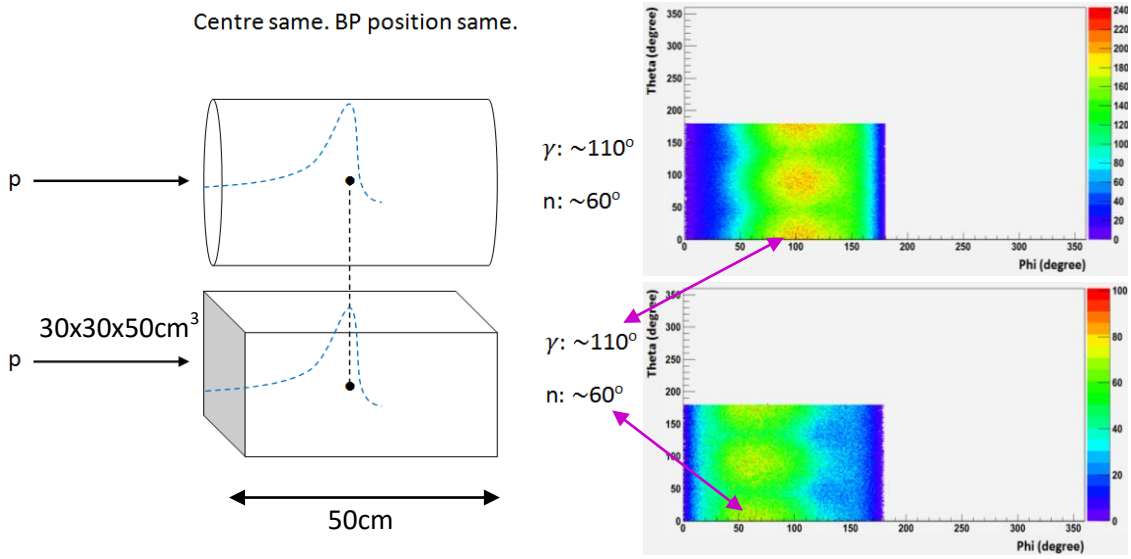

Figure 34: Illustration demonstrating the similarities of the cylinder phantom and a rectangular phantom, in which the proton incidence position and Bragg peak position are the same for both phantoms with respect to the global system of coordinates. 2D angular distribution plots on the right are the rectangle phantom results for gamma (top) and neutron (bottom) when traversing the detection sphere; data obtained with Geant4, $1x10^{7}$ events were executed.

When shifting the 30x30x30 cm^{3} cubic phantom along the opposite direction of incidence of protons, such that the BP is in the same position when considering the cubic and cylindrical phantom with respect to the global system of coordinates (see Figure 35), the gamma angular preference is $\varphi \sim 110^{o}$ in both phantoms, and the neutron emission preference is $\varphi \sim 60^{o}$ in the cylinder and $\varphi \sim 30^{o}$ in the cube (due to different absorption thickness). Again, it is shown that regardless of the geometry, given that the BP position is the same, the gamma emission preference is consistent.

Therefore, although our results have shown different emission preferences for the cylinder and cube geometry phantoms, the results are consistent, such that the angular preference of gamma emission is slightly backward relative to the BP. In addition, we discuss why the azimuthal emission is isotropic for the cylinder phantom but not for the cube phantom. As mentioned, this is simply due to the geometry of the phantom, and the material

absorption thickness prior to the gamma (and neutron) leaving the phantom. The cylinder yields an isotropic θ (i.e. the xy plane) emission because the path length for the gamma (and neutron) leaving the phantom (from the centre) is the same in all directions of θ.

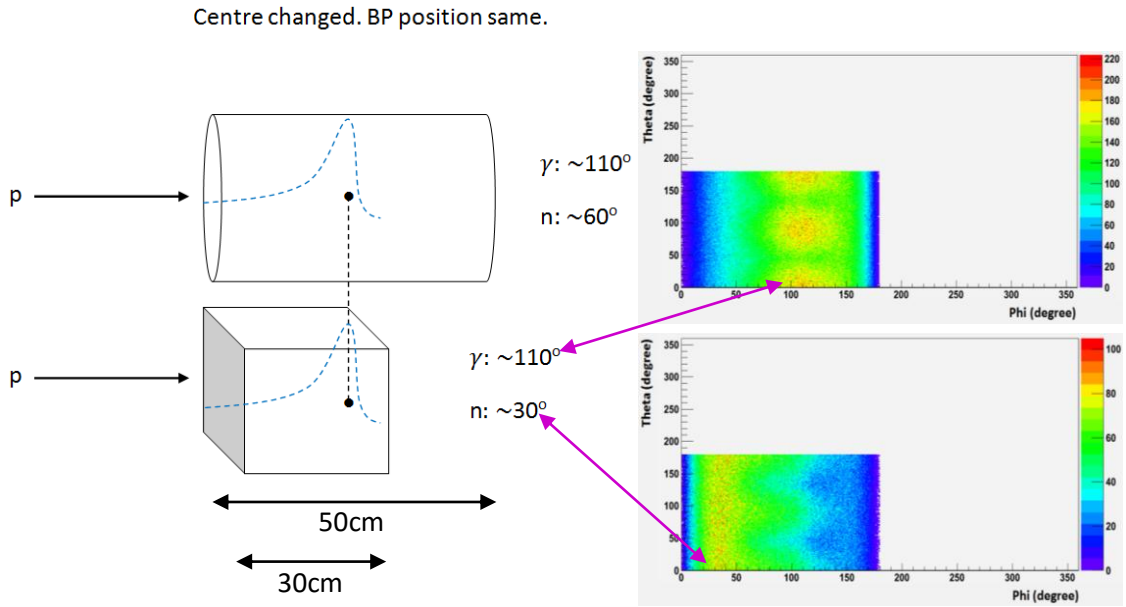

Figure 35: Illustration comparing the cylinder phantom with the cube phantom, in which the proton incidence position and Bragg peak position are the same for both phantoms with respect to the global system of coordinates. 2D angular distribution plots on the right are the cube phantom results for gamma (top) and neutron (bottom) when traversing the detection sphere; data obtained with Geant4, $1x10^7$ events were executed.

4.2.1.3 Emission Characteristics of Prompt Gamma with the Detection Cylinder

From the previous study (section 4.2.1.2) it is clear that a cylindrical phantom is more suitable to study PG emission, as the emission is isotropic with respect to θ. Therefore it was decided to study the spatial distribution properties of gamma and neutron emission leaving the proton-irradiated phantom with a detection cylinder, substituting the sphere, having the same length as the cylinder phantom.

Figure 36 shows the angle θ (see section 3.2) of the gamma rays and neutrons when traversing the surface of the detection cylinder with respect to the position z. As expected, the emission is isotropic with respect to θ. The gamma emission is slightly backward peaked, whereas the neutron emission is forward peaked, confirming the results of section 4.2.1.1. In the considered geometrical setup, the BP position corresponds to about 0 mm (water phantom) and -30 mm (PMMA phantom) with respect to the centre of the coordinate system.

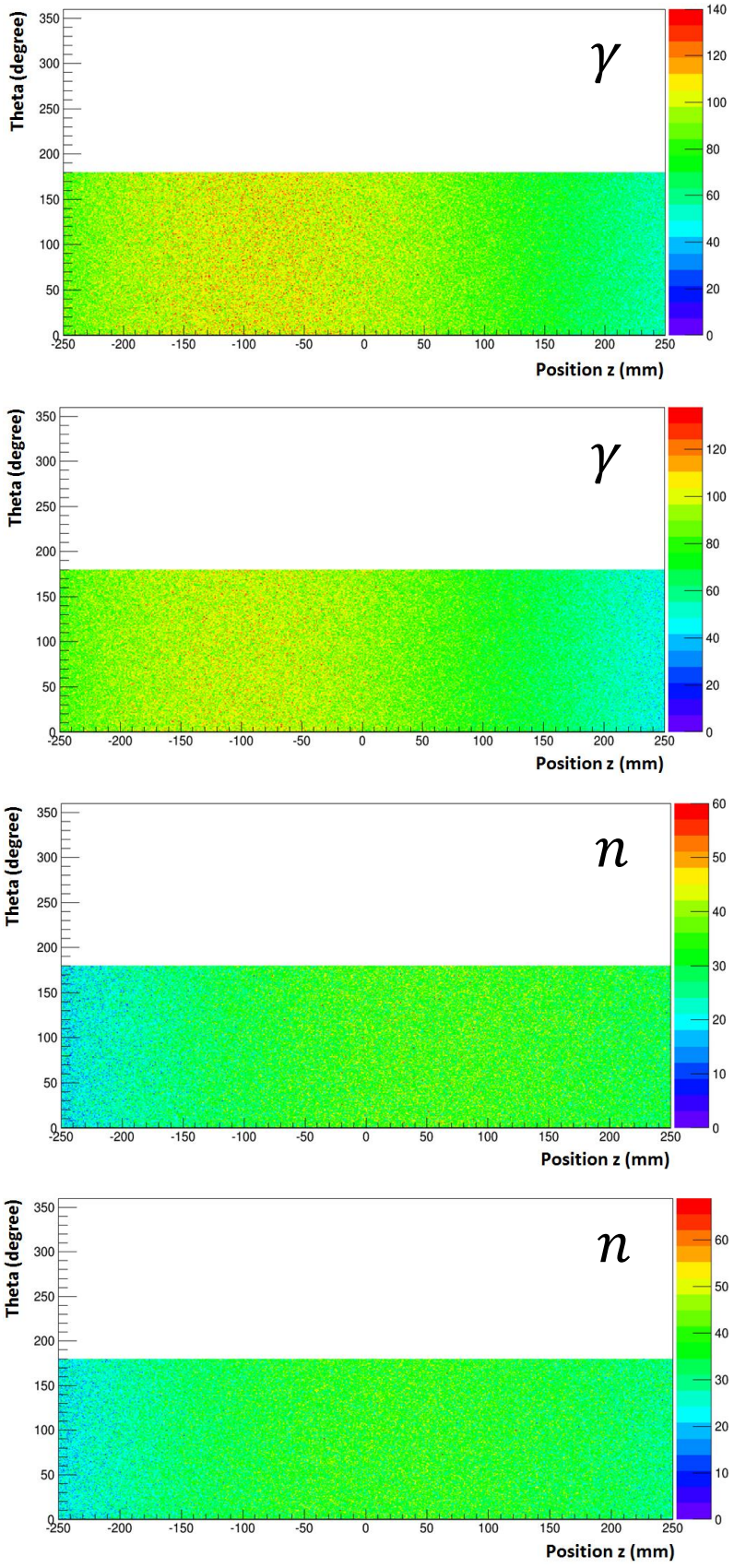

Figure 36: Spatial distribution ($\boldsymbol{\theta}$ and Position z, see Figure 10, Chapter 3) of gamma rays ($\boldsymbol{\gamma}$) and neutrons ($\boldsymbol{n}$) emission when traversing the detection cylinder. The radiation is emitted from a cylinder phantom of water (top and third) and PMMA (second and bottom). The colour code represents the number of counts provided in the right-hand axis of each figure. 5x10^{7} events were executed. Data obtained with Geant4.

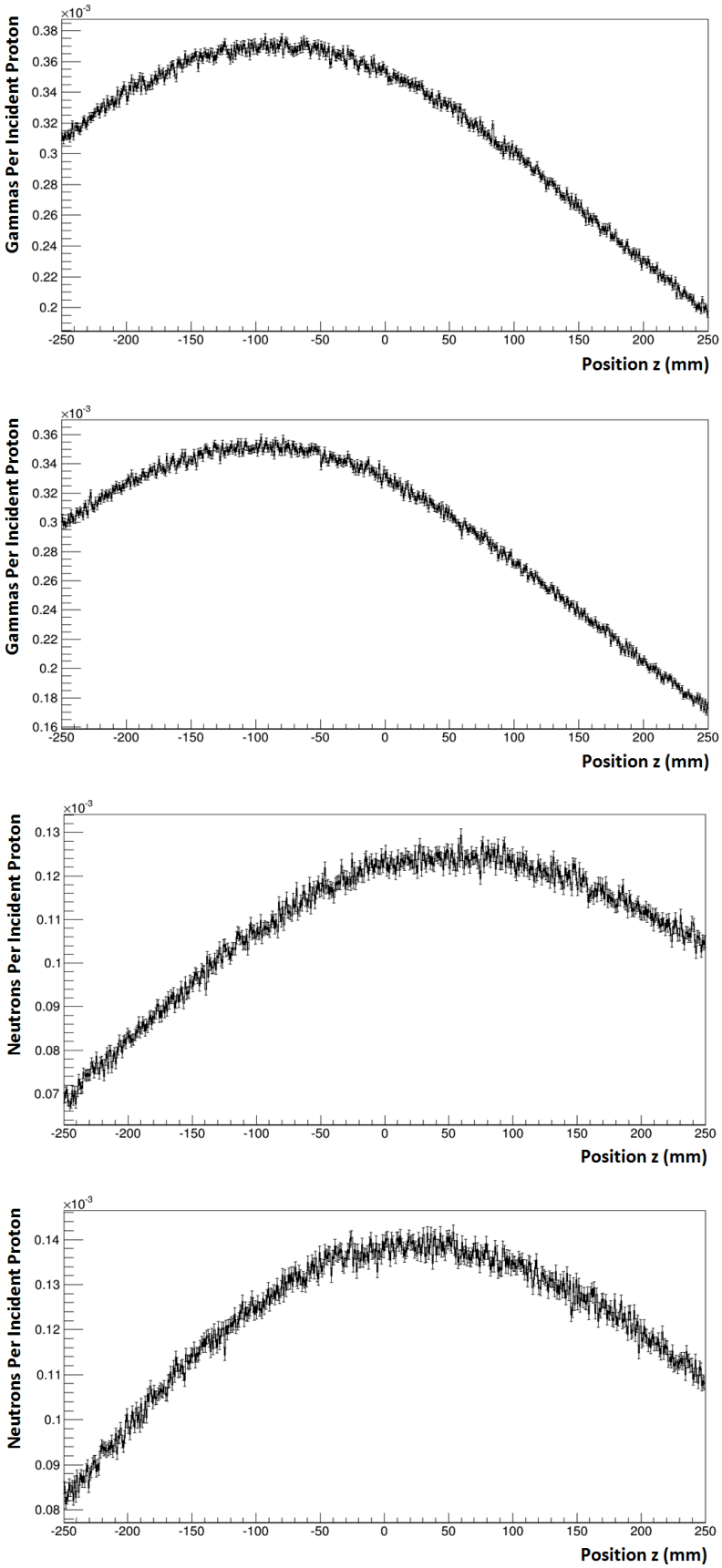

Figure 37: Distribution of gamma rays and neutrons traversing the detection cylinder, once emitted from the cylinder phantom. Top and third: water phantom. Second and bottom: PMMA phantom. Data obtained with Geant4.

Figure 37 shows the frequency of the position of gamma rays and neutrons when traversing the detection cylinder. The gamma emission has a maximum when reaching the detection cylinder at around -80 mm from the water phantom, and around -70 mm from the PMMA phantom, with respect to the BP position. These correspond to $\sim 11^{o}$ backward peaked gamma emission in water, and $\sim 8^{o}$ backward peaked in PMMA, relative to the BP.

The gamma and neutron emission traversing the detection cylinder was again observed within the energy windows of interest. Table 14 presents the preferential position of gammas and neutrons when traversing the detection cylinder once emitted from the cylinder phantom.

Table 15 summarises the gamma and neutron yield ratios. It shows that the 4.2-6.3 MeV energy window yields the higher signal-to-noise ratio, with $N_g/N_n \cong 0.33$ from the water phantom, and $N_g/N_n \cong 0.22$ from the PMMA phantom. The gamma yields within this window are around 1.8% and 1.3% per incident proton from the water and PMMA phantoms, respectively.

Table 14: Preferential position of gamma and neutron emission traversing the detection cylinder once emitted from the cylinder phantom.

	Energy window (MeV)	Preferential position on the detection cylinder (mm) (±1 mm)		Gamma angular preference, φ, with respect to the BP position (degree) ($\pm 5^{o}$)
		Gamma	Neutron	
Water	No window	-80	60	11
	4.2-4.6	-90		
	5.0-5.4	-100		
	5.9-6.3	-100		
	4.2-6.3	-100		
PMMA	No window	-100	20	8
	4.2-4.6	-100		
	4.2-6.3	-100		

Table 15: Gamma-neutron ratios for emission traversing the detection cylinder once emitted from the cylinder phantom. The simulation statistical uncertainties are given.

	Energy window (MeV)	Number of gammas per incident proton, N_g (%)	Number of neutrons per incident proton, N_n (%)	Ratio, N_g/N_n
Water	No window	15.866 ± 0.006	5.454 ± 0.003	2.9091 ± 0.0019
	4.2-4.6	0.689 ± 0.001		0.1263 ± 0.0002
	5.0-5.4	0.480 ± 0.001		0.0880 ± 0.0002
	5.9-6.3	0.320 ± 0.001		0.0587 ± 0.0002
	4.2-6.3	1.777 ± 0.002		0.3258 ± 0.0004
PMMA	No window	14.806 ± 0.005	6.136 ± 0.004	2.4130 ± 0.0018
	4.2-4.6	0.702 ± 0.001		0.1144 ± 0.0002
	4.2-6.3	1.319 ± 0.002		0.2150 ± 0.0004

In conclusion, our results show that the optimal position for a PG imaging system is slightly before the expected proton range, such that the angular preference of PG emission has been determined to be slightly backward peaked relative to the BP, while neutrons are forward peaked. Thus PG emission is dependent on the BP position. Few studies have focused in detail on the PG angular/spatial emission. A recent study looking into the angular dependence of PG emission during PT found that backward angles are preferential for PG detection, while no significant dependence is seen from the azimuthal angles.[71] Our results agree with these findings, while our study further explored the PG angular emission dependence on target material and geometry. We also investigated the angular dependence of PG emission in the various energy windows, and compared all data to the neutron emission.

4.2.2 Time Properties of Prompt Gamma Detection

4.2.2.1 Characterisation of the TOF of Prompt Gamma with the Detection Cylinder

The TOF of gammas and neutrons was studied when traversing the detection cylinder to determine an optimal timing window for improving the gamma-neutron ratio. The cylinder phantom was made of water and PMMA, alternatively. Figure 38 shows the TOF frequency of gamma rays and neutrons traversing the detection cylinder. We find that gammas are mostly emitted at around 3 ns, and neutrons are well differentiated as they are emitted after about 4 ns, peaking at around 6 ns. Similar results were obtained in the previous stage of the work when a cubic phantom and a detection sphere were adopted. Studies into the timing properties of gamma (and neutrons) have shown similar TOF properties as obtained in our

results; the gamma TOF distribution peaks at around 2-3 ns[54,55,72], while neutrons are being emitted after about 3 ns.[54]

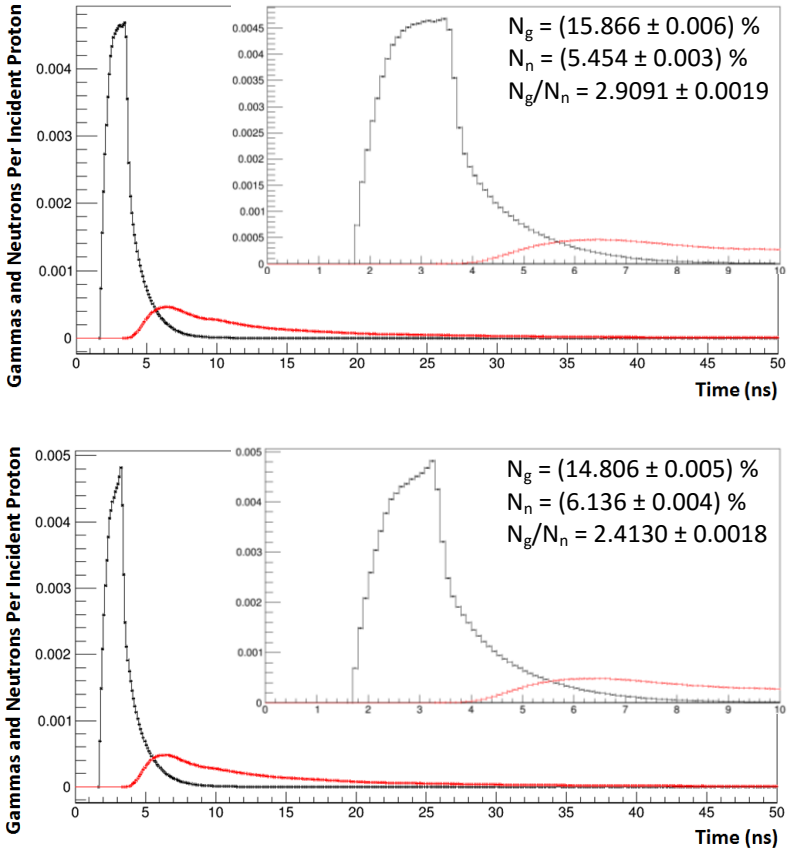

Figure 38: TOF frequency of gamma rays (black) and neutrons (red) traversing the detection cylinder, once emitted from the cylinder phantom. No window applied. Top: water phantom. Bottom: PMMA phantom. Data obtained with Geant4.

Applying the 4.2-4.6 and 4.2-6.3 MeV energy windows on the gamma emission, we find that most PG rays have a TOF of around 3.5 ns from the water phantom, and around 3.3 ns from the PMMA phantom (see Figure 39). The gamma rays and neutrons are still well differentiated and the 4.2-6.3 MeV yields the higher signal-to-noise ratio, as expected. The ratio of gamma rays in the 4.2-6.3 MeV window to the total number of neutrons is $N_g/N_n \cong 0.33$ from water, and $N_g/N_n \cong 0.22$ from PMMA.

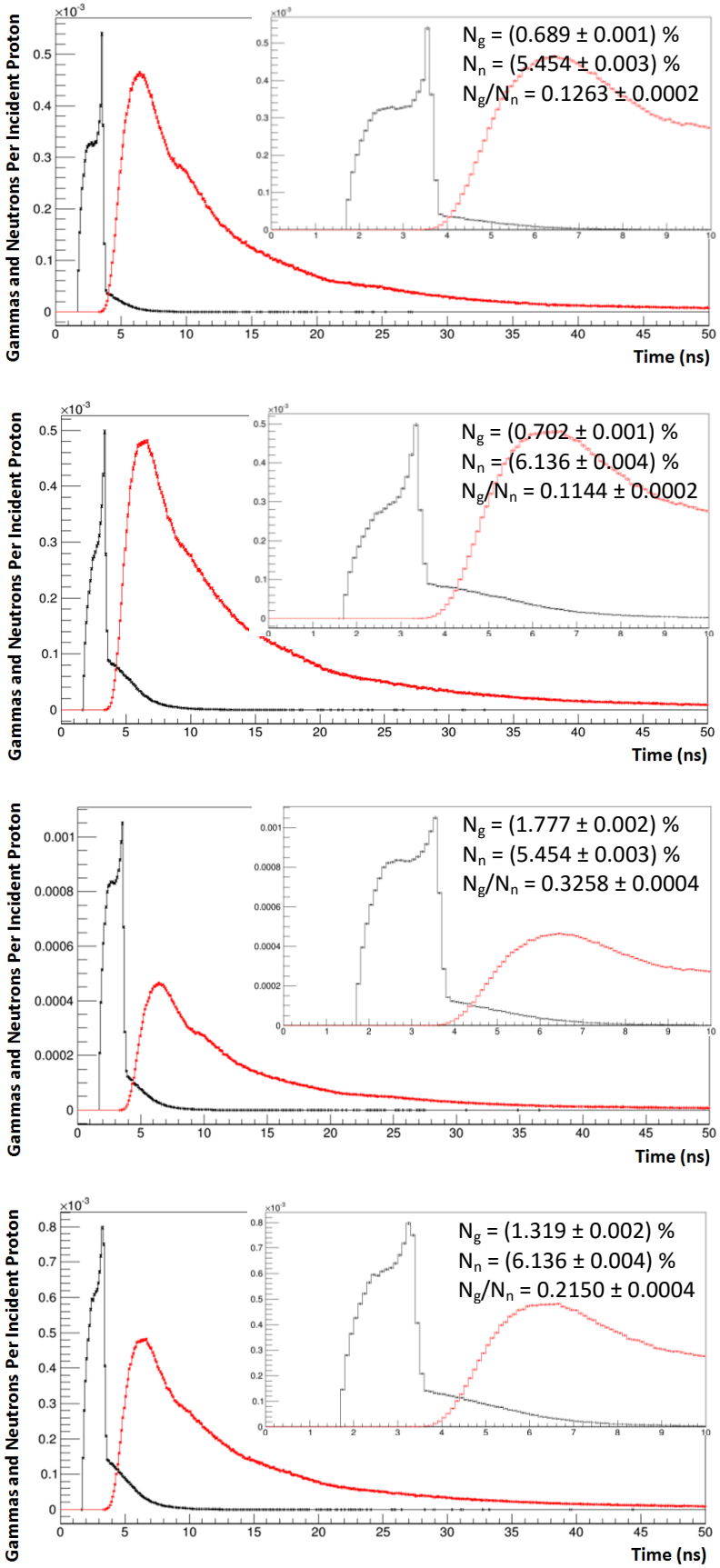

Figure 39: TOF frequency of gamma rays (black) and neutrons (red) traversing the detection cylinder, once emitted from the cylinder phantom. Top and second: 4.2-4.6 MeV window. Third and bottom: 4.2-6.3 MeV window. Top and third: water phantom. Second and bottom: PMMA phantom. Data obtained with Geant4.

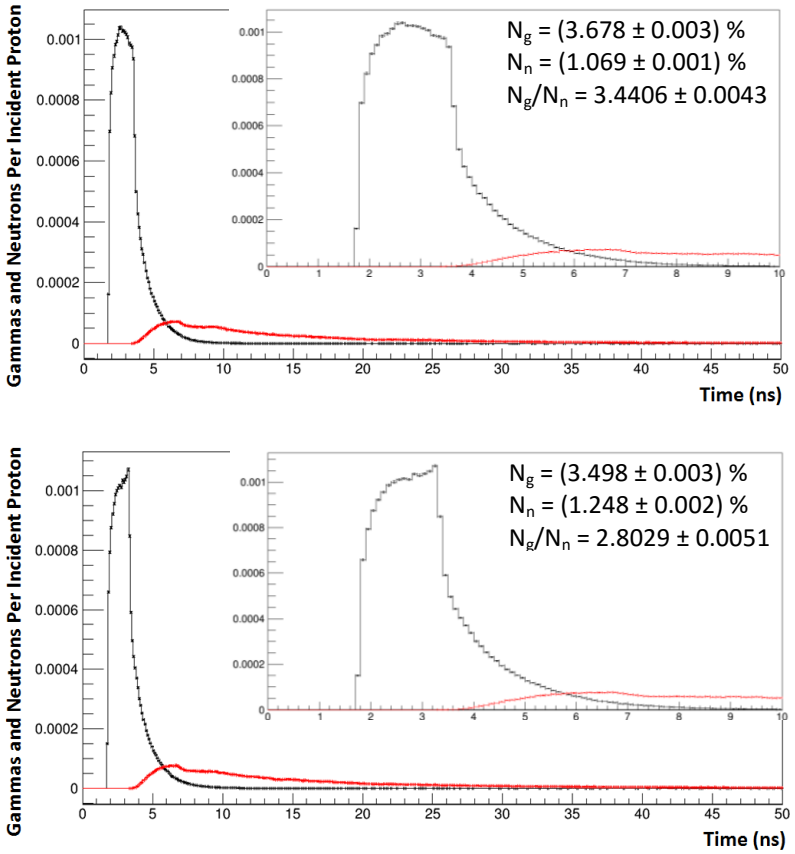

Figure 40: TOF frequency of gamma rays (black) and neutrons (red) traversing the detection cylinder once emitted from the cylinder phantom, with -150 mm to -50 mm spatial window applied to gamma and neutron emission. Top: water phantom. Bottom: PMMA phantom. Data obtained with Geant4.

The gamma and neutron radiation traversing the detection cylinder between -150 mm to -50 mm (called *spatial window* in the following) was selected, corresponding to the preferential position of gamma emission seen in our previous results (see section 4.2.1.3). The plots are presented in Figure 40, where the gamma-neutron ratio increases from the case where no window is applied (see Figure 38).

The gamma-neutron ratio can be improved further by applying the spatial window in combination with the energy windows (see Figure 41). The gamma and neutron TOF distribution remain well differentiated, with PG rays being mostly emitted with a TOF of around 2-4 ns. The 4.2-6.3 MeV window again yields the higher gamma-neutron ratios in both phantoms, with $N_g/N_n \cong 0.38$ from water, and $N_g/N_n \cong 0.25$ from PMMA.

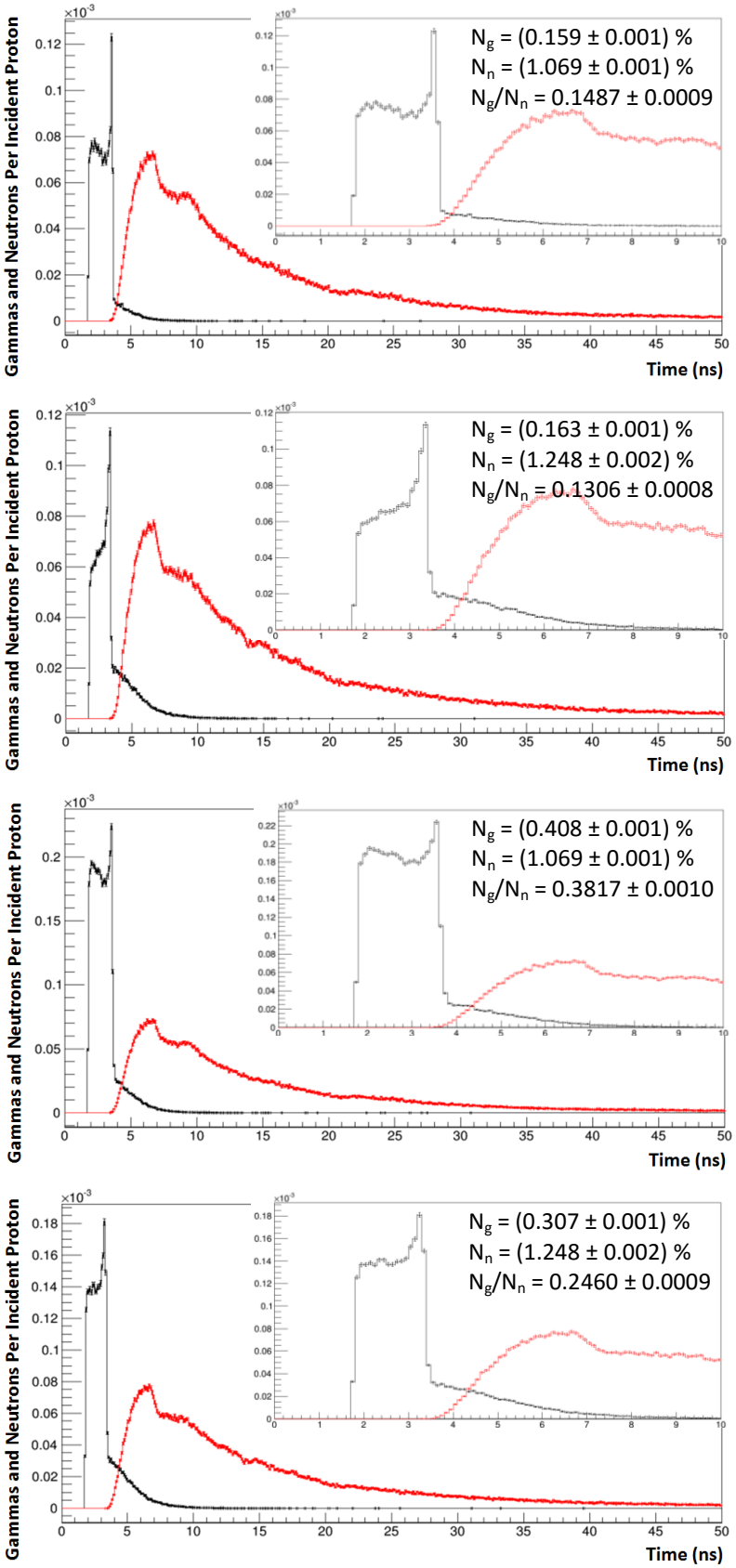

Figure 41: TOF frequency of gamma rays (black) and neutrons (red) traversing the detection cylinder once emitted from the cylinder phantom, with -150 mm to -50 mm spatial window applied to gamma and neutron emission. Top and second: 4.2-4.6 MeV window. Third and bottom: 4.2-6.3 MeV window. Top and third: water phantom. Second and bottom: PMMA phantom. Data obtained with Geant4.

Table 16 summarises the gamma and neutron yields reaching the detection cylinder, with the corresponding gamma-neutron ratio. Applying the preferential spatial window for PG detection significantly reduces the number of registered neutrons and increases the signal-to-noise ratio. Hence, applying the spatial window in combination with the energy window further improves the gamma-neutron ratio. As expected, the 4.2-6.3 MeV gamma energy window yields a higher signal-to-noise ratio compared with the 4.2-4.6 MeV window, since it provides an increased number of gamma statistics.

Table 16: Summary of gamma and neutron yields (in percentage) traversing the detection cylinder once emitted from the cylinder phantom. No energy window applied to neutrons. The simulation statistical uncertainties are given.

	Window	Number of gammas per incident proton, N_g (%)	Number of neutrons per incident proton, N_n (%)	Ratio, N_g/N_n
Water	No window	15.866 ± 0.006	5.454 ± 0.003	2.9091 ± 0.0019
	4.2-4.6 MeV	0.689 ± 0.001		0.1263 ± 0.0002
	4.2-6.3 MeV	1.777 ± 0.002		0.3258 ± 0.0004
	-150 to -50 mm	3.678 ± 0.003	1.069 ± 0.001	3.4406 ± 0.0043
	4.2-4.6 MeV and -150 to -50 mm	0.159 ± 0.001	1.069 ± 0.001 (-150 to -50 mm)	0.1487 ± 0.0009
	4.2-6.3 MeV and -150 to -50 mm	0.408 ± 0.001	1.069 ± 0.001 (-150 to -50 mm)	0.3817 ± 0.0010
PMMA	No window	14.806 ± 0.005	6.136 ± 0.004	2.4130 ± 0.0018
	4.2-4.6 MeV	0.702 ± 0.001		0.1144 ± 0.0002
	4.2-6.3 MeV	1.319 ± 0.002		0.2150 ± 0.0004
	-150 to -50 mm	3.498 ± 0.003	1.248 ± 0.002	2.8029 ± 0.0051
	4.2-4.6 MeV and -150 to -50 mm	0.163 ± 0.001	1.248 ± 0.002 (-150 to -50 mm)	0.1306 ± 0.0008
	4.2-6.3 MeV and -150 to -50 mm	0.307 ± 0.001	1.248 ± 0.002 (-150 to -50 mm)	0.2460 ± 0.0009

Figure 42 shows the frequency of gamma rays and neutrons traversing the detection cylinder with respect to the position along the detection cylinder with a 2-4 ns timing window applied. This result demonstrated that the optimal TOF window is around 2-4 ns such that applying both a TOF window and the energy windows can improve PG imaging formation, whereby it eliminates the presence of neutrons.

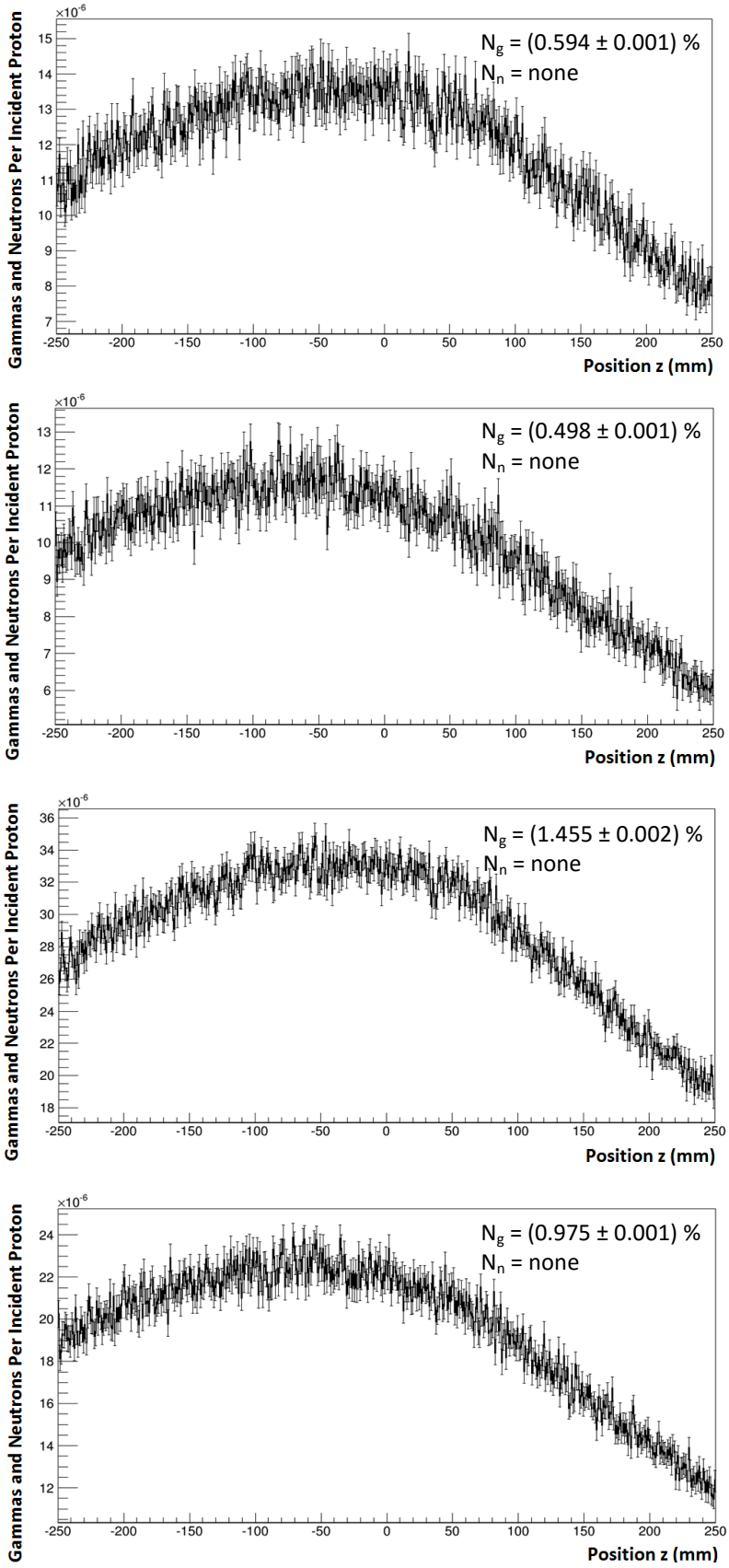

Figure 42: Distribution of gamma rays traversing the detection cylinder once emitted from the cylinder phantom, with 2-4 ns time window applied to gamma and neutron emission. Top and second: 4.2-4.6 MeV window. Third and bottom: 4.2-6.3 MeV window. Top and third: water phantom. Second and bottom: PMMA phantom. Data obtained with Geant4.

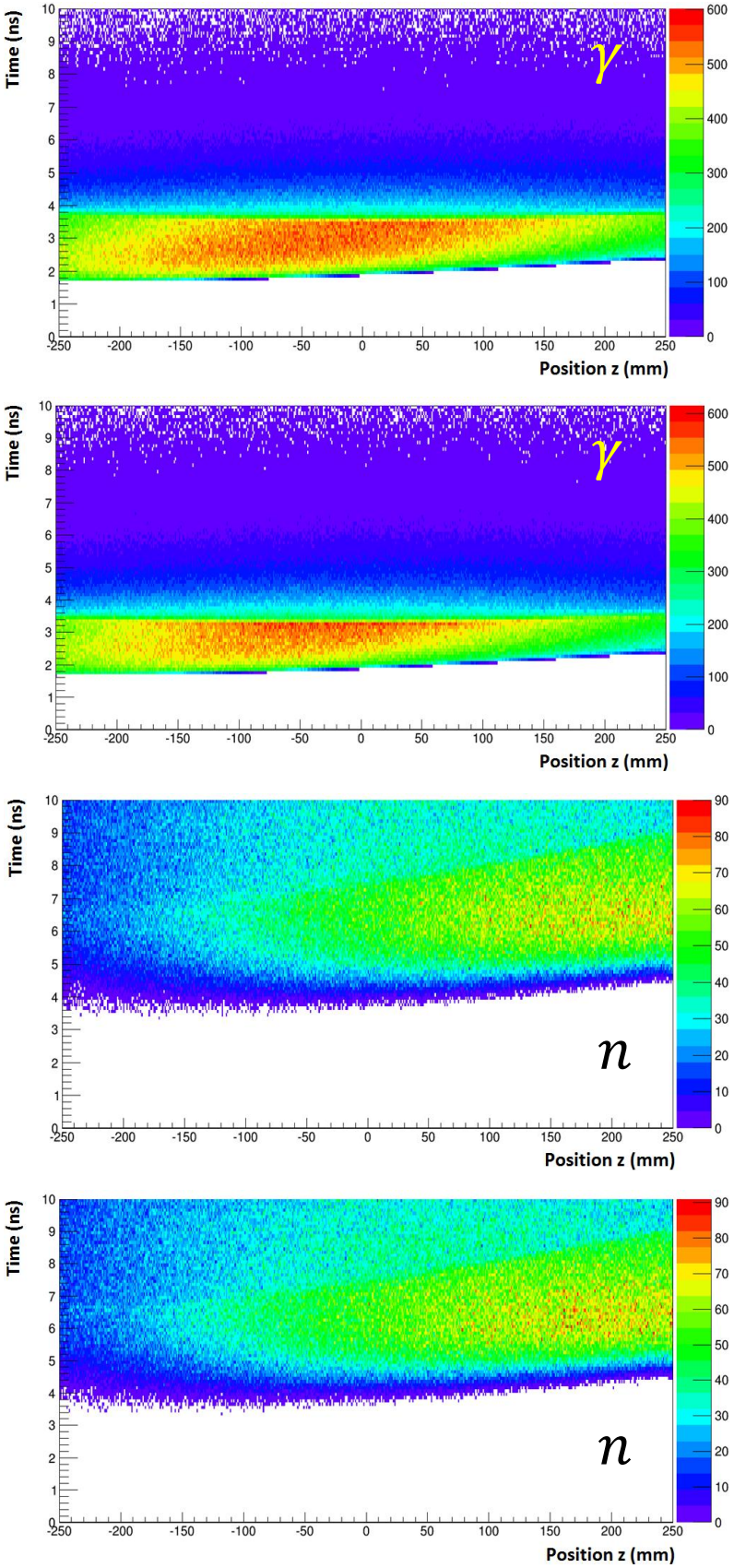

Figure 43: TOF of gamma rays (γ) and neutrons (n) traversing the detection cylinder, with respect to the position along the detection cylinder. No window applied. Top and third: water phantom. Second and bottom: PMMA phantom. The colour code represents the number of counts provided in the right-hand axis of each figure. $5x10^7$ events were executed. Data obtained with Geant4.

The TOF of gamma rays and neutrons traversing the detection cylinder with respect to the position along the detection cylinder is presented in Figure 43. The gamma emission is predominantly emitted between about 2-4 ns and mostly in the region of the BP, while neutrons are predominantly emitted after around 4 ns and mainly after the BP (i.e. neutrons are forward peaked).

Thus we validated that PG rays are mainly emitted at around 3 ns, with neutrons being well differentiated with emission after around 4 ns. Hence, applying a TOF window is a background suppression technique for improving the PG signal-to-noise ratio by differentiating the PG signal and the background (neutrons). Combining this time window with the optimal energy window and positioning the imaging system at the preferential location further improves PG image formation. So although high energy PG detectors are currently unavailable, we have demonstrated that with our proposed strategies gamma detectors can provide efficient PG imaging for effective beam range verification in PT.

4.3 Modelling Prompt Gamma Detection with an Ideal Detector

4.3.1 Estimated Number of Primary Protons Required

In the detector modelling simulations, we have defined the detector to be fully BGO (i.e. with no pixel array), however for this estimation we assume that one unit space on the face of the detector is 1 pixel. So for 1 pixel, we want the statistical deviation (error) to be less than 10%:

→ 1 pixel = $\Delta N/N = 1/\sqrt{N} < 10\%$ → $N = 10^2 = 100$

So, we want the number of gammas in one pixel to be ≥ 100.

The detector face is 45x45 mm^2 = 2,025 mm^2:

→ so the total number of gammas needed to reach the detector is 2025 x 100 = **2.025×10^5**

When the number of primary protons in the beam is 10^7, the number of gammas reaching the detection sphere is 3,209,450 (data from PMMA cube phantom simulation results).

Note, the relationship we are considering in this calculation can be written as $N_{\gamma,D} = \varepsilon_{\text{eff}} \, . \, N_{\gamma}$, where ε_{eff} is the detector efficiency.

The area of a sphere is $A = 4\pi r^2$ → A = 4 x π x (500 mm)^2 = 3,141,592 mm^2

→ the ratio from sphere to detector: 3,141,592mm^2 ÷ 2,025 mm^2 = 1,551

→ the number of gammas from detection sphere to detector is: 3,209,450 ÷ 1,551 = 2,069

That is, the number of gammas reaching the detector, with 10^7 primary protons, $N_{\gamma,D}$ **= 2,069**.

But we want 2.025x10^5 gammas reaching the detector (as shown above):

→ 2.025x10^5 ÷ 2,069 = 98 ≈ 100

That is, we need about 100 times more gammas.

→ 10^7 x 100 = 10^9

Therefore, we need **10^9** primary protons to meet the necessary number of gammas reaching the detector to have a standard deviation less than 10%.

To simply check this value → 10^7 ÷ 2,069 = 4,833

→ 10^9 ÷ 4,833 = 206,911

Hence, having 10^9 primary protons yields ~206,900 gammas reaching the detector, which is greater than the required 2.025x10^5 gammas, hence satisfactory for use in the following simulations.

4.3.2. BGO Detector Response with Proton Pencil Beam

To aid the design and development of an optimal detection system for PG imaging, the ideal response of a BGO detector was investigated when placed at 90^o with respect to the PMMA cube phantom, as shown in Figure 11, Chapter 3. Figure 45 shows the detector response (total energy deposition per event) from the 200 MeV proton beam incident on the face of the phantom. To compare the detector response with the gamma emission field, Figure 44 shows the energy spectrum of gamma rays traversing the detection sphere once emitted from the cube PMMA phantom. Even though the 4.44 MeV PG contributes significantly to the PG field at the distance where the detector is located (see Figure 44), its contribution to the PG signal in the BGO detector is very minor. This may be due to Compton scattering of photons within the detector and subsequently leaving the detector itself, as seen in Figure 45. To limit this problem, the size of the detector may need to be made bigger to absorb more PG rays. Nonetheless, Figure 45 shows that the 4.44 MeV PG peak can be seen in the detector response, and that this peak is more prominent than the other PG peaks.

In terms of efficiency, we find that the BGO detector in this study yields a higher efficiency for detecting the 4.2-6.3 MeV energy window compared with the 4.2-4.6 MeV window, since greater statistics are obtained with the larger energy window; keeping in mind that the PG rays within these energy windows are emitted with the same angular characteristics. That is, knowing the area of the detector as 2,025 mm^2, and with the area of the total sphere being 3,141,592 mm^2, the ratio of the two is $6.4x10^{-4}$. Using Monte Carlo and our already obtained results, it was determined that the ratio of the number of gammas per incident proton recorded in the detector to those reaching the sphere in the energy range 4.2-4.6 MeV is approximately $1.5x10^{-4}$. Similarly, the ratio of gammas per incident proton recorded in the detector to those reaching the sphere, in the energy range 4.2-6.3 MeV is approximately $2.1x10^{-4}$, thus giving a higher detector efficiency.

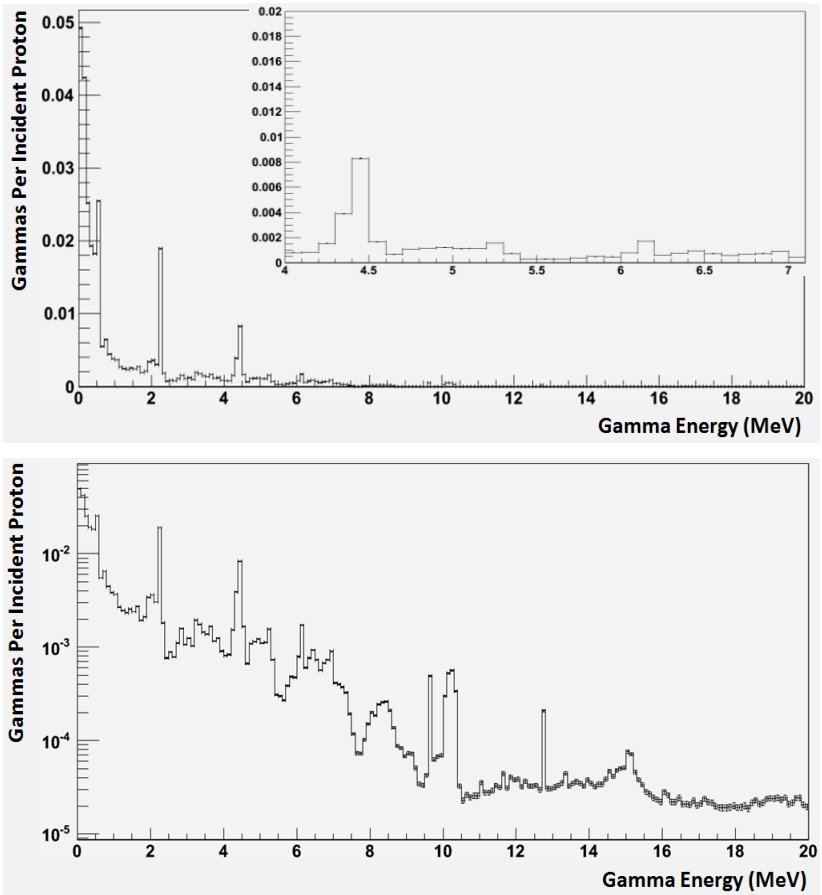

Figure 44: Gamma spectrum of gamma rays traversing the detection sphere once emitted from the proton-irradiated cubic PMMA phantom. $1x10^7$ events were executed. Top: Linear scale. Bottom: Logarithmic scale. Data obtained with Geant4.

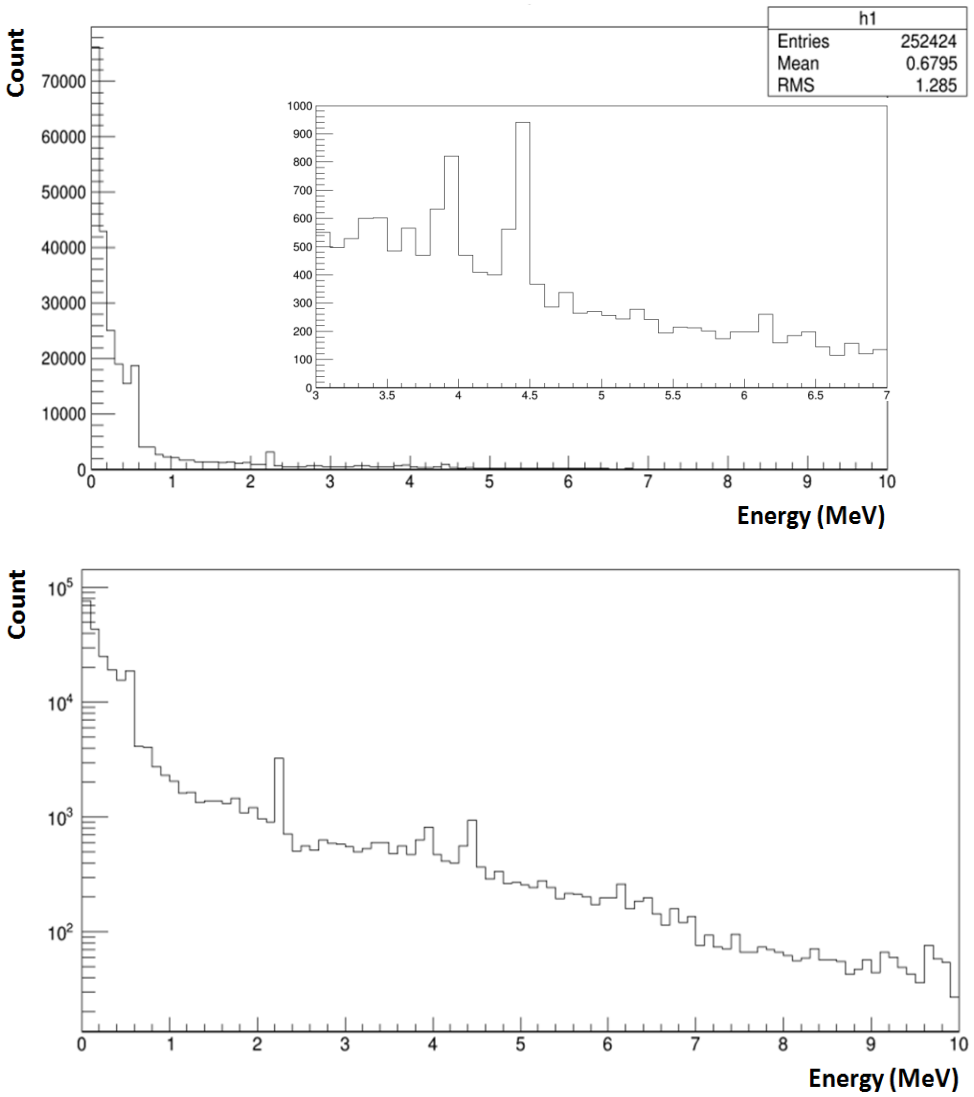

Figure 45: Detector response from 1x10[9] primary protons incident upon the cubic PMMA phantom. Top: Linear scale. Bottom: Logarithmic scale. Data obtained with Geant4.

To investigate in more depth the 4.44 MeV PG emission line observed in the detector response in Figure 45, the detector response deriving from a 4.44 MeV gamma beam directed toward the detector itself was investigated and the results are presented in Figure 46. We can identify the 4.44 MeV photopeak and the Compton edge responsible for the emission lines at lower energies. As seen, the single and double escape peaks are more prominent than the Compton edge. A single gamma can cause multiple physical interactions, it has been determined that for 4.44 MeV gamma rays interacting in BGO, the most important physical process is Compton scattering as it is responsible for 59% of the energy deposited, while pair production accounts for 38%, and the photoelectric effect is negligible at 3%.[73] Therefore, we find that the 4.44 MeV PG rays predominately interact via Compton scattering. A possible solution is to adopt Compton cameras, which have been studied for detecting PG rays as they

do not rely on traditional 2D collimation or complete absorption of the gamma rays (see section 2.2.2).[50]

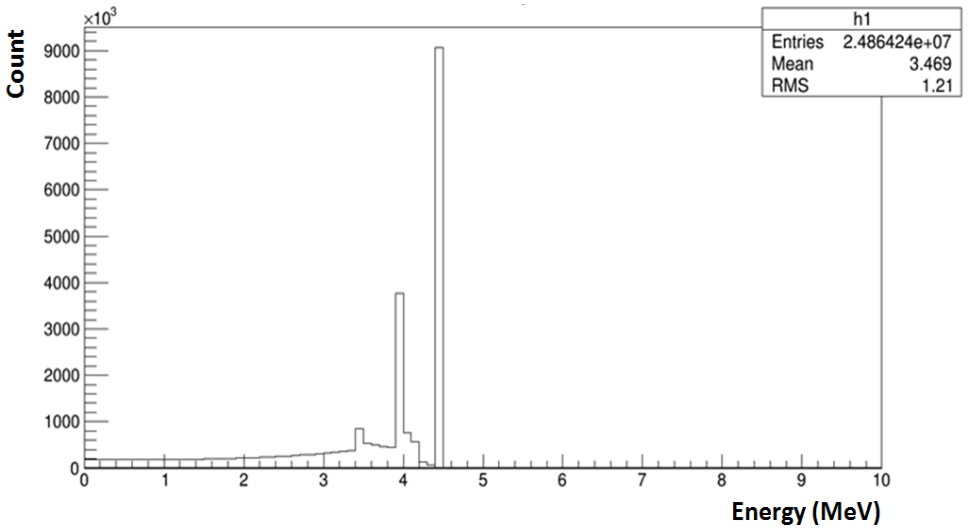

Figure 46: Detector response for 5x10^7 gammas of 4.44 MeV incident on the detector. Data obtained with Geant4.

This study shows that systems capable of detecting 4.44 MeV energy window gamma rays are required to allow PG imaging for range verification in hadron therapy. Our results have shown that a detector with high PG detection efficiency will allow good quality PG image formation, and with our study of the PG angular distribution we show that a strategy to improve such imaging formation is to position the detection system slightly backward (relative to the BP position) where gamma emission is dominant with less neutron influence. Applying an energy window and timing window can further improve the signal-to-noise ratio for better image formation. Other techniques, such as using a detector with higher detection efficiency or an array of detectors, can also improve the detection efficiency. Increasing the number of primary protons would also increase the number of detected PG rays.

Chapter 5

Conclusion

As part of a pilot study of a project to develop a novel *in-vivo* dose verification technique using the PG emission signal for real-time tracking of the BP during hadron radiation therapy delivery, we have investigated the PG emission and detection characteristics from high energy proton irradiation using extensive Monte Carlo simulations in this study. The PG emission characteristics in terms of energy spectra, yield and ratio with respect to neutrons, and quantified correlation with the BP have been investigated. The PG detection dependencies on its energy, spatial position, and TOF properties have been studied. The detector response from an ideal detector has then been modelled for potential optimal PG detection.

Geant4 Monte Carlo simulations have been performed to study the primary radiation of high energy proton irradiation in specific phantoms, and also the secondary radiation of PG rays and neutrons during the proton irradiation. Two homogeneous cylindrical phantoms of water and PMMA (ϕ30 cm x 50 cm) have been used in the simulations with a 200 MeV pencil proton beam. Cubic water and PMMA phantoms (30x30x30 cm^3) have also been examined. Two sensitive detection geometries have been investigated for PG and neutron detection characteristics; a detection sphere with 50 cm radius encompassing the phantom, and a detection cylinder (ϕ100 cm x 50 cm) coaxially surrounding the phantom. The yields and ratio of secondary radiation of PG rays and neutrons have been obtained. The quantitative correlation between the PG distribution and the Bragg curve in the phantoms have been extracted with different PG energy windows. The energy spectra, spatial spectra and TOF of the PG emission and detection from high energy proton irradiations have been extensively studied as compared to secondary neutrons. In addition, preliminary modelling of a practical BGO based detector (45x45x25 mm^3) for PG detection has been performed as compared to the detection sphere.

Our results show that PG emission exhibits relative high yields and well-distinguishable characteristic spectral lines at 4.44 MeV ($^{12}C^*$), 5.21 MeV ($^{15}O^*$) and 6.13 MeV ($^{16}O^*$) in both water and PMMA phantoms. The gamma spectra seen in our results agree well with already published work.[9,10,27,34,49,52,57] Furthermore, the PG yields in the 4.2-4.6 MeV energy range are

about 3% per incident proton in the water and PMMA cylindrical phantoms, with PG-neutron ratios of ~0.12 and ~0.11, respectively. In comparison, PG yields in the 4.2-6.3 MeV energy range are about 5-6% in water and PMMA, with PG-neutron ratios of ~0.30 and ~0.21, respectively.

The longitudinal distribution of the PG emission signal exhibits a strong correlation with the Bragg curve. However, the PG fall-off is seen to be not equal to the dose fall-off, which has also been noted previously.[26] Differences between the PG fall-off and BP fall-off have a variation from 0 to 7 mm with the PG energy windows observed in the water phantom, but a smaller variation of 1 to 2 mm with the energy windows observed in the PMMA phantom. The longitudinal PG distribution also has a strong dependence on the PG energy window. The 4.2-4.6 MeV window presents a ~4 mm fall-off difference in water and ~1 mm fall-off difference in PMMA. The fall-off difference in the 4.2-6.3 MeV window is ~4 mm in water and ~2 mm in PMMA. Considering these PG energy windows, which offer relatively higher statistics, the PG signal in the energy window of 4.2-4.6 MeV shows better fall-off correlation with the BP fall-off. This agrees with previous work.[25,57,70]

The PG spatial distributions in both detection geometries of sphere and cylinder show isotropically azimuthal emission and non-isotropically axial emission. The PG emission is also seen to be slightly backward relative to the BP position, while neutrons are forward peaked. These results are in good agreement with published data.[57,71] The detection sphere setup showed a gamma angular preference of $\varphi \sim 110^{o}$ from both water and PMMA cylindrical phantoms, while neutrons are mainly directed forward at $\varphi \sim 60^{o}$ from water and $\varphi \sim 70^{o}$ from PMMA, with respect to the coordinate system centre. We determined from these results that gamma emission is $\sim 20^{o}$ backward peaked in water, and $\sim 17^{o}$ backward peaked in PMMA, relative to the BP. From the detection cylinder setup, the backward angle of gamma emission was determined to be $\sim 11^{o}$ in water, and $\sim 8^{o}$ in PMMA, relative to the BP. A $\sim 3^{o}$ difference between water and PMMA is seen to exist from both detection geometry setups. These results indicate that there exists an optimal axial angular preference for PG detection.

The timing properties of PG detection show a narrow TOF window at around 3 ns in both water and PMMA, while neutrons are not predominantly emitted until around 4 ns. These results show agreement with previous studies.[54,55,72] This timing difference can be utilised to differentiate the PG signal from the interference of neutrons. This indicates that a TOF technique can be utilised to improve the signal-to-noise ratio of PG detection. In addition, the preliminary modelling of a BGO based scintillation detector shows that this detector (with

parameters as defined in this study) is suitable for detecting the optimal 4.44 MeV PG peak, compared to the 5.21 and 6.13 MeV PG rays.

All the above results indicate that there is the probability to optimize the strategy for PG signal detection. Utilising these optimal energy window, angular window and TOF window, PG image formation can be significantly improved for BP tracking. Hence, in this work we have not only aimed to maximise the PG signal, but we have also investigated techniques to minimise the background signal, combining both space and time methods to improving PG imaging for beam range verification. Monitoring PG and neutron emission in both space and time has the potential to improve the PG signal-to-noise ratio and the accuracy of beam range verification during hadron therapy, as well as eliminating the need for bulky shielding around the detectors. Given that this is not a new concept, such that some published work have explored both these platforms of improving PG imaging[54,55], the practicality of this technique looks promising. The results from this study will help design and optimize a PG imaging system to maximise PG image formation and detection. Further investigations for a novel PG imaging detector and system are under study.

References

[1] CERN, ENLIGHT, What is Hadron Therapy?, Available: http://enlight.web.cern.ch/what-is-hadron-therapy [Accessed 28/5/2014]

[2] Wilson RR 1946, Radiological use of fast protons, Radiology 47(5): p. 487-491

[3] Levy RP, Fabrikant JI, Frankel KA, Phillips MH, Lyman JT, Lawrence JH, Tobias CA 1991, Heavy-charged-particle radiosurgery of the pituitary gland: clinical results of 840 patients, Stereotact. Funct. Neurosurg. 57(1-2): p. 22-35

[4] Castro JR 1993, Heavy Ion Therapy: Bevalac Epoch, Lawrence Berkeley Laboratory University of California

[5] Slater JM, Archambeau JO, Miller DW, Notarus MI, Preston W, Slater JD 1992, The proton treatment center at Loma Linda University Medical Center: rationale for and description of its development, Int. J. Radiat. Oncol. Biol. Phys. 22(2): p. 383-389

[6] Proton Therapy Center, Proton Therapy Around the World, Available: http://www.proton-cancer-treatment.com/proton-therapy/proton-therapy-around-the-world/ [Accessed 17/8/15]

[7] The National Association for Proton Therapy, Proton News, Available: http://www.proton-therapy.org/patients55.html [Accessed 17/8/15]

[8] Smith AR 2009, Vision 20/20: Proton Therapy, Am. Assoc. Phys. Med. 36(2): p. 556-568

[9] Polf JC, Panthi R, Mackin DS 2013, Measurement of characteristic prompt gamma rays emitted from oxygen and carbon in tissue-equivalent samples during proton beam irradiation, Phys. Med. Biol. 58(17): p. 5821-5831

[10] Bom V, Joulaeizadeh L, Beekman F 2012, Real-time prompt gamma monitoring in spot-scanning proton therapy using imaging through a knife-edge-shaped slit, Phys. Med. Biol. 57(2): p. 297-308

[11] Knopf AC, Lomax A 2013, In vivo proton range verification: a review, Phys. Med. Biol. 58(15): p. 131-160

[12] Essers M, Mijnheer BJ 1999, In vivo dosimetry during external photon beam radiotherapy, Int. J. Radiat. Oncol. Biol. Phys. 43(2): p. 245-259

[13] Scarantino CW, Ruslander DM, Rini CJ, Mann GG, Nagle HT, Black RD 2004, An implantable radiation dosimeter for use in external beam radiation therapy, Med. Phys. 31(9): p. 2658-2671

[14] Scarantino CW, Rini CJ, Aquino M, Carrea TB, Ornitz RD, Anscher MS, Black RD 2005, Initial clinical results of an in vivo dosimeter during external beam radiation therapy, Int. J. Radiat. Oncol. Biol. Phys. 62(2): p. 606-613

[15] Black RD, Scarantino CW, Mann GG, Anscher MS, Ornitz RD, Nelms BE 2005, An analysis of an implantable dosimeter system for external beam therapy, Int. J. Radiat. Oncol. Biol. Phys. 63(1): p. 290-300

[16] Beyer GP, Scarantino CW, Prestidge BR, Sadeghi AG, Anscher MS, Miften M, Carrea TB, Sims M, Black RD 2007, Technical evaluation of radiation dose delivered in prostate cancer patients as measured by an implantable MOSFET dosimeter, Int. J. Radiat. Oncol. Biol. Phys. 69(3): p. 925-935

[17] Beyer GP, Kry SF, Espenhahn E, Rini C, Boyles E, Mann G 2011, Evaluation of an implantable MOSFET dosimeter designed for use with hypofractionated external beam treatments and its applications for breast and prostate treatments, Med. Phys. 38(8): p. 4881-4887

[18] Rosenfeld AB, Bradley P, Cornelius I, Kaplan GI, Allen BJ 2000, A new silicon detector for microdosimetry applications in proton therapy, Nuclear Science IEEE 47(4): p. 1386-1394

[19] Lu HM 2008, A potential method for in vivo range verification in proton therapy treatment, Phys. Med. Biol. 53(5): p. 1413-1424

[20] Mumot M, Algranati C, Hartmann M, Schippers JM, Hug E, Lomax AJ 2010, Proton range verification using a range probe: definition of concept and initial analysis, Phys. Med. Biol. 55(16): p. 4771-4782

[21] Schneider U, Pedroni E 1995, Proton radiography as a tool for quality control in proton therapy, Med. Phys. 22(4): p. 353-363

[22] Doolan PJ, Testa M, Sharp G, Bentefour EH, Royle G, Lu HM 2015, Patient-specific stopping power calibration for proton therapy planning based on single-detector proton radiography, Phys. Med. Biol. 60(5): p. 1901-1917

[23] Schulte RW, Bashkirov V, Klock MC, Li T, Wroe AJ, Evseev I, Williams DC, Satogata T 2005, Density resolution of proton computed tomography, Med. Phys. 32(4): p. 1035-1046

[24] Schulte R, Bashkirov V, Tianfang L, Zhengrong L, Mueller K, Heimann J, Johnson LR, Keeney B, Sadrozinski HF-W, Seiden A, Williams DC, Lan Z, Zhang L, Peggs S, Satogata T, Woody C 2004, Conceptual design of a proton computed tomography system for applications in proton radiation therapy, Nuclear Science IEEE 51(3): p. 866-872

[25] Min CH, Kim CH, Youn MY, Kim JW 2006, Prompt gamma measurements for locating the dose falloff region in the proton therapy, Appl. Phys. Lett. 89(18): p. 183517

[26] Moteabbed M, Espana S, Paganetti H 2011, Monte Carlo patient study on the comparison of prompt gamma and PET imaging for range verification in proton therapy, Phys. Med. Biol. 56(4): p. 1063-1082

[27] Polf JC, Peterson S, McCleskey M, Roeder BT, Spiridon A, Beddar S, Trache L 2009, Measurement and calculation of characteristic prompt gamma ray spectra emitted during proton irradiation, Phys. Med. Biol. 54(22): p. N519-527

[28] Zhu X, Fakhri GEI 2013, Proton therapy verification with PET imaging, Theranostics 3(10): p. 731-740

[29] Parodi K, Ponisch F, Enghardt W 2005, Experimental study on the feasibility of in-beam PET for accurate monitoring of proton therapy, IEEE Trans. Nucl. Sci. 52(3): p. 778-786

[30] Oelfke U, Lam GK, Atkins MS 1996, Proton dose monitoring with PET: quantitative studies in Lucite, Phys. Med. Biol. 41(1): p. 177-196

[31] Parodi K, Bortfeld T 2006, A filtering approach based on Gaussian-power law convolutions for local PET verification of proton radiotherapy, Phys. Med. Biol. 51(8): p. 1991-2009

[32] Gensheimer MF, Yock TI, Liebsch NJ, Sharp GC, Paganetti H, Madan N, Grant PE, Bortfeld T 2010, In vivo proton beam range verification using spine MRI changes, Int. J. Radiation Oncology Biol. Phys. 78(1): p. 268-275

[33] Yuan Y, Andronesi OC, Bortfeld TR, Richter C, Wolf R, Guimaraes AR, Hong TS, Seco J 2013, Feasibility study of in vivo MRI based dosimetric verification of proton end-of-range for liver cancer patients, Radiother. Oncol. 106(3): p. 378-382

[34] Polf JC, Peterson S, Ciangaru G, Gillin M, Beddar S 2009, Prompt gamma-ray emission from biological tissues during proton irradiation: a preliminary study, Phys. Med. Biol. 54(3): p. 731-743

[35] Kurosawa S, Kubo H, Ueno K, Kabuki S, Iwaki S, Takahashi M, Taniue K, Higashi N, Miuchi K, Tanimori T, Kim D, Kim J 2012, Prompt gamma detection for range verification in proton therapy, Curr. Appl. Phys. 12(2): p. 364-368

[36] Lee KS, Hong B, Park S, Rhee HB, Sim KS 2011, Monte-Carlo simulations for proton-beam-induced prompt radiations in biological tissue, J. Korean Phys. Soc. 58(1): p. 15-21

[37] Mackin D, Peterson S, Beddar S, Polf J 2012, Evaluation of a stochastic reconstruction algorithm for use in Compton camera imaging and beam range verification from secondary gamma emission during proton therapy, Phys. Med. Biol. 57(11): p. 3537-3553

[38] Newhauser WD, Zhang R 2015, The physics of proton therapy, Phys. Med. Biol. 60(8): p. R155-R209

[39] Attix FH 2004, Introduction to Radiological Physics and Radiation Dosimetry, WILEY-VCH Verlag GmbH & KGaA, Weinheim

[40] Knoll GF 2000, Radiation Detection and Measurement, 3rd Ed., John Wiley & Sons, Inc.

[41] Kraan AC 2015, Range verification methods in particle therapy: underlying physics and Monte Carlo modeling, Front Oncol. 5: 150 doi:10.3389/fonc.2015.00150.

[42] Ziegler JF 1999, The stopping of energetic light ions in elemental matter, J. Appl. Phys. 85(3): p. 1249-1272

[43] Leo WR 1994, Techniques for Nuclear and Particle Physics Experiments, Second ed New York NY, Springer Verlag

[44] Olive KA, Particle Data Group 2014, Review of Particle Physics, Chin. Phys. C38(9): 090001

[45] Lindhard J, Nielsen V, Scharff M, Thomsen PV 1963, Integral equations governing radiation effects, Mat. Fys. Medd. Dan. Vid. Selsk. 33(10)

[46] Ziegler JF, Biersack JP, Littmark U, Anderson HH 1977, The Stopping and Ranges of Ions in Matter, New York Pergamon Press

[47] Ma CMC, Lomax T, Hendee WR 2013, Proton and Carbon Ion Therapy, Taylor & Francis Group, LLC

[48] Seco J, Verhaegen F, Hendee WR 2013, Monte Carlo Techniques in Radiation Therapy, Taylor & Francis Group, LLC

[49] Kozlovsky B, Murphy RJ, Ramaty R 2002, Nuclear deexcitation gamma-ray lines from accelerated particle interactions, ApJS 141(2): p. 523-541

[50] Peterson SW, Robertson D, Polf J 2010, Optimizing a three-stage Compton camera for measuring prompt gamma rays emitted during proton radiotherapy, Phys. Med. Biol. 55(22): p. 6841-6856

[51] Frandes M, Zoglauer A, Maxim V, Prost R 2010, A tracking Compton-scattering imaging system for hadron therapy monitoring, IEEE Trans. Nucl. Sci. 57(1): p. 144-150

[52] Verburg JM, Shih HA, Seco J 2012, Simulation of prompt gamma-ray emission proton radiotherapy, Phys. Med. Biol. 57(17): p. 5459-5472

[53] Testa M, Bajard M, Chevallier M, Dauvergne D, Freud N, Henriquet P, Karkar S, Foulher FL, Letang JM, Plescak R, Ray C, Richard MH, Schardt D, Testa E 2010, Real-time monitoring of the Bragg-peak position in ion therapy by means of single photon detection, Radiat. Environ. Biophys. 49(3): p. 337-343

[54] Biegun AK, Seravalli E, Lopes PC, Rinaldi I, Pinto M, Oxley DC, Dendooven P, Verhaegen F, Parodi K, Crespo P, Schaart DR 2012, Time-of-flight neutron rejection to improve prompt gamma imaging for proton range verification: a simulation study, Phys. Med. Biol. 57(20): p. 6429-6444

[55] Golnik C, Hueso-Gonzalez F, Muller A, Dendooven P, Enghardt W, Fiedler F, Kormoll T, Roemer K, Petzoldt J, Wagner A, Pausch G 2014, Range assessment in particle therapy based on prompt gamma-ray timing measurements, Phys. Med. Biol. 59(18): p. 5399-5422

[56] Kim JW, Yim H, Kim D 2009, Pinhole camera measurements of prompt gamma-ray for detection of beam range variation in proton therapy, J. Korean Phys. Soc. 55(4): p. 1673-1676

[57] Smeets J, Roellinghoff F, Prieels D, Stichelbaut F, Benilov A, Busca P, Fiorini C, Peloso R, Basilavecchia M, Frizzi T, Dehaes JC, Dubus A 2012, Prompt gamma imaging with a slit camera for real-time range control in proton therapy, Phys. Med. Biol. 57(11): p. 3371-3405

[58] Kormoll T, Fiedler F, Schone S, Wustemann J, Zuber K, Enghardt W 2011, A Compton imager for in-vivo dosimetry of proton beams – A design study, Nucl. Instrum. Methods Phys. Res. 626-627: p. 114-119

[59] Richard MH, Chevallier M, Dauvergne D, Freud N, Henriquet P, Le Foulher F, Letang JM, Montarou G, Ray C, Roellinghoff F, Testa E, Testa M, Walenta AH 2011, Design guidelines for a double scattering Compton camera for prompt-γ imaging during ion beam therapy: a Monte Carlo simulation study, IEEE Trans. Nucl. Sci. 58(1): p. 87-94

[60] Min CH, Lee HR, Kim CH, Lee SB 2012, Development of array-type prompt gamma measurement system for in vivo range verification in proton therapy, Med. Phys. 39(4): p. 2100-2107

[61] Kang BH, Kim JW 2009, Monte Carlo Design Study of a Gamma Detector System to Locate Distal Falloff in Proton Therapy, IEEE Transactions on Nuclear Science. 56(1): p. 46-50

[62] CERN, Geant4, last updated 28 April 2015, Available: http://geant4.cern.ch/ [Accessed 13/5/15]

[63] CERN, About Geant4, last updated 8 July 2006, Available: http://geant4.web.cern.ch/geant4/support/about.shtml [Accessed 10/9/15]

[64] National Institute of Standards and Technology, U.S. Department of Commerce.

[65] CERN, Model: Binary Cascade, Available: http://geant4.cern.ch/support/proc_mod_catalog/models/hadronic/BinaryCascade.html [Accessed 28/8/15]

[66] Hall DC, Makarova A, Paganetti H, Gottschalk B 2015, Validation of nuclear models in Geant4 using the dose distribution of a 177 MeV proton pencil beam, Phys. Med. Biol. 61(1): p. N1-N10

[67] Kinheng International Holding Co., Ltd. 2012, BGO scintillation crystal,Scintillator BGO,Bi4Ge3O12(BGO)Bismuth Germanate scintillator, Available: http://www.kinheng-crystal.com/products-detail.asp?id=1340 [Accessed 25/4/15]

[68] Schardt D, Elsasser T, Schulz-Ertner D 2010, Heavy-ion tumor therapy: Physical and radiobiological benefits, Rev. Mod. Phys. 82(1): p. 383-425

[69] Fiedler F, Kormoll T, Muller A, Enghardt W 2010, Requirements on the instrumentation of a prompt gamma measuring device, NSS/MIC IEEE: p. 1047-1049

[70] Verburg JM, Riley K, Bortfeld T, Seco J 2013, Energy- and time-resolved detection of prompt gamma-rays for proton range verification, Phys. Med. Biol. 58(20): L37-49

[71] Lee E, Polf JC, Mackin DS, Beddar S, Dolney D, Ainsley C, Kassaee A, Avery S 2014, Study of the angular dependence of a prompt gamma detector response during proton radiation therapy, Int. J. Particle Ther. 1(3): p. 731-744

[72] Lopes PC, Clementel E, Crespo P, Henrotin S, Huizenga J, Janssens G, Parodi K, Prieels D, Roellinghoff F, Smeets J, Stichelbaut F, Schaart DR 2015, Time-resolved imaging of prompt-gamma rays for proton range verification using a knife-edge slit camera based on digital photon counters, Phys. Med. Biol. 60(15): p. 6063-6085

[73] Lemieux DA, Baudet C, Grim GP, Barber HB, Miller BW, Fasje D, Furenlid 2011, Investigation of the possibility of gamma-ray diagnostic imaging of target compression at NIF, Proc SPIE Int Soc Opt Eng. 8144: 814407 doi:10.1117/12.895765.